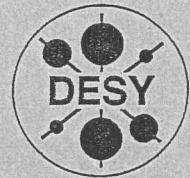


DEUTSCHES ELEKTRONEN-SYNCHROTRON



DESY-THESIS-1999-045

December 1999

Vector Meson Photoproduction at
Large Momentum Transfer at HERA

by

L. Adamczyk

Eigentum der **DESY** Bibliothek
Property of **DESY** library
Zugang: 17. Mai 2000
Accessions:
Keine Ausleihe
Not for loan

ISSN 1435-8085

NOTKESTRASSE 85 - 22607 HAMBURG

DESY behält sich alle Rechte für den Fall der Schutzrechtserteilung und für die wirtschaftliche Verwertung der in diesem Bericht enthaltenen Informationen vor.

DESY reserves all rights for commercial use of information included in this report, especially in case of filing application for or grant of patents.

To be sure that your reports and preprints are promptly included in the
HEP literature database
send them to (if possible by air mail):

DESY
Zentralbibliothek
Notkestraße 85
22603 Hamburg
Germany

DESY
Bibliothek
Platanenallee 6
15738 Zeuthen
Germany

Vector Meson Photoproduction at Large Momentum Transfer at HERA

PhD Thesis

Leszek Adamczyk

*University of Mining and Metallurgy, Faculty of Physics and Nuclear Techniques,
al. Mickiewicza 30, PL-30059 Cracow, Poland*

May 24 1999

Supervisor: Prof. dr hab. Danuta Kisielewska

Vector Meson Photoproduction at Large Momentum Transfer at HERA

Abstract

This thesis reports on a study of elastic and proton-dissociative production of ρ^0 , ϕ , and J/ψ vector mesons ($ep \rightarrow eVp$, $ep \rightarrow eVN$) at the positron-proton collider HERA. The data used for this analysis were collected by the ZEUS experiment during 1995 and correspond to an integrated luminosity of 1.98 pb^{-1} . The data cover the kinematic range $85 < W < 105 \text{ GeV}$ and $Q^2 < 0.01 \text{ GeV}^2$ where W and $-Q^2$ are the virtual photon-proton center of mass energy and the squared four-momentum transferred by the photon. The low values of Q^2 covered made it possible to precisely reconstruct the four-momentum transfer squared at the photon-vector meson vertex (t) and to extract from the data the cross sections for real photoproduction of vector mesons ($\gamma p \rightarrow Vp$, $\gamma p \rightarrow VN$) up to $-t = 3 \text{ GeV}^2$. In the case of ρ^0 ($\rho^0 \rightarrow \pi^+\pi^-$) production, the $\pi^+\pi^-$ invariant mass distribution has been investigated as a function of t . The spectra show deviations from a simple relativistic Breit-Wigner shape as expected in models in which the asymmetry of the $\pi^+\pi^-$ invariant mass shape is ascribed to the interference of resonant and non-resonant $\pi^+\pi^-$ production. The asymmetry of the ρ^0 mass shape decreases with increasing $-t$. The spin density matrix elements obtained from the decay angular distribution of ρ^0 , ϕ and J/ψ mesons are generally consistent with expectations based on s -channel helicity conservation, except for the highest $-t$ range accessible in this analysis where r_{1-1}^{04} was found to be different from zero for all mesons. However present accuracy does not allow to conclude about SCHC violation. The differential cross sections $d\sigma/dt$ for elastic and proton-dissociative ρ^0 , ϕ and J/ψ production have been measured and compared to predictions of QCD models. The proton-dissociative cross sections at $-t > 1 \text{ GeV}^2$ could be successfully described by QCD models. However for ρ^0 and ϕ meson photoproduction the non-perturbative mechanisms still dominate in the considered kinematical range. The ratio of elastic to proton-dissociative cross sections decreases with increasing $-t$ for all three vector mesons in a similar way thus confirming the Regge factorization hypothesis. The ratios of ϕ to ρ^0 and J/ψ to ρ^0 photoproduction cross sections were studied as a function of t for both elastic and proton-dissociative processes. The ratios are lower than the expected ones assuming flavour independent interactions. The Pomeron trajectory has been determined from the study of the W dependence of $d\sigma/dt$ at fixed t for ρ^0 and ϕ mesons in the range $0.0 < -t < 0.9 \text{ GeV}^2$ and $0.0 < -t < 1.4 \text{ GeV}^2$ respectively. From elastic ρ^0 photoproduction the result is $\alpha_P(t) = (1.08 \pm 0.02) + (0.11 \pm 0.04)t$ and from that of ϕ data $\alpha_P(t) = (1.08 \pm 0.01) + (0.15 \pm 0.04)t$.

Contents

1	Introduction	5	5	Monte Carlo simulation	35	
2	Diffractive vector meson production in positron-proton collision	7		5.1	Monte Carlo generators 35	
2.1	Positron-proton scattering	7		5.2	Comparison of MC with data 38	
2.1.1	Relationship between positron-proton and photon-proton cross sections.	8		5.2.1	Rewighting of the ρ^0 MC 39	
2.1.2	The hadronic character of the photon	9		5.2.2	Rewighting of the ϕ MC 42	
2.2	Diffractive scattering	9		5.2.3	Rewighting of the J/ψ MC 45	
2.2.1	Diffraction and triple Regge formalism	10		5.3	Resolution and acceptance 47	
2.2.2	Diffraction in photoproduction	11		5.3.1	Resolution 47	
2.3	Vector meson production	12		5.3.2	Acceptance 48	
2.3.1	Regge theory expectations	14		6	Results	50
2.3.2	Photoproduction in the presence of a hard scale	15		6.1	Estimate of systematic uncertainties	50
3	The ZEUS detector at HERA	17		6.2	Separation of elastic and proton-dissociative processes.	52
3.1	The HERA collider	17		6.3	ρ^0 photoproduction	55
3.2	The ZEUS detector	18		6.3.1	Mass distribution	55
4	Reconstruction and event selection	24		6.3.2	Differential cross section $d\sigma/dt$	59
4.1	Offline event reconstruction	24		6.3.3	Decay angular distribution	62
4.1.1	Reconstruction of particles in detectors	25		6.4	ϕ photoproduction	65
4.1.2	Reconstruction of kinematic variables	26		6.4.1	Mass distribution	65
4.2	Trigger	27		6.4.2	Differential cross section $d\sigma/dt$	67
4.2.1	Trigger for vector meson events	27		6.4.3	Decay angular distribution	68
4.2.2	Trigger efficiency	28		6.5	J/ψ photoproduction	70
4.3	Selection of vector meson candidates	31		6.5.1	Mass distribution	70
				6.5.2	Differential cross section $d\sigma/dt$	72
				6.5.3	Decay angular distribution	73
				7	Discussion	75
				7.1	Comparison with the previous ZEUS measurements	75
				7.2	Comparison with pQCD based models and Regge based models	79
				7.2.1	Comparison with pQCD based models	79
				7.2.2	Ratios of cross sections for vector meson photoproduction	80
				7.2.3	Comparison with Regge pole based models	82
				8	Conclusions	88

List of Abbreviations

BCAL	barrel calorimeter
BPC	beam pipe calorimeter
BW	Breit-Wigner function
CTD	central tracking detector
DESY	Deutsches Elektronen-Synchrotron
DIS	deep inelastic scattering
EMC	electromagnetic calorimeter
FCAL	forward calorimeter
FLT	first level trigger
HAC	hadronic calorimeter
HERA	Hadron-Elektron Ring Anlage
IP	interaction point
LPS	leading proton spectrometer
LLA	leading logarithmic approximation
LUMI	luminosity monitor
MC	Monte Carlo
PMT	photomultiplier tube
pQCD	perturbative QCD
PRT	proton remnant tagger
PT	photoproduction tagger
QCD	quantum chromodynamics
RCAL	rear calorimeter
SCHC	s-channel helicity conservation
SLT	second level trigger
TLT	third level trigger
UCAL	uranium calorimeter
VDM	vector meson dominance model
VW	veto wall

List of Symbols

α	fine-structure constant
$\alpha_P(t)$	Pomeron trajectory
$\alpha_P(0)$	intercept of the Pomeron trajectory
α'_P	slope of the Pomeron trajectory
b_{el}	t-slope of the elastic process
b_{pd}	t-slope of the proton-dissociative process
D	dispersion of the particle multiplicity of the system N
e	incoming positron
e'	scattered positron
E_e	energy of the incoming positron
$E_{e'}$	energy of the scattered positron
E_{max}	maximum allowed energy of a calorimeter cell not associated with the tracks
η	pseudorapidity
E_V	energy of outgoing vector meson
Φ	angle between V production plane and positron scattering plane
Φ_γ	integrated photon flux

ϕ_h	azimuthal decay angle in the helicity frame
γ	photon
γ^*	virtual photon
$\Gamma(y, Q^2)$	photon flux
k	four-momentum of the initial positron
k'	four-momentum of the scattered positron
M_e	positron mass
M_N	mass of the proton-dissociative state
M_P	proton mass
M_V	vector meson mass
M_{ee}	invariant mass of the two tracks assuming that they are electrons
M_{KK}	invariant mass of the two tracks assuming that they are kaons
$M_{\mu\mu}$	invariant mass of the two tracks assuming that they are muons
$M_{\pi\pi}$	invariant mass of the two tracks assuming that they are pions
N	proton-dissociative state
$\langle n \rangle$	average particle multiplicity of the system N
P	four-momentum of the incoming proton
P'	four-momentum of the outgoing proton or proton-dissociative state
p	proton
p_T	track transverse momentum
$p_{V,T}$	V transverse momentum
$p_{V,Z}$	V longitudinal momentum
IP	Pomeron
Q^2	negative four-momentum square of the virtual photon
q	four-momentum of the virtual photon
\mathbb{R}	Reggeon
R_{max}	maximum distance of the calorimeter cell from the track to be associated
r_{ij}^{kl}	vector meson spin density matrix elements
s	center of mass energy square of the positron proton system
t	four-momentum transfer squared at the proton vertex
θ_h	polar decay angle in the helicity frame
W	center of mass energy of the photon proton system
V	vector meson
V_X, V_Y, V_Z	x,y,z coordinates of the IP (vertex position)
v	vector meson four-vector
X, Y, Z	x,y,z coordinates in the Cartesian system with its origin at nominal positron-proton IP
y	the fraction of the positron energy transferred to the hadronic final state

Chapter 1

Introduction

Vector mesons (V) can be diffractively photo-produced via two processes. In one of them the target proton remains intact and the reaction is called exclusive or elastic,

$$\gamma p \rightarrow Vp, \quad (1.1)$$

and in the other process the proton dissociates into higher mass nucleonic states (N) and the reaction is called proton-dissociative,

$$\gamma p \rightarrow VN. \quad (1.2)$$

Measurements of the exclusive vector meson photoproduction have been very helpful in understanding of high energy interactions. This process has been found to reveal the general characteristics of a diffractive process: a weak energy dependence of the cross section, an exponential fall-off of the forward cross section $d\sigma/dt$ and s-channel helicity conservation (SCHC).

Vector Meson Dominance Model and Regge theory connect vector meson production in photon-hadron collisions to inclusive γp scattering and to hadron-hadron processes. These phenomenological models, often referred to as 'soft models', have been able to describe an extensive list of results obtained in hadron-hadron collisions as well as the results of photon-hadron fixed target experiments at center of mass energies W up to $W \approx 20$ GeV.

The first electron-proton collider HERA with a center-of-mass energy of 300 GeV has allowed the study of electroproduction of vector mesons in a kinematic region previously unexplored and unreachable in fixed target experiments. The HERA lepton beam can be considered as a source of interacting virtual photons. The advent of HERA has therefore allowed the study of photon-proton interactions in a new kinematic regime.

Vector meson production is one of the few processes calculable in perturbative QCD (pQCD). It allows investigation of the gluon content in the proton and the nature of the Pomeron and photon. One of the most important profits from the study of V production is the insight into the transition between the soft and hard regimes of QCD.

The photoproduction of light vector mesons at HERA has been studied in detail and found to exhibit characteristics of soft processes.

The studies of the energy behavior of diffractive vector mesons production at HERA show that whenever a hard scale is present, the cross section rises faster than expected from soft processes. The hard scale can be either the photon virtuality Q^2 , as in the exclusive electroproduction of vector mesons at high Q^2 , $\gamma^* p \rightarrow Vp$ or the mass of the heavy flavour quark, as in the exclusive photoproduction of the J/ψ meson, $\gamma p \rightarrow J/\psi p$.

It was suggested [1, 2] that in processes of diffractive vector meson photoproduction, the four-momentum transfer squared t between the photon and the vector meson may also serve as a hard scale. In this thesis this hypothesis is tested by measuring these diffractive processes as function of t and confronting the data with pQCD based models which should hold in the presence of a hard scale. In addition, the lower $-t$ data is used to compare with models expected to hold for soft processes. This will provide a study of the transition between the soft, non-perturbative, and the hard, perturbative, regimes of QCD.

ZEUS is the multipurpose detector for physics at HERA, taking data since 1992. Its region of coverage in t has been extended in 1995 by the installation of a small angle electromagnetic calorimeter located at $Z = -44$ m in the direction of the outgoing positron. The detection of the scattered positrons in this device ensures that the virtuality of the exchanged photon is $Q^2 \leq 0.01$ GeV², and allows $-t$ to be measured up to high values. In this kinematical regime the virtual photon behaves essentially like a real photon, and photon-proton interactions can be studied indirectly through positron-proton collisions. Therefore in the following this small positron calorimeter is called the Photoproduction Tagger (PT). The PT can bring significant contribution to the understanding of V production at a region of large $-t$ where the calculations of pQCD can be applied.

The ZEUS collaboration consists of almost 500 physicists coming from more than 50 institutes and 12 different nations. Such a large scale experiment requires joint effort from many people. During my time as a PhD student I was a member of the ZEUS Luminosity Monitor (LUMI) group. My contributions in the ZEUS experiment have been the following: participation in the tests of the LUMI detectors at the DESY test beam, development of the calibration techniques used in the LUMI, implementation of the reconstruction software for the LUMI position detectors, monitoring of the data quality and responsibility for the calibration of the LUMI detectors, participation in the offline luminosity calculation, participation in the development and optimization of the trigger for vector meson photoproduction using the PT and analysis of the large $-t$ vector meson production with the PT.

This thesis reports on the study of reactions (1.1) and (1.2) by measuring the processes $ep \rightarrow e'Vp$ and $ep \rightarrow e'VN$, where $V = \rho^0, \phi, J/\psi$ up to $-t = 4$ GeV² using the new ZEUS component, the PT located at $Z = -44$ m.

The organization of this thesis is as follows. Chapter 2 contains a short introduction to the physics of photon-proton scattering at HERA, especially to the vector mesons photoproduction. The components of the ZEUS detector relevant for this analysis are introduced in chapter 3. The reconstruction of the kinematic variables as well as the online and offline event selection are presented in chapter 4. Chapter 5 contains a description of the Monte Carlo simulation programs used in this analysis. Chapter 6 summarizes the results obtained in this thesis. These results are compared with the predictions of the pQCD and Regge based models in chapter 7. Finally conclusions are drawn in chapter 8.

Chapter 2

Diffractive vector meson production in positron-proton collision

In the following a brief description of the essentials of various models for vector meson production in positron-proton collision will be given. First the relevant kinematical variables for positron-proton scattering are introduced. Then the relationship between positron-proton and photon-proton cross sections and the hadronic character of the photon are presented. The overview of the hadron-hadron diffractive scattering will be described next. Finally the basic theoretical expectations for diffractive vector meson production are discussed.

2.1 Positron-proton scattering

The positron-proton interaction proceeds via the exchange of a virtual boson. The intermediate boson can be either a photon γ^* or one of the weak gauge bosons (Z, W). The contribution from weak exchange is negligible at the low values of momentum transfer Q that are involved in the analysis and thus is ignored. One-photon-exchange to the first order is assumed (see Fig. (2.1)).

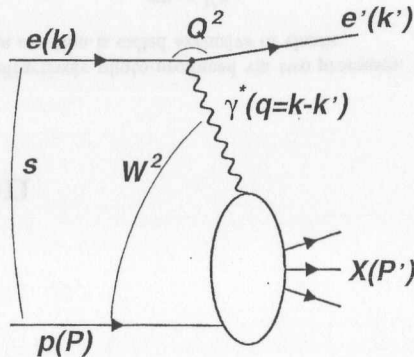


Figure 2.1: Schematic diagram of positron-proton scattering via one-photon-exchange. The positron-proton collision can be seen as a γ^*p collision, with the positron beam emitting the photon. The energy-momentum four-vectors of the particles are given in parentheses.

Assuming that k, k', P, P' are the four-vectors of the initial positron, the final positron, the incoming proton and the outgoing hadronic system, respectively, the kinematics of the inclusive scattering of unpolarized positrons and protons is described by the squared positron-proton center-of-mass energy

$$s = (k + P)^2 \quad (2.1)$$

and any two of the following variables:

- the negative square of the exchanged photon's four-momentum

$$Q^2 = -q^2 = (k - k')^2, \quad (2.2)$$

- the center-of-mass energy of the photon-proton system

$$W^2 = (q + P)^2, \quad (2.3)$$

- the fraction of the positron energy transferred to the hadronic final state in the rest frame of the initial state proton

$$y = \frac{q \cdot P}{k \cdot P}. \quad (2.4)$$

2.1.1 Relationship between positron-proton and photon-proton cross sections.

The differential cross section for the positron-proton interaction at small enough Q^2 ($Q^2 \ll W^2$) can be written as

$$\frac{d^2\sigma^{ep \rightarrow eX}}{dydQ^2} = \Gamma(y, Q^2) (\sigma_T^{\gamma^*p \rightarrow X} + \epsilon\sigma_L^{\gamma^*p \rightarrow X}) \quad (2.5)$$

where Γ is the photon flux

$$\Gamma(y, Q^2) = \frac{\alpha}{2\pi Q^2} \left(\frac{1 + (1-y)^2}{y} - \frac{2(1-y)}{y} \frac{Q_{min}^2}{Q^2} \right) \quad (2.6)$$

and

$$\epsilon = \frac{2(1-y)}{1 + (1-y)^2 - 2(1-y) \frac{Q_{min}^2}{Q^2}}. \quad (2.7)$$

$Q_{min}^2 = M_e^2 \frac{y^2}{1-y}$ is the minimum possible Q^2 , α is fine-structure constant and M_e is electron mass. The functions $\sigma_T^{\gamma^*p \rightarrow X}$ and $\sigma_L^{\gamma^*p \rightarrow X}$ are the photon-proton cross-sections for transversely and longitudinally polarized photons, satisfying

$$\lim_{Q^2 \rightarrow 0} \sigma_T^{\gamma^*p \rightarrow X}(y, Q^2) = \sigma^{\gamma p \rightarrow X}(y),$$

$$\lim_{Q^2 \rightarrow 0} \sigma_L^{\gamma^*p \rightarrow X}(y, Q^2) = 0.$$

Since the virtuality of the exchanged photon is nonzero, one should extrapolate the measured value of $\sigma_T^{\gamma^*p \rightarrow X}$ to $Q^2 = 0$ to obtain $\sigma^{\gamma p \rightarrow X}$. If Q^2 is unmeasured, or poorly determined, such an extrapolation is not possible.

It was shown [3] that if the virtuality of the exchanged photon is small $Q^2 \leq Q_{max}^2 \approx 0.01 \text{ GeV}^2$ one can neglect the Q^2 dependence of the $\sigma_T^{\gamma^*p \rightarrow X}$ and neglect $\sigma_L^{\gamma^*p \rightarrow X}$. In this case, one can write

$$\frac{d^2\sigma^{ep\rightarrow eX}}{dydQ^2} = \Gamma(y, Q^2)\sigma^{\gamma p\rightarrow X}(y) . \quad (2.8)$$

The measured positron-proton cross section $\sigma^{ep\rightarrow eX}$ can thus be transformed into the photon-proton cross section $\sigma^{\gamma p\rightarrow X}$ by dividing the positron-proton cross section by the photon flux integrated over the y and Q^2 range covered by the measurement.

By the same arguments also vector meson production at HERA in the reaction $ep\rightarrow eV X$ can be expressed in terms of the process $\gamma p\rightarrow V X$

$$\frac{d^2\sigma^{ep\rightarrow eV X}}{dydQ^2} = \Gamma(y, Q^2)\sigma^{\gamma p\rightarrow V X}(y) . \quad (2.9)$$

2.1.2 The hadronic character of the photon

It was shown in the previous section that at very low Q^2 there is a direct relation (see Eq. (2.9)) between electroproduction of vector mesons $ep\rightarrow eV X$ and real photoproduction $\gamma p\rightarrow V X$. The latter reaction has been extensively studied in fixed target experiments and is usually interpreted in terms of the hadronic character of the photon. Measurements in the early 50s and 60s of diffractive photoproduction of vector mesons revealed a number of similarities between photon-hadron and hadron-hadron interactions and gave rise to the model of Vector Meson Dominance (VDM). In this model the vector meson photoproduction is viewed as a two step process (see Fig. (2.2)): *i*) photon fluctuates into a vector meson which carries the same quantum numbers as the photon, *ii*) vector meson scatters from the target proton.

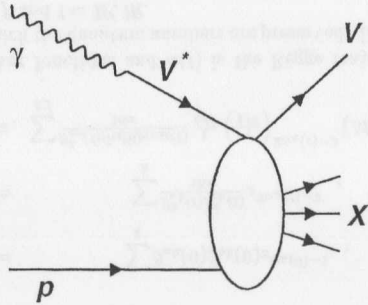


Figure 2.2: Vector meson production in the Vector Dominance Model. The photon fluctuates into a vector meson which then scatters from the proton.

2.2 Diffractive scattering

In hadron-hadron scattering the diffraction covers three types of processes which differ in the characteristics of the final states: *i*) *elastic scattering* when exactly the same incident hadrons come out after the collision, *ii*) *single dissociation* when one of the incident hadrons dissociates into a multi-particle final state preserving quantum numbers of the initial hadron, *iii*) *double dissociation* when each incident

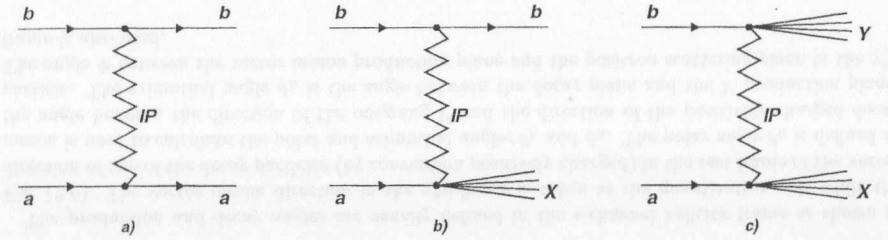


Figure 2.3: a) elastic scattering, b) single dissociation c) double dissociation.

hadron gives rise to a bunch of final particles with exactly the same quantum numbers of the two initial ones.

One usually refers to a diffractive process by saying that it is dominated by the exchange of the Pomeron (IP). From Fig. (2.3), due to the lack of additional final state particles created through color interaction with the exchanged IP, it is clear that IP has to carry vacuum quantum numbers. Experimentally for such events one expects to see no particles in a region in the detector (rapidity gap) between the leading particle b (or system Y) and the system X .

2.2.1 Diffraction and triple Regge formalism

The behavior of the hadron-hadron cross sections can be interpreted in terms of Regge theory [4] in which the interaction is regarded as due to the exchanges of a family of off-shell particles (Regge poles) such that the relevant quantum numbers are conserved. The Regge poles within a single family form a linear trajectory in the J, m^2 plane, where J is the spin of the particle and m its mass. The continuation of a trajectory to negative values of m^2 leads to a parameterization in terms of t as follows:

$$\alpha(t) = \alpha(0) + \alpha' \cdot t \quad (2.10)$$

where $\alpha(0)$ is the intercept and α' is the slope of the trajectory.

Each trajectory has the quantum numbers, isospin, parity, strangeness etc. of the first recurrence from which it takes its name. The mesonic trajectories ($\rho, f_2, a_2, \omega, \dots$) almost coincide and have a common form

$$\alpha(t) \approx 0.5 + t . \quad (2.11)$$

The fermionic trajectories and those interpolating strange particles have a very similar slope α' but lower intercept $\alpha(0)$

$$\alpha(t) \approx 0.0 + t . \quad (2.12)$$

The parameters of the trajectory for the IP exchange have been determined experimentally [5] to be

$$\alpha_P(t) = 1.08 + 0.25 \cdot t \quad (2.13)$$

Generally each Regge pole is called a Reggeon. However to distinguish between pomeron and non-pomeron exchanges in the following the name Reggeon (\mathbb{R}) is reserved for all Regge poles other than the pomeron.

In the Regge limit ($-t \ll M^2 \ll s$) the total, elastic and single dissociation cross section formulas for the interaction of hadrons a and b can be written as:

$$\sigma_{tot}^{ab} = \sum_k \beta_{ak}(0) \beta_{bk}(0) s^{\alpha_k(0)-1}, \quad (2.14)$$

$$\frac{d\sigma_{el}^{ab}}{dt} = \sum_k \frac{\beta_{ak}^2(t) \beta_{bk}^2(t)}{16\pi} s^{2\alpha_k(t)-2}, \quad (2.15)$$

$$\frac{d^2\sigma_{sd}^{ab}}{dt dM^2} = \sum_{k,l} \frac{\beta_{ak}^2(t) \beta_{bl}(0) g_{kkl}(t)}{16\pi} \frac{1}{M^2} \left(\frac{s}{M^2}\right)^{2\alpha_k(t)-2} (M^2)^{\alpha_l(0)-1} \quad (2.16)$$

where $\beta(t)$ and $g(t)$ are vertex functions and $\alpha(t)$ is the Regge trajectory. The sum runs over all the Regge trajectories for which the quantum numbers are preserved. In principle for elastic and single dissociative processes $k = IP, f$ and $l = IP, \mathbb{R}$.

2.2.2 Diffraction in photoproduction

It is useful to explain what one understands by diffractive processes in photoproduction. The true elastic process is the elastic Compton scattering $\gamma p \rightarrow \gamma p$. However this is an electromagnetic process and accounts only for a small part of the total γp cross section while in the hadron-hadron collisions the elastic process takes typically $\sim 20\%$ of the total cross section. In the VDM (described in Sec. (2.1.2)) the photon first fluctuates into the virtual vector meson which then scatters from the proton. With this in mind the process $\gamma p \rightarrow V p$ can be considered as the hadronic elastic scattering in photoproduction. Its contribution to the total γp cross section is of the same magnitude as the elastic scattering in hadron-hadron collisions. With similar arguments the following processes also contribute to the diffractive photoproduction reactions: $\gamma p \rightarrow X p$ (photon dissociation), $\gamma p \rightarrow V N$ (proton dissociation) and $\gamma p \rightarrow X N$ (double dissociation) where $X \neq V$. This is illustrated in Fig. (2.4).

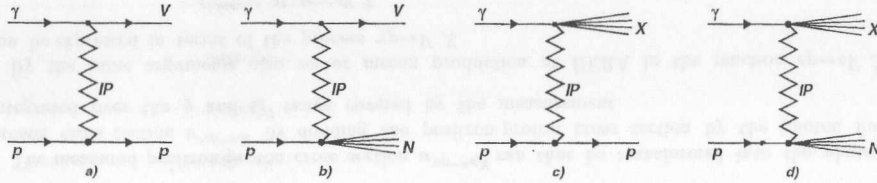


Figure 2.4: a) elastic, b) proton dissociation, c) photon dissociation, d) double dissociation.

2.3 Vector meson production

For the elastic process $\gamma^* p \rightarrow V p$ and the proton-dissociative process $\gamma^* p \rightarrow V N$ ($V \rightarrow$ two charged particles, $q^+ q^-$) the following additional variables are used (see Fig. (2.5))

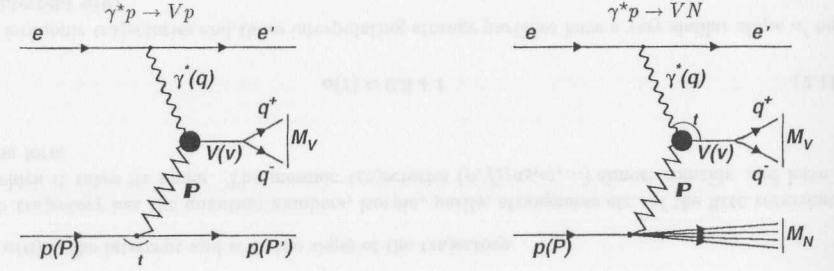


Figure 2.5: Overview of kinematic variables describing vector meson production.

- the squared four-momentum transfer at the photon-V vertex

$$t = (q - v)^2 = (P - P')^2 \quad (2.17)$$

where v is the vector meson four-vector,

- for the proton-dissociative reaction, the mass M_N of the diffractively produced state N is relevant $M_N^2 = (P')^2$,
- the mass of the vector meson M_V ,
- the angles describing the production and decay of the vector meson.

Decay angular distribution

The spin state of the produced vector meson can be determined from the angular distribution of its decay products. The knowledge of the vector meson spin allows to study the spin dependent properties of the production process such as s-channel helicity conservation (SCHC, i.e. does the vector meson retain the helicity of the photon?). The relevant formalism has been developed in [6]

The production and decay angles are usually defined in the s-channel helicity frame as shown in Fig. (2.6). The vector meson direction in the $\gamma^* p$ frame is taken as the quantization axis while the direction of one of the decay particles (by convention positively charged) in the rest frame of the vector meson is used to calculate the polar and azimuthal angles θ_h and ϕ_h . The polar angle θ_h is defined as the angle between the direction of the outgoing V and the direction of the positively charged decay particle. The azimuthal angle ϕ_h is the angle between the decay plane and the V production plane. The angle Φ between the vector meson production plane and the positron scattering plane in the $\gamma^* p$ frame is also used.

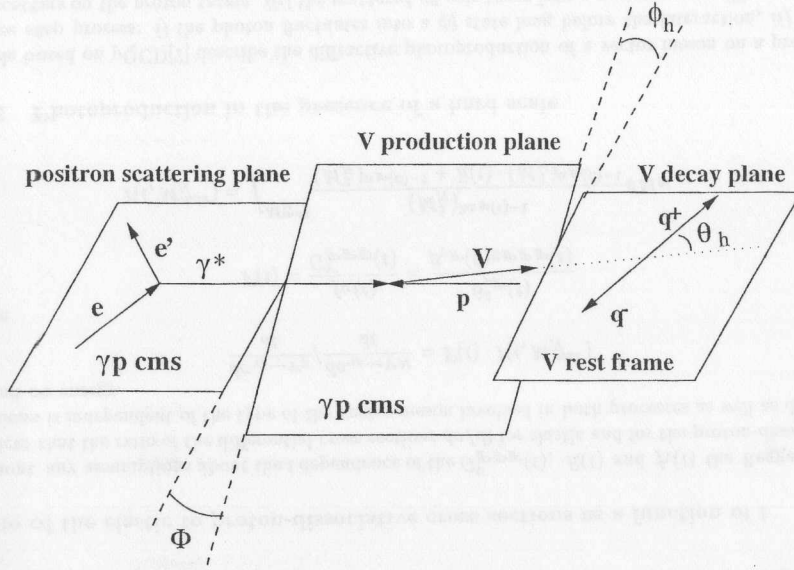


Figure 2.6: Definition of the planes and angles used to describe the decay of the vector meson into two charged particles (q^+ , q^-).

The full decay angular distribution is usually expressed in terms of $(\cos\theta_h, \phi_h, \Phi)$. Since in the analysis presented here the angle Φ is not measured, the decay angular distribution integrated over this angle for an unpolarized positron beam reduces to (for a decay into two spin-0 particles)

$$W(\cos\theta_h, \phi_h) = \frac{3}{4\pi} \left[\frac{1}{2}(1 - r_{00}^{04}) + \frac{1}{2}(3r_{00}^{04} - 1)\cos^2\theta_h - \sqrt{2}Re(r_{10}^{04})\sin 2\theta_h \cos\phi_h - r_{1-1}^{04}\sin^2\theta_h \cos 2\phi_h \right]. \quad (2.18)$$

After integrating over $\cos\theta_h$ or ϕ_h the following one-dimensional distributions are obtained:

$$W(\cos\theta_h) = \frac{3}{4} \left[1 - r_{00}^{04} + (3r_{00}^{04} - 1)\cos^2\theta_h \right], \quad (2.19)$$

$$W(\phi_h) = \frac{1}{2\pi}(1 - r_{1-1}^{04}\cos 2\phi_h) \quad (2.20)$$

where r_{00}^{04} , r_{10}^{04} , and r_{1-1}^{04} are the relevant vector meson spin density matrix elements. The element r_{00}^{04} represents the probability that the vector meson is produced in a helicity zero state. The element r_{10}^{04} is related to the interference between non-flip and helicity single flip amplitudes while r_{1-1}^{04} is related to the interference between helicity non-flip and double flip amplitudes. If SCHC holds then r_{1-1}^{04} and r_{10}^{04} should be zero.

Eq. (2.18) holds for a decay into two spin-0 particles (for example $\rho^0 \rightarrow \pi^+\pi^-$ and $\phi \rightarrow K^+K^-$). For a decay into two spin-1/2 particles (like $J/\psi \rightarrow e^+e^-$ and $J/\psi \rightarrow \mu^+\mu^-$) it has to be replaced by

$$W(\cos\theta_h, \phi_h) = \frac{3}{4\pi} \left[\frac{1}{2}(1 + r_{00}^{04}) - \frac{1}{2}(3r_{00}^{04} - 1)\cos^2\theta_h \right.$$

$$\left. + \sqrt{2}Re(r_{10}^{04})\sin 2\theta_h \cos\phi_h + r_{1-1}^{04}\sin^2\theta_h \cos 2\phi_h \right]. \quad (2.21)$$

After integrating over $\cos\theta_h$ or ϕ_h the following one-dimensional distributions are obtained:

$$W(\cos\theta_h) = \frac{3}{4} \left[1 + r_{00}^{04} - (3r_{00}^{04} - 1)\cos^2\theta_h \right], \quad (2.22)$$

$$W(\phi_h) = \frac{1}{2\pi}(1 + r_{1-1}^{04}\cos 2\phi_h). \quad (2.23)$$

2.3.1 Regge theory expectations

Regge formulas (Eq. (2.15) and Eq. (2.16)) written for the diffractive vector meson photoproduction have the form

$$\frac{d\sigma_{\gamma p \rightarrow Vp}}{dt} = \sum_k \frac{\beta_{V_k}^2(t)\beta_{p_k}^2(t)}{16\pi} (W^2)^{2\alpha_k(t)-2}, \quad (2.24)$$

$$\frac{d^2\sigma_{\gamma p \rightarrow VN}}{dt dM_N^2} = \sum_{k,l} \frac{\beta_{V_k}^2(t)\beta_{N_l}(0)g_{kkll}(t)}{16\pi} \frac{1}{M_N^2} \left(\frac{W^2}{M_N^2} \right)^{2\alpha_k(t)-2} (M_N^2)^{\alpha_l(0)-1}. \quad (2.25)$$

As mentioned in Sec. (2.2.1) for these processes $k = IP, f$ and $l = IP, IR$. In case of ϕ and J/ψ production the f trajectory exchange is forbidden since ϕ and J/ψ are pure $s\bar{s}$ or $c\bar{c}$ states which couple only to the Pomeron. For ρ^0 production the f trajectory exchange is allowed. However its contribution is expected to be negligible at large W^2 , small M_N^2/W^2 and high $-t$. For simplicity in the following the f trajectory exchange is neglected also for ρ^0 production.

For only IP exchange the cross sections are given by

$$\frac{d\sigma_{\gamma p \rightarrow Vp}}{dt} = f_V(t) \cdot (W^2)^{2\alpha_{IP}(t)-2}, \quad (2.26)$$

$$\frac{d^2\sigma_{\gamma p \rightarrow VN}}{dt dM_N^2} = G_{IP^2}^V(t) \frac{1}{M_N^2} \left(\frac{W^2}{M_N^2} \right)^{2\alpha_{IP}(t)-2} \left[(M_N^2)^{\alpha_{IP}(0)-1} + R(t) \cdot (M_N^2)^{\alpha_{IR}(0)-1} \right] \quad (2.27)$$

where

$$f_V(t) = \frac{\beta_{VIP}^2(t)\beta_{pIP}^2(t)}{16\pi}, \quad (2.28)$$

$$G_{IP^2}^V(t) = \frac{\beta_{VIP}^2(t)\beta_{pIP}(0)g_{IP^2}(t)}{16\pi}, \quad (2.29)$$

$$G_{IP^2IR}^V(t) = \frac{\beta_{VIP}^2(t)\beta_{pIR}(0)g_{IP^2IR}(t)}{16\pi}, \quad (2.30)$$

$$R(t) = \frac{G_{IP^2IR}^V(t)}{G_{IP^2}^V(t)} = \frac{\beta_{pIR}(0)g_{IP^2IR}(t)}{\beta_{pIP}(0)g_{IP^2}(t)}. \quad (2.31)$$

It should be noticed that $G_{IP^2}^V(t)$ and $G_{IP^2IR}^V(t)$ depend on the type of produced vector meson while $R(t)$ does not and is expected to be the same for all proton-dissociative reactions ($ap \rightarrow aX$) independent on the type of the initial hadron a .

Elastic cross section

Usually $f_V(t)$ is approximated by the single exponential function $f_V(t) \sim e^{b_{0,el}^V t}$ thus the cross section takes the form

$$\frac{d\sigma_{\gamma p \rightarrow V p}}{dt} \sim e^{(b_{0,el}^V + 2\alpha'_{IP} \ln(W^2)) \cdot t} \cdot (W)^{4\alpha_{IP}(0)-4} \sim e^{b^V(W)t} \cdot (W)^{4\alpha_{IP}(0)-4} \quad (2.32)$$

where $b^V(W) = b_{0,el}^V + 2\alpha'_{IP} \ln(W^2)$. This last expression is an important prediction of the Regge theory. The fact that α'_{IP} is non-zero means that the slope of the t distribution will depend on the energy (this is called shrinkage). Integrating the last expression over t , the energy dependence for an elastic process yields

$$\sigma_{\gamma p \rightarrow V p} \sim \frac{(W)^{4\alpha_{IP}(0)-4}}{b^V(W)} \quad (2.33)$$

Proton-dissociative cross section

Assuming that $G_{PP}^V(t) \sim e^{b_{0,pd}^V t}$ and $R(t) = R = \text{const}$, the proton-dissociative cross section can be written as

$$\frac{d^2\sigma_{\gamma p \rightarrow VN}}{dt dM_N^2} \sim e^{(b_{0,pd}^V + 2\alpha'_{IP} \ln(\frac{W^2}{M_N^2})) \cdot t} \cdot \frac{1}{M_N^2} \left(\frac{W}{M_N} \right)^{4\alpha_{IP}(0)-4} \left[(M_N^2)^{\alpha_{IP}(0)-1} + R \cdot (M_N^2)^{\alpha_{R}(0)-1} \right] \quad (2.34)$$

Similarly as in the elastic process, the fact that α'_{IP} is non-zero means that the slope of the t distribution will depend on the energy and also on the M_N ; $b^V(W, M_N) = b_{0,pd}^V + 2\alpha'_{IP} \ln(\frac{W^2}{M_N^2})$.

Ratio of the elastic to proton-dissociative cross sections as a function of t

Without any assumptions about the t dependence of the $G_{PP}^V(t)$, $R(t)$ and $f_V(t)$ the Regge theory predicts that the ratio of the differential cross sections $d\sigma/dt$ for elastic and for the proton-dissociative reactions is independent of the type of the vector meson involved in both processes as well as does not depend on energy.

$$\frac{d\sigma_{\gamma p \rightarrow V p}}{dt} / \frac{d\sigma_{\gamma p \rightarrow VN}}{dt} = F(t) \cdot I(t, M_N^{max}) \quad (2.35)$$

where

$$F(t) = \frac{f_V(t)}{G_{PP}^V(t)} = \frac{\beta_{pIP}^2(t)}{\beta_{pIP}(0)g_{pIP}(t)} \quad (2.36)$$

and

$$I(t, M_N^{max}) = \int_0^{M_N^{max}} \frac{(M_N^2)^{2\alpha_{IP}(t)-1}}{(M_N^2)^{\alpha_{IP}(0)-1} + R(t) \cdot (M_N^2)^{\alpha_{R}(0)-1}} dM_N \quad (2.37)$$

2.3.2 Photoproduction in the presence of a hard scale

Models based on pQCD[7] describe the diffractive photoproduction of a vector meson on a proton as a three step process: *i*) the photon fluctuates into a $q\bar{q}$ state long before the interaction, *ii*) the $q\bar{q}$ pair scatters on the proton target, *iii*) the scattered $q\bar{q}$ pair turns into a vector meson. The process is depicted in Fig. (2.7).

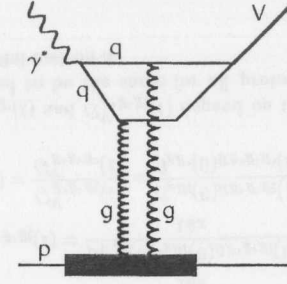


Figure 2.7: The two gluon exchange model describing hard diffractive production of vector mesons.

The photon $q\bar{q}$ fluctuation is described by the photon wave-function derived from QCD [7]. The interaction of the $q\bar{q}$ pair with the proton is mediated in a lowest order by the exchange of two gluons in a colour singlet state. In the leading logarithmic approximation (LLA) it can be also described by the exchange of a gluon ladder [8, 9, 10]. The interaction to be calculable in the pQCD has to involve hard scales. In photoproduction this formalism can be applied if the mass of the vector meson or t is large enough to serve as a hard scale. The transition of a $q\bar{q}$ pair into a meson is a non-perturbative phenomenon and can be described by the meson wave-function derived from the lattice calculations and sum rules [11].

The expected signs of approaching the perturbative regime of the diffractive meson production are:

- A fast rise of the diffractive cross sections with W due to increase of the gluon density in the proton [8].
- No variation with W of the t -dependence of the cross section, i.e. no shrinkage of the diffractive t -slope [9].
- Significant breaking of SCHC for light vector mesons production [10, 12], in particular at the asymptotic limit of very large $-t$ at which the mesons are produced in helicity zero state independent of the initial photon helicity.
- Approximate restoration of the flavour-independent production (i.e. the U(4) symmetry) [13]. From the quark charges of the vector mesons and a flavour-independent production mechanism, the production cross section is expected to have a relative size of 9 : 1 : 2 : 8 for $\rho^0 : \omega : \phi : J/\psi$.

Chapter 3

The ZEUS detector at HERA

In this chapter, first, the HERA accelerator and the ZEUS experiment are overviewed. Then the components of the detector that are of particular relevance for this analysis are briefly described.

3.1 The HERA collider

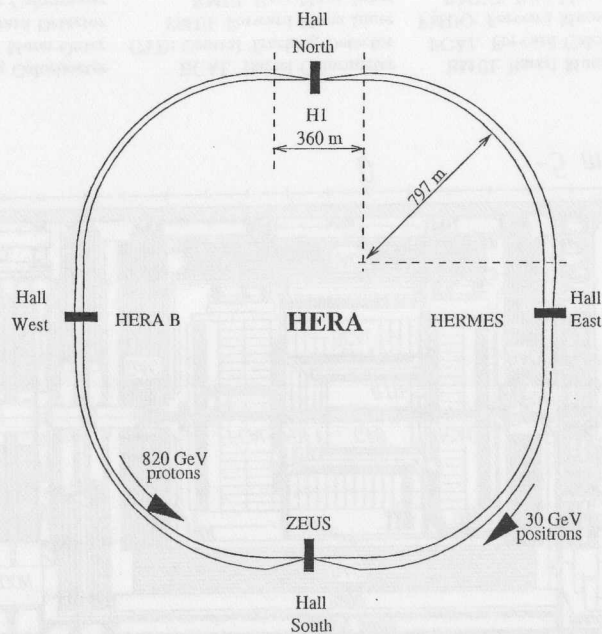


Figure 3.1: The layout of HERA with the location of the different detector halls.

Parameter	designed values	1995
proton energy (GeV)	820	820
positron energy (GeV)	30	27.5
bunches ($ep + e + p$)	210	174+15+16
proton current (mA)	160	55
positron current (mA)	58	30
bunch crossing time (ns)	96	96
specific luminosity ($\text{cm}^{-2}\text{s}^{-1}\text{A}^{-2}$)	$3.9 \cdot 10^{29}$	$5.0 \cdot 10^{29}$
instantaneous luminosity ($\text{cm}^{-2}\text{s}^{-1}$)	$1.7 \cdot 10^{31}$	$4.3 \cdot 10^{30}$
integrated luminosity ($\text{pb}^{-1}/\text{year}$)	35	12.5

Table 3.1: Design and operational(1995) values of the main HERA parameters.

The HERA (Hadron-Elektron Ring Anlage) machine is the world's first lepton-nucleon collider located at the DESY (Deutsches Elektronen Synchrotron) laboratory in Hamburg, Germany. It consists of two storage rings of a circumference of 6.3 km. The proton storage ring uses superconducting magnets to provide the 4.68 T field necessary to store protons of energy 820 GeV. In contrast, the field required to store 27.5 GeV positrons can be reached by conventional magnets. The beams collide at two intersection regions at zero crossing angle to provide ep interactions for the H1 and ZEUS experiments. The center of mass energy from the collision of these two beams is $\sqrt{s} = 300$ GeV, equivalent to a beam of 48 TeV positrons colliding on a fixed target.

The two beams at HERA are also used by two other experiments. In HERMES for the measurement of the proton spin structure the polarized positron beam collides with a polarized proton gas jet. HERA-B aims at measuring CP violation in the B hadron sector by scattering beam protons on a wire target. Fig. (3.1) shows the layout of the HERA collider and the locations of the four experiments.

The positrons and protons are bunched with bunches separated by 96 ns. Some number of bunches are left unpaired (i.e. the corresponding bunch in the other beam is empty) for background studies. In 1995 HERA was filled with 174 paired (*colliding*) bunches and 16 unpaired (*pilot*) proton bunches and 15 unpaired positron bunches.

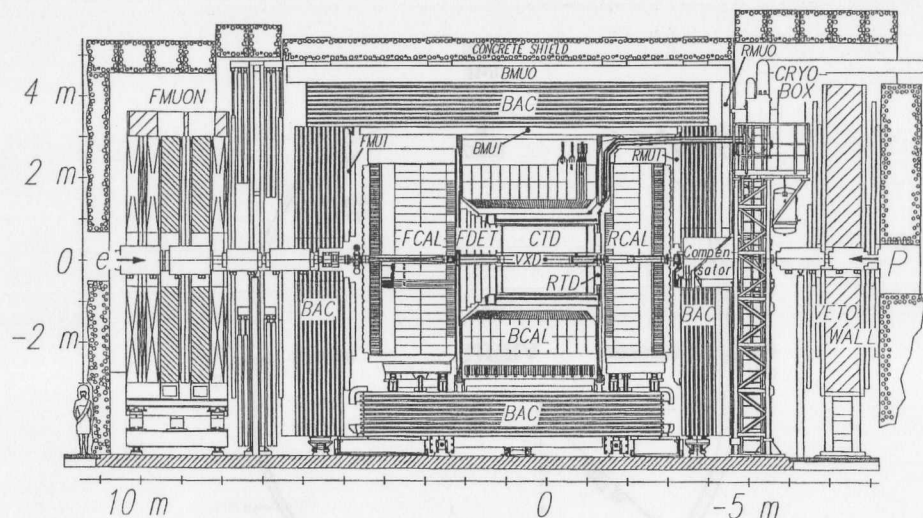
The maximum instantaneous luminosity achieved in 1995 was $4.3 \cdot 10^{30} \text{ cm}^{-2} \text{ s}^{-1}$ to be compared with the design goal of $1.7 \cdot 10^{31} \text{ cm}^{-2} \text{ s}^{-1}$. Tab. (3.1) summarizes the design and operational (1995) performance of HERA.

3.2 The ZEUS detector

The ZEUS detector is a multipurpose magnetic detector with nearly hermetic calorimetric coverage. The detector is described in detail in [14]. It has been supplemented by various sub-detectors dedicated to special physics topics. Here only those components relevant for this analysis are described in some details.

The direction of the proton beam defines the positive z axis, the positive y axis points upwards and the horizontal positive x axis points towards the center of the HERA ring. The highly different beam energies of protons and positrons lead to an asymmetric event topology which has been accounted

Overview of the ZEUS Detector
(longitudinal cut)



BAC: Backing Calorimeter	BCAL: Barrel Calorimeter	BMUI: Barrel Muon Inner
BMUO: Barrel Muon Outer	CTD: Central Tracking Detector	FCAL: Forward Calorimeter
FDET: Forward Detector	FMUI: Forward Muon Inner	FMUO: Forward Muon Outer
RCAL: Rear Calorimeter	RMUI: Rear Muon Inner	RMUO: Rear Muon Outer
RTD: Rear Tracking Detector	VXD: Vertex Detector	

Figure 3.2: Cross sectional view of the ZEUS detector.

for in the design of the detector as can be seen in Fig. (3.2). At the center of the detector inside the magnet coil the inner tracking chambers are located (CTD,RTD,SRTD,FDET). The vertex detector (VXD) was removed before the 1995 running period. Around the tracking devices a high resolution uranium-scintillator calorimeter (UCAL) is built whose parts are called BCAL, FCAL and RCAL. In 1995 ZEUS has been operated with additional components: the Proton Remnant Tagger (PRT) and the Leading Proton Spectrometer (LPS) in the forward direction and the Beam Pipe Calorimeter (BPC), Luminosity Detectors (LUMI) and Photoproduction Tagger (PT) in the backward direction.

The central tracking detector

The CTD is a wire chamber designed to reconstruct charged particles track over a wide range in polar angle ($15^\circ < \theta < 164^\circ$) and full azimuthal coverage. The CTD is composed of 9 super-layers, each consisting of 8 wire layers. Of these, 5 are axial super-layers and 4 are stereo super-layers allowing both $R - \phi$ and Z coordinate measurement. This structure is shown in Fig. (3.3). The sense wires are contained in 576 cells oriented at a 45° angle to the radial direction to produce drift lines approximately tangential to the chamber azimuth in the strong axial magnetic field (1.43 T) provided by the superconducting solenoid.

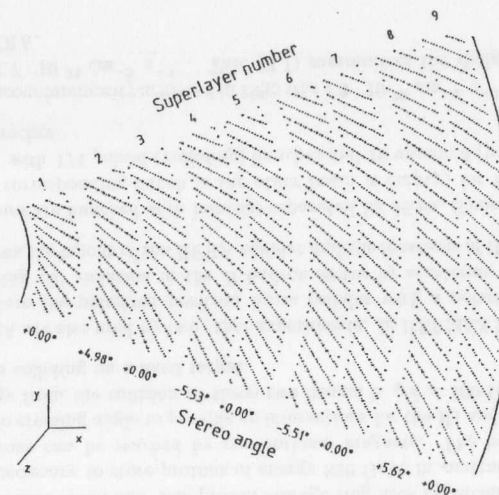


Figure 3.3: Cross section of an octant of the CTD. Sense wires are indicated by larger dots.

The CTD has a design momentum resolution at $\theta = 90^\circ$ in a 1.7 T magnetic field of $\sigma_p/p = \sqrt{(0.002p)^2 + (0.003)^2}$ and a Z coordinate resolution of 1 mm.

The uranium calorimeter

The UCAL is a ^{238}U -scintillator sampling calorimeter, covering the angular range $2.2^\circ < \theta < 178.4^\circ$. The calorimeter consists of a forward component (FCAL) positioned 222 cm from the interaction point (IP) in the proton direction, a barrel part (BCAL) extending from 120 to 230 cm in radius and rear part (RCAL) opposite to FCAL.

The FCAL and RCAL contain 24 modules each. Each module is 20 cm in width. The BCAL is built out of 32 wedge shaped modules. The modules are subdivided transversely into towers, which consists of alternate layers of depleted uranium and plastic scintillator tiles. The towers are subdivided longitudinally into two parts. The inner part constitutes the electromagnetic calorimeter (EMC) with

depth of $\approx 25X_0$. The outer part is called the hadronic calorimeter (HAC). The depth of the hadronic sections are $\approx 6\lambda$, $\approx 4\lambda$ and $\approx 3\lambda$, respectively, for FCAL, BCAL and RCAL. Each section (EMC and HAC) of a tower is made up of a group of cells.

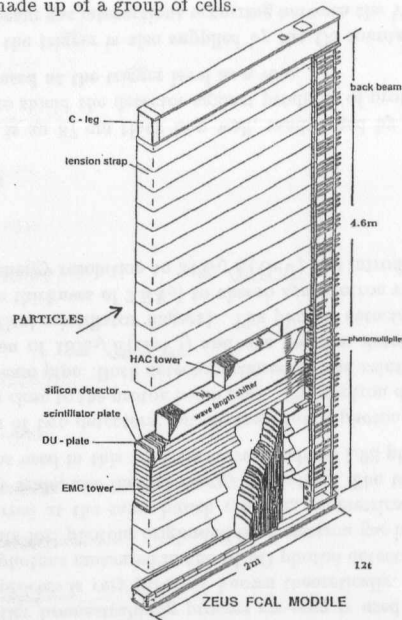


Figure 3.4: Layout of the ZEUS FCAL module. The module is partitioned into towers having two sections, an electromagnetic section EMC and a hadronic section HAC.

The calorimeter design was chosen to give the best possible energy resolution for hadrons. The energy measurement is complicated by the fact that hadrons can initiate nuclear reaction involving neutrons and for various reasons fail to deposit their entire energy. As a consequence a hadron with specific energy will produce a shower whose energy will be less than of the one initiated by an electron of same energy, unless the invisible energy produced in nuclear reactions is compensated for. In the ZEUS calorimeter the compensation is achieved by using depleted uranium in the absorbing material with a precisely matched thickness of the scintillator layers. Uranium calorimeters show better response to hadrons than other types of calorimeters. This is because when using a uranium absorber, some fraction of the hadronic shower energy results in the productions of low energy neutrons. These neutrons can induce fission in ^{238}U . The fission reaction produces fast neutrons which can scatter elastically so that recoil protons can be sampled. This boosts the hadron response considerably. In this way it is possible with the ZEUS UCAL to achieve an identical energy response to electrons and hadrons ($e/h \approx 1$).

The performance of the calorimeter has been measured in detail at the test beam giving the energy resolution of $\sigma_e/E \approx 18\%/\sqrt{E}$ for electrons and $\sigma_h/E \approx 35\%/\sqrt{E}$ for hadrons with the energy E in GeV. Besides its compensating effect the uranium has proven to be an extremely valuable source of calibration and monitoring tool by its natural radioactivity. The inter calibration between cells is known at the 1% level by setting the photomultipliers' gains in such a way as to equalize the uranium signal. Despite the presence of the uranium activity the calorimeter has very low noise (typically 10 MeV for EMC cells and 20 MeV for HAC cells).

The photoproduction tagger

The PT is a small detector located at $Z = -44$ m and sensitive to 22–25 GeV positrons scattered under very small angles. A 3.5 m long part of the HERA positron beam pipe near the PT was modified by making a 14 mm deep and 60 cm long indentation on the side facing the ring center as shown in Fig. (3.5).

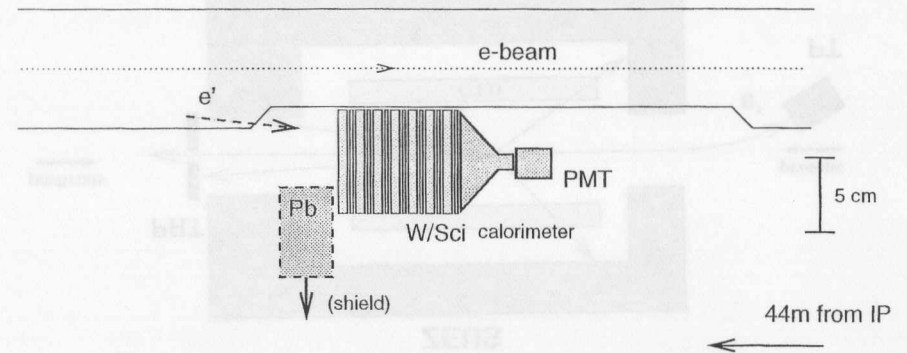


Figure 3.5: Layout of the photon tagging detector.

The detector is an electromagnetic sampling calorimeter made of twelve $70 \times 90 \times 7$ mm³ tungsten plates interleaved with 3 mm thick scintillator layers. The detector sensitive edge is about 28 mm away from the electron beam. After the first, second and third tungsten plates, corresponding approximately to depths of 2, 4 and 6 radiation lengths, additional scintillator strips are installed. These 8 mm wide vertical strips are connected at the top end to plastic light guides. Signals from the strips can be used to apply fiducial cuts and select well contained electromagnetic showers.

Test beam measurements demonstrated that for 1–5 GeV electrons hitting the calorimeter centrally the energy resolution is $0.25/\sqrt{E(\text{GeV})}$ and the calorimeter linearity is better than 1%.

The proton remnant tagger

The PRT [64] consists of 7 pairs of scintillator counters surrounding the beam pipe, in the forward region, which detect particles scattered at very small angles, predominantly associated with the remnant of the proton. Two pairs of counters (PRT1) are located at $Z = 5$ m and five pairs (PRT2) at $Z = 24$ m, tagging particles in the angular range from 6 to 26 mrad and 1.5 to 8 mrad, respectively. In this analysis only PRT1 has been used, because at sufficiently high $-t$ ($-t > 0.5$ GeV²) some fraction of true elastic events, in which the scattered proton stays intact, have the outgoing proton detected in PRT2. Each of the four counter paddles of PRT1 are constructed as scintillator-lead sandwiches with two slices of 26 cm \times 15 cm \times 2.6 mm scintillator separated by 2 mm lead foils as shown in Fig. (3.6).

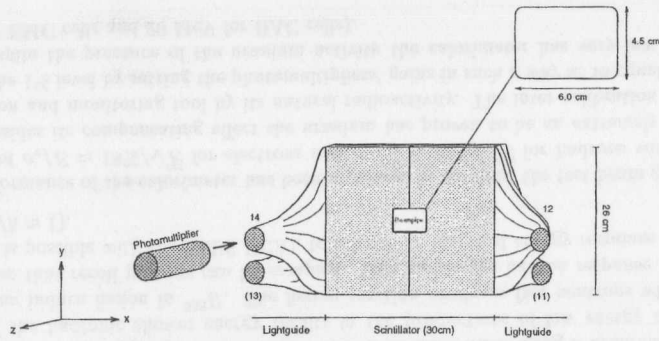


Figure 3.6: Setup of the PRT1 counters. Plot taken from [64].

The luminosity measurement

For a cross section calculation a precise measurement of the luminosity is imperative. The experimental definition of the luminosity is

$$L = R/\sigma \quad (3.1)$$

where R is the events rate for a specific process and σ is the cross section of the same process. At ZEUS the Bethe-Heitler bremsstrahlung process $ep \rightarrow e\gamma$ is used to measure the luminosity as the cross section for this process is very precisely known theoretically. The luminosity is determined from the corrected rate of photons measured in the LUMI photon detector within an energy window where the correction accounts for: photons originated from electron-gas interaction, multiple bremsstrahlung processes which occurred at the same bunch crossing, geometrical acceptance of the detector, non-linearity of the energy scale, and limited energy resolution. The total luminosity gated by the ZEUS experiment in the runs used in this analysis corresponds to 1.98 pb^{-1} with an uncertainty of 1.1%.

The LUMI consists of two detectors: an electron and a photon detector. The photon detector is placed at $Z = -104 \text{ m}$ close to the proton beam pipe. The electron detector is placed about $Z = -35 \text{ m}$ close to the electron beam pipe. Both detectors consist of lead-scintillator electromagnetic calorimeter (with energy resolution of $18\% \sqrt{E(\text{GeV})}$) and one position detector (which consists of two layers of horizontal and vertical scintillator fingers). The photon detector is additionally equipped with a carbon filter (with the thickness of $2.5X_0$) to absorb synchrotron radiation. However the presence of the filter reduces the energy resolution to $24\% \sqrt{E(\text{GeV})}$ and introduces a nonlinearity in the detector response.

The veto counters

The Veto Wall (VW) is an 87 cm thick iron wall, sandwiched by two scintillator layers, located at $Z = 7.27 \text{ m}$. It helps to shield the detector against products of proton-beam gas interactions, and its timing information is used at the trigger level as a veto.

The crucial part in the trigger is also supplied by the C5 counter located at $Z = -5.3 \text{ m}$ which is used to reject proton-beam gas interactions occurring between the VW and this counter.

Chapter 4

Reconstruction and event selection

The reconstruction of the vector meson events is briefly discussed here. Then the online trigger decision and its efficiency is presented. At the end the offline selection criteria are described.

4.1 Offline event reconstruction

The production of vector mesons decaying into the two charged particles are analyzed. This requirement and finite statistics limit the number of analyzed vector mesons to three $\rho^0 \rightarrow \pi^+\pi^-$, $\phi \rightarrow K^+K^-$ and $J/\psi \rightarrow e^+e^-/\mu^+\mu^-$.

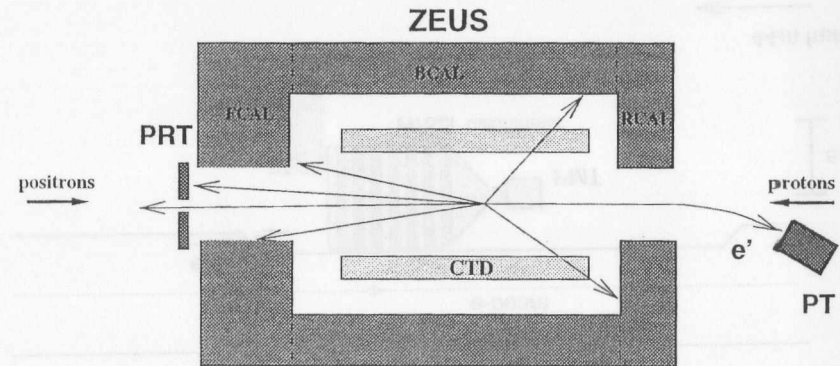


Figure 4.1: Sketch of the diffractive vector meson production signatures in the ZEUS detector.

A sketch of the diffractive vector meson production signatures in the ZEUS detector is shown in Fig. (4.1). It is required to see the two oppositely charged tracks in the CTD. The momenta of the tracks are then used to reconstruct the invariant mass. The event is included in the analysis when the reconstructed mass is near the mass of the vector meson under study. The UCAL and PRT1 are used to reconstruct additional particles. It is required not to observe additional particles in the RCAL and BCAL. This requirement on the one hand reduces the photon-dissociative background and on the

other hand fulfills the experimental definition of diffraction (i.e. presence of the rapidity gap between V and $p(N)$). The proton-dissociative production is tagged by the detection of additional particles in the forward region (FCAL or PRT1) where the final state still consists of an exclusive vector meson and the additional energy is deposited by the proton fragmentation system. The proton-dissociative events where no energy is deposited in the forward direction are experimentally not distinguishable from the elastic ones on an event by event basis. This is the main contribution to the systematic error on the cross sections measurement. The scattered positron detected in the PT ensures low virtuality of the exchanged photon and allows a precise measurement of t .

4.1.1 Reconstruction of particles in detectors

Reconstruction of charged particles in the CTD

The package VCTRACK [15] is used to reconstruct CTD tracks and the primary event vertex. The default reconstruction is dual (performs tracks finding twice per event). The first pass uses only information from the CTD. The second pass uses information from other tracking detectors (VXD, SRTD and RTD). In this analysis only the information from the CTD is used because this reduces uncertainties in corrections for efficiency and acceptance.

Each track candidate begins as a track "seed" in an outer part of the CTD. A track seed is then extrapolated inward, gathering additional hits with increasing precision as the track parameters are updated. After all the track candidates are found the primary vertex is reconstructed. In the vertex reconstruction only tracks which are compatible with coming from the beam line are used and a diffuse pseudo-proton (centered at the beam spot in the XY plane with $\sigma_X = \sigma_Y = 0.7$ cm) is added to help constraining the vertex position. The final vertex fit not only solves for the final vertex position, but also constrains the remaining tracks (vertexed tracks) to it while simultaneously refitting direction and curvature of the tracks.

In this analysis the vertexed tracks (assumed to be the decay tracks of the vector meson) are used to perform a reconstruction of the event's kinematics.

Detection of particles in the UCAL

The reconstruction of the calorimeter quantities uses as input the readout of the two photomultipliers connected to each cell. In this analysis the energies and the positions of the calorimeter cells contain enough information to perform the event selection and reconstruction. Any cell (not associated to the decay tracks observed in the CTD) with energy well above noise is a good evidence of the additional particles being present in an event.

Those cells which exhibit noise above average or had been identified to have a faulty PMT were removed from the analysis. For this purpose the energy distribution of all cells had been monitored for all runs used in this analysis [16].

Detection of particles in the PRT

The particle is observed in the PRT if it hits one of the PRT counter pairs. The hit in a given pair is defined as the coincidence of signals above noise in both counters. In order to suppress signals not related to particles coming from the IP the timing cut was applied.

Detection of scattered positron in the PT

The PT is sensitive to the 22-25 GeV positrons scattered under very small angles. The energy deposit in the PT well above noise (≈ 1 GeV) is required in the trigger. It is possible to reconstruct offline the energy of scattered positrons by applying the fiducial cut which selects electromagnetic showers well contained in the detector. However this reduces the number of observed good vector meson candidates by 30% - 50% and increases systematic uncertainty of the tagging efficiency. In addition the energy of the scattered positrons can be calculated from the vector meson four-momentum with much better resolution. therefore for the purpose of this analysis no offline reconstruction of the scattered positrons was performed.

4.1.2 Reconstruction of kinematic variables

In the present analysis only the three-momenta of the decay particles were measured. The momentum of the scattered positron as well as the angle between the V production plane and the positron scattering plane were not measured. In such tagged photoproduction events Q^2 ranges from the kinematic minimum $Q_{min}^2 \approx M_e^2 y^2 / (1-y) \approx 10^{-9}$ GeV², where M_e is the electron mass, to the maximum value at which the scattered positron is observed in the PT, $Q_{max}^2 \approx 4E_e E_{e'} \sin^2(\theta_{max}/2) \approx 0.01$ GeV², where θ_{max} is the maximum scattering angle and E_e and $E_{e'}$ are the energies of the incoming and the scattered positron, respectively. Since the typical Q^2 is very small (the median Q^2 is approximately 10^{-7} GeV²), it can be neglected in the reconstruction of the other kinematical variables. The photon-proton center-of-mass energy can be approximated by

$$W^2 \approx 2E_p(E_V - p_{V,Z}) \quad (4.1)$$

where E_p and E_V are the energies of the incoming proton and of the produced meson V in the laboratory frame; the meson longitudinal momentum is denoted by $p_{V,Z}$.

The four-momentum transfer squared is given by

$$t = t_0 - 4p_\gamma^* p_V^* \sin^2(\theta^*/2) \quad (4.2)$$

where p_γ^* , p_V^* and θ^* are the photon and meson momenta and the angle between them in the photon-proton center-of-mass system and

$$t_0 = (M_N^2 - M_p^2 - Q^2 - M_V^2)^2 / 4W^2 - (p_\gamma^* - p_V^*)^2 \quad (4.3)$$

is the maximum $t(\theta^* = 0)$ value. For $Q^2 \ll -t, p_{V,T}^2, M_V^2, M_N^2 \ll W^2$, t and t_0 are given by

$$t \approx t_0 - p_{V,T}^2 \approx -M_V^2(M_N^2 - M_p^2) / W^2 - p_{V,T}^2 \quad (4.4)$$

where $p_{V,T}$ is the meson transverse momentum. Since the maximum $-t_0$ value in the kinematic range covered by this analysis is small ($-t_0 \leq 7 \cdot 10^{-3}$ GeV² for $V = \rho^0, \phi$ and $-t_0 \leq 6 \cdot 10^{-2}$ GeV² for $V = J/\psi$) compared to the $-t$ value, it can be neglected. The t is then given by

$$t \approx -p_{V,T}^2. \quad (4.5)$$

The derivations of the Eq. (4.2, 4.3 and 4.4) can be found in appendix A.

The energy E_V and momenta $p_{V,Z}, p_{V,T}$ are calculated from the measured three-momenta of the tracks observed in the CTD assuming that the tracks are pions, kaons or electrons for ρ, ϕ and J/ψ , respectively.

The approximation $Q^2 = 0$ is used to reconstruct the decay angles in the helicity frame. In addition no transverse momentum for the incoming positrons and protons is assumed.

4.2 Trigger

The positron and proton bunches collide at HERA every 96 ns. The ZEUS detector is required to detect the products of positron-proton collisions resulting from any of the 10^7 bunch crosses that occur per second. Most of the signals observed by ZEUS are background produced by interactions with residual gas in the beam pipe or cosmic rays which have much higher rates than that of positron-proton interactions. To cope with such rate of background events and to select efficiently physics events, there is a three level trigger system providing a final output rate of a few Hz. The first level trigger (FLT) is a hardware based trigger while the second (SLT) and the third (TLT) level trigger are software based. At the FLT the trigger decision is taken based on the global properties of an event, like energy sums, timing information or signals in the veto counters. The main task of the SLT is to identify and reject background events while the TLT runs part of the offline reconstruction code and allows sophisticated and reliable filtering of interesting events. Events which are accepted by the TLT are written to tape and can be used for offline analysis.

4.2.1 Trigger for vector meson events

The PT was installed at the beginning of the 1995 running period. The trigger for PT tagged vector mesons was optimized simultaneously with data taking so that only part of the 1995 luminosity is useful for physics analysis. The final trigger configuration was used for ZEUS runs since run 13348. The trigger demands the following requirements:

- At the FLT the candidates were identified by an energy deposit of more than ≈ 1 GeV in the PT (PT_{FLT}), at least one track candidate in the CTD (CTD_{FLT}), no vetoes from the ZEUS veto counters VW and C5, and less than 1250 MeV energy deposit in the innermost FCAL towers ring close to the beam pipe ($FCAL_{BP_{FLT}}$) (to remove proton beam gas interactions). An upper limit of 1 GeV on the energy deposited in the LUMI photon and electron ($LUMI_{VETO}$) calorimeters was also imposed. This requirement suppressed random overlays with bremsstrahlung events.
- The SLT included a restriction on the number of tracks and track segments in the CTD and a requirement on the vertex position if the vertex had been found (CTD_{SLT}). Further cuts allowed rejection of beam gas events and cosmic or halo muons.
- At the TLT the selected events had exactly one vertex within ± 60 cm of the IP with two tracks pointed to it and no tracks not associated to the vertex (CTD_{TLT})

4.2.2 Trigger efficiency

Any trigger inefficiencies which are not properly modeled in the MC simulation will result in wrong conclusions for physics analysis. Thus a correct simulation of the trigger is necessary. While the SLT and TLT can be verified using *pass through* events (i.e. the event is taken independently of any trigger decision) or *control trigger* events (i.e. some fraction of events with looser cuts than the nominal trigger are taken), this is difficult in the case of the FLT. Thus the main concern is to ensure the correct simulation of the FLT in the MC. The efficiencies of all sub-triggers were evaluated by an event sample obtained by requiring independent triggers.

Efficiency of the PT_{FLT}

The PT issues a trigger for events with energy deposit above approximately 1 GeV. The low threshold ensures that the tagging efficiency is determined mainly by the geometrical acceptance.

The PT acceptance for high energy positrons scattered under very small angles was studied with Bethe-Heitler events, $ep \rightarrow e'\gamma p$ as depicted in Fig. (4.2). Triggering on the events with a photon

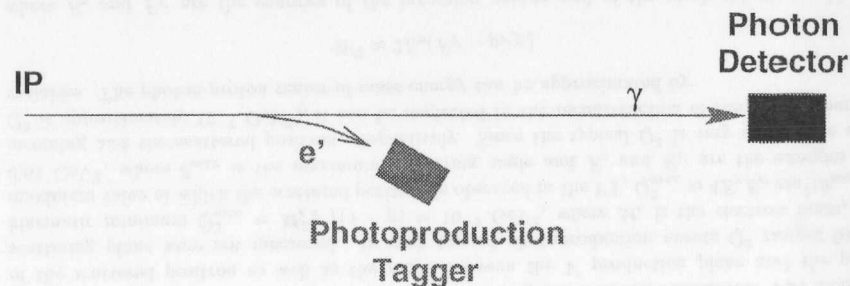


Figure 4.2: Sketch of the small angle positron and photon tagging system

measured in the LUMI photon detector the PT acceptance A_B was studied as a function of the measured photon energy in the LUMI. Fig. (4.3a) shows the distribution of the measured photon energy in the LUMI photon detector (non-shaded histogram) and the subsample of events with the positron measured in the PT (shaded histogram). The acceptance A_B is the ratio of these two distributions after correction for the multiple events (in which the photon and positron originated from different interactions) and after subtraction of the positron-gas contribution.

Thus the Monte Carlo program using the HERA beam transport matrices to simulate the scattered positron trajectory was tuned so as to achieve the best agreement with the data.

The PT_{FLT} efficiency for photoproduction events was then evaluated using events generated according to the equivalent photon approximation for positron scattering angles up to 3 mrad (for larger angles the acceptance is negligible) and were tracked through the HERA beam line. The fraction A_t of the positrons which passed the trigger was calculated as a function of the collision energy W (shown in Fig. (4.3b)). For the kinematical range used in this analysis the average PT acceptance was $70\% \pm 11\%$.

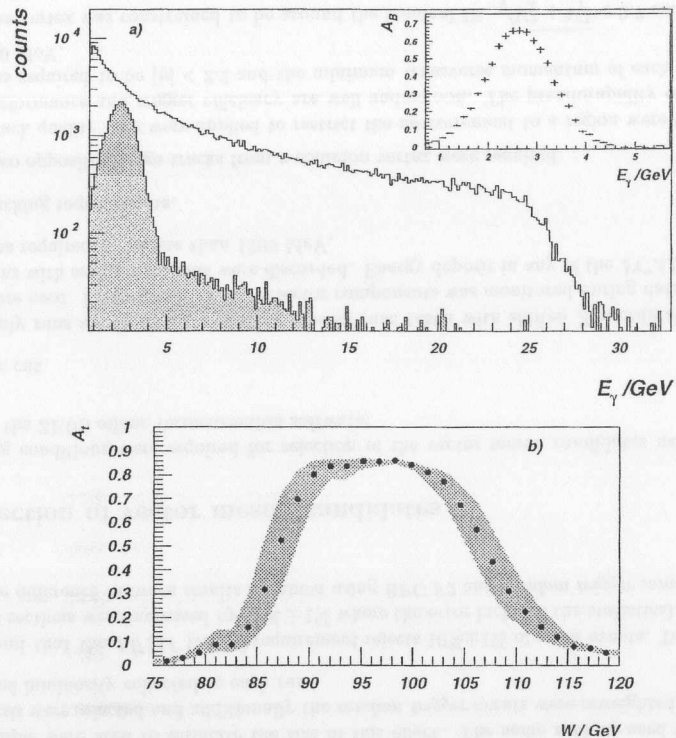


Figure 4.3: (a) The acceptance (crosses) of the PT as a function of the measured photon energy in LUMI for bremsstrahlung data. The histograms are explained in text. (b) The acceptance of the PT as a function of the collision energy W for photoproduction events. The shaded region represents the systematic uncertainty of the PT acceptance.

The procedure used to determine A_t and its systematic uncertainty is described in more details in [18].

In the analysis to account for the PT acceptance and efficiency the reconstructed Monte Carlo events were weighted with the function $A_t(W)$.

Efficiency of the $FCAL_{BP_{FLT}}$ veto

To study the efficiency of the $FCAL_{BP_{FLT}}$ veto an independent trigger (BPC F2) without $FCAL_{BP_{FLT}}$ was used.

The $FCAL_{BP_{FLT}}$ veto is set when there is more than 1250 MeV energy deposited in any of the eight FCAL towers surrounding the beam pipe. Since the energy thresholds of FLT triggers are not a step function, a cut on offline energy at 1200 MeV was introduced to obtain a good agreement between data and MC.

The efficiency of the $FCAL_{BP_{FLT}}$ as well as the FCAL tagging efficiency is sensitive to the position of the collimator C4 situated in front of the FCAL to reduce the radiation in the inner tracking

detectors and in the calorimeter. Further complication is that the position of this collimator is not precisely known and has been changing during running period. In the standard ZEUS MC simulation the collimator is opened. Therefore another MC sample with the closed collimator was generated to check the sensitivity of the results to the collimator position. Since the agreement between data and MC is better in the case of the open collimator, the final MC sample consisted of 67% of MC events with an open collimator and 33% of MC events with the collimator closed. The uncertainty on the collimator position was accounted for by increasing the contribution of MC events with the collimator closed to 67% and by decreasing it to 0%. Fig. (4.4) shows the $FCAL_{BP_{FLT}}$ veto inefficiency as a function of M_N^2 for both MC samples and its nominal mixture.

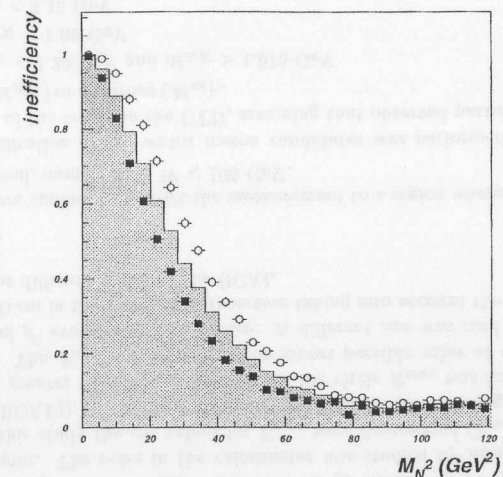


Figure 4.4: The inefficiency of the $FCAL_{BP_{FLT}}$ veto as a function of M_N^2 . The histogram corresponds to the mixture of 67% of MC events with an open collimator (squares) and 33% of MC events with a closed collimator (empty circles)

CTD trigger efficiency

The CTD trigger efficiencies were checked using the BPC F2 sample, which did not require any tracking information in the trigger. Since the CTD trigger efficiency depends on the topology of the two track events, all of the offline selection cuts described in the next section were applied to select ρ^0 events for BPC F2 data and MC sample. The trigger efficiency for data and MC was compared for each trigger level. Also *control triggers* with relaxed SLT and TLT CTD cuts was used to check CTD trigger efficiencies.

The CTD_{FLT} trigger efficiency was found to be $94 \pm 1.5\%$ for data and $88 \pm 0.5\%$ for Monte Carlo. The difference between data and Monte Carlo ($6 \pm 1.6\%$) does not depend on pseudorapidity¹ (η) of the

¹ $\eta = -\ln \tan \frac{\theta}{2}$ where θ is the polar angle of the track relative to the z-axis

tracks. The CTD_{SLT} trigger efficiency was 99% for both data and MC. The CTD_{TLL} trigger efficiency were found to be strongly dependent on almost all relevant variables for MC samples contrary to the results from BPC F2 and *control trigger* data. Therefore no TLL CTD cuts were finally required in the MC simulation.

The overall CTD trigger efficiencies (FLT, SLT and TLL in case of data and only FLT and SLT for Monte Carlo) were compared. Within the statistical error the differences between data and Monte Carlo ($3.5 \pm 2.0\%$) do not depend on any relevant variable, except for $M_{\pi\pi}$. For low and for high $M_{\pi\pi}$ events no difference between data and Monte Carlo is observed but the statistical error for data is 4%. The topology of the two track events (η distributions) for low $M_{\pi\pi}$ and for ϕ are similar, as well as for high $M_{\pi\pi}$ and for J/ψ events. Therefore the cross sections for ρ^0 were scaled down by 3.5% and no corrections were implemented for ϕ and J/ψ cross sections. The statistical errors 2% for ρ^0 and 4% for ϕ and J/ψ events are included in the systematic error of all cross sections measurements.

Veto counters

The signals in the veto counters are used to reject background events. If the background rate is high the accidental coincidences reduce also the rate of the interesting events. The *random trigger* and BPC F2 sample were used to estimate the size of this effect. The same runs as used in the vector meson analysis were selected and additionally the *random trigger* events were reweighted according to the integrated luminosity collected in each run.

It was found that the *LUMI VETO* requirement rejects $10\% \pm 1\%$ of good events. To account for this all cross sections were increased by $10\% \pm 1\%$ where the error includes the statistical uncertainty as well as the difference between results obtained using BPC F2 and *random trigger* samples.

4.3 Selection of vector meson candidates

The following conditions were required for selection of the vector meson candidates using the final output from the ZEUS offline reconstruction software:

- Generic cut
 1. Only runs above 13348, excluding special runs taken with shifted Z coordinate of the IP, were used. Performance of the detector components was monitored during data taking and runs with severe problems were discarded. Energy deposit in any of the *FCAL_BP* towers was required to be less than 1200 MeV.
- The tracking requirements.
 2. Two opposite-charge tracks from a common vertex were required.
 3. Track quality cuts were applied to restrict the measurement to a region where the detector performance and trigger efficiency are well understood. The pseudorapidity of each track was required to be $|\eta| < 2.2$ and the minimum transverse momentum of each track $p_T > 150$ MeV.
 4. The vertex was constrained to be around the nominal IP, $\sqrt{V_x^2 + V_y^2} < 0.7$ cm and $|V_z| < 40$ cm.
- The selection of the diffractive events.

step	events
1	183302
2	144490(79%)
3	108553(59%)
4	98671(54%)
5	58483(32%)
6	25446(14%)
7	$\rho^0(22823)$, $\phi(366)$ and $J/\psi(120)$

Table 4.1: The impact of the cuts applied to select vector meson events on the triggered data.

5. An efficient cut against background, when other particles (from the photon vertex) than the two tracks are observed in UCAL, is a cut on the maximum energy E_{max} of calorimeter cells that are not associated with the two tracks. This is achieved by applying a *matching* routine (TRKCLU [17]) associating the tracks in the CTD with the energy deposits in the UCAL. Each calorimeter cell inside a circle of radius R_{max} around the track is assigned to the tracks. It is required that E_{max} is below an energy which is given by the maximal noise in the calorimeter. The noise in the calorimeter was studied by using random triggered events. From this study the cut values for E_{max} were determined ($E_{max} < 200(250)$ MeV in the RCAL(BCAL)) by requiring that only 0.1% of all random trigger events have the maximal noise greater than E_{max} . The size of the circle R_{max} was fixed by studying the ρ^0 MC events. The R_{max} was chosen at the lowest possible value at which the efficiency of keeping good ρ^0 events starts to flatten. A different size was used in EMC and HAC ($R_{max} = 30(50)$ cm in the EMC(HAC)) section taking into account the different radial size of the shower at different depth in the UCAL.
- The kinematic cuts.
 6. The W cuts were applied to restrict the measurement to a region where the PT acceptance is well understood, namely $85 < W < 105$ GeV.
 7. The final identification of the vector meson candidates was performed using cuts on the invariant mass of the tracks in the CTD, assuming that observed particles are either pions ($M_{\pi\pi}$) kaons (M_{KK}) or electrons (M_{ee}).
 - ρ^0 $0.55 < M_{\pi\pi} < 1.20$ GeV and $M_{KK} > 1.075$ GeV
 - ϕ $0.99 < M_{KK} < 1.06$ GeV
 - J/ψ $2.98 < M_{ee} < 3.13$ GeV
 The cuts on the $M_{\pi\pi}$ were used to suppress the contribution from other vector mesons ($\omega \rightarrow \pi^+\pi^-\pi^0$ and $\rho'(1500) \rightarrow \pi^+\pi^-$). The cuts on M_{KK} and M_{ee} were chosen at the level of ± 3 typical mass resolution around the nominal reconstructed masses of ϕ and J/ψ to reduce the non-resonant background.

The number of events after each of the above selection steps are listed in Tab. (4.1) together with a fractional number of events, normalized to the number of events after the first step. The effectiveness of the cuts is displayed in Fig. (4.5a) where the invariant two pion mass spectrum is shown after subsequent application of the cuts. In Fig. (4.5a) contributions from ϕ , ω , ρ^0 , $\rho'(1500-1700)$ and J/ψ mesons are clearly visible. Fig. (4.5b,c,d) show the mass spectra of the selected events (before applying the invariant mass cut) with a clear ρ^0 , ϕ and J/ψ signal.

Fig.(4.6) shows the comparison of the measured pseudorapidity (η^+) and transverse momentum (p_T^+) of the positive tracks, W , helicity angles and V pseudorapidity (η_{VM}) distributions in the data

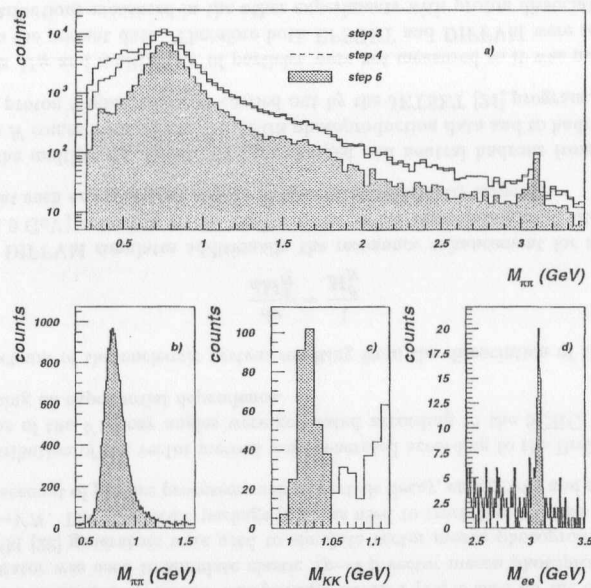


Figure 4.5: The invariant two-pion mass spectra (a) after subsequent application of the cuts 1-6. Contributions from ϕ , ω , ρ^0 , ρ' (1500–1700) and J/ψ mesons are clearly visible. Mass spectra $M_{\pi\pi}$ (b), M_{KK} (c) and M_{ee} (d) after all selection cuts (except for the mass cut). The shaded regions indicate the cuts on the invariant mass of the two tracks used to select ρ^0 , ϕ and J/ψ candidates.

with MC for ρ^0 , ϕ and J/ψ candidates. The selection cuts on the plotted variables were not applied and are indicated as a solid lines. The MC events were reweighted as described in the following chapter.

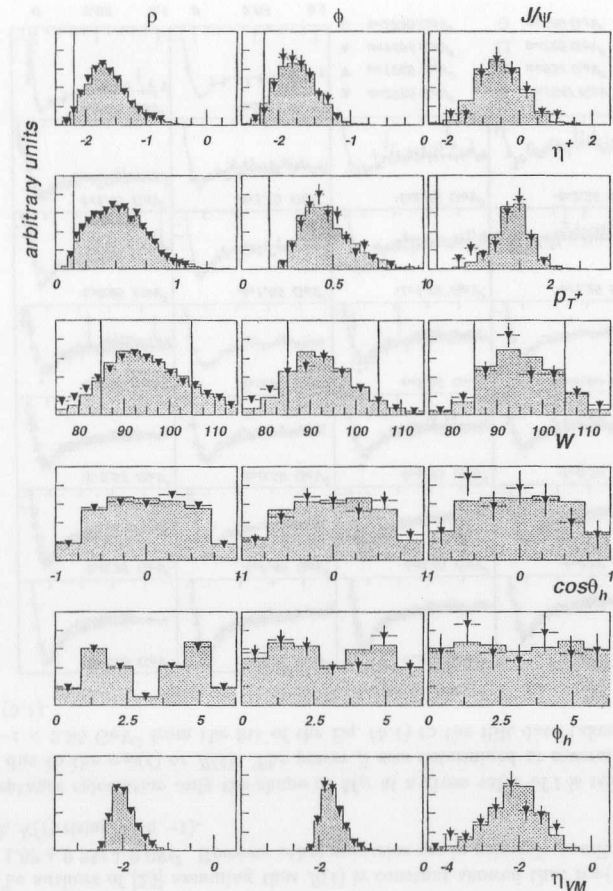


Figure 4.6: The comparison of the measured η^+ , p_T^+ , W , helicity angle and η_V distributions in the data with MC for ρ^0 , ϕ and J/ψ candidates. Points represent the data. The histograms correspond to the sum of elastic and proton-dissociative MC events. The solid lines correspond to the selection cuts.

Chapter 5

Monte Carlo simulation

In this chapter the Monte Carlo (MC) simulation programs used to study efficiency of the selection of the vector meson candidates are described.

5.1 Monte Carlo generators

The MC event and detector simulation is used to correct for acceptance and smearing effects due to the final resolution of the measurement. The package GEANT [19] is used for the detector simulation. DIPSI [20] generator was used to simulate elastic $\gamma p \rightarrow V p$ vector meson photoproduction. EPSOFT [21] and DIFFVM [22] generators were used to simulate vector meson photoproduction with proton dissociation $\gamma p \rightarrow V N$. The MOZART package [23] was used to track the particles through the whole detector taking account of physics processes such as particle decay, energy loss and multiple scattering.

The mass distribution of the vector mesons were generated according to the Breit-Wigner function. The distributions of the V decay angles were generated according to the SCHC. The t values were simulated assuming an exponential dependence.

The mass spectrum of the nucleonic system resulting from the dissociation of the proton was calculated as

$$\frac{d\sigma}{dM_N^2} \sim \frac{1}{M_N^\beta} \quad (5.1)$$

where $\beta = 2.0$. DIFFVM simulates additionally the resonance enhancement for a light dissociative system ($M_N < 1.9$ GeV) according to the results of the proton dissociation on deuteronium. However it is expected that such enhancement should disappear at sufficiently large $-t$.

In EPSOFT the multiplicity distribution for charged and neutral hadrons from the decay of the nucleonic system N comes from a fit to the ZEUS photoproduction data and to hadron-hadron results. In DIFFVM the proton fragmentation is carried out by the JETSET [24] program.

In this analysis M_N and multiplicity of particles were not measured so it was not possible to tune the simulation to the present data. Therefore both EPSOFT and DIFFVM were reweighted so as to describe M_N distributions measured in the other experiments with proton dissociation at large $-t$.

M_N evolution with t

Both EPSOFT and DIFFVM assume that there is no M_N evolution with t (β in Eq. (5.1) is t independent). It is in contrast to the results from proton-dissociative experiments as well as to the expectation from Regge theory. In the triple Regge theory at a fixed t the M_N distribution is given by (see Eq. (2.27))

$$\frac{d\sigma}{dM_N^2} \sim \left(\frac{1}{M_N^2}\right)^{2\alpha_{IP}(t)-1} \left[(M_N^2)^{\alpha_{IP}(0)-1} + R(t) \cdot (M_N^2)^{\alpha_R(0)-1} \right] \sim \left(\frac{1}{M_N}\right)^{\beta(t)} \quad (5.2)$$

The effective power β depends on both $\alpha_{IP}(t)$ and $R(t)$. Very little is known about $\alpha_{IP}(t)$ and $R(t)$ at high $-t$. The authors of [25] assuming that $R(t)$ is constant showed that $\alpha_{IP}(t)$ has a quadratic form $\alpha_{IP}(t) = 1.08 + 0.25t + 0.08t^2$. However other scenarios are in principle possible (linear pomeron trajectory with $R(t)$ rising with $-t$).

For the acceptance calculation only the shape of M_N at a given value of t is relevant. It does not matter if it is due to the $\alpha_{IP}(t)$ or $R(t)$. The power β was determined at several values of t in the range $0.15 < -t < 2.95$ GeV² from the fits of the Eq. (5.1) to the ISR data taken from [26] as it is shown in Fig. (5.1).

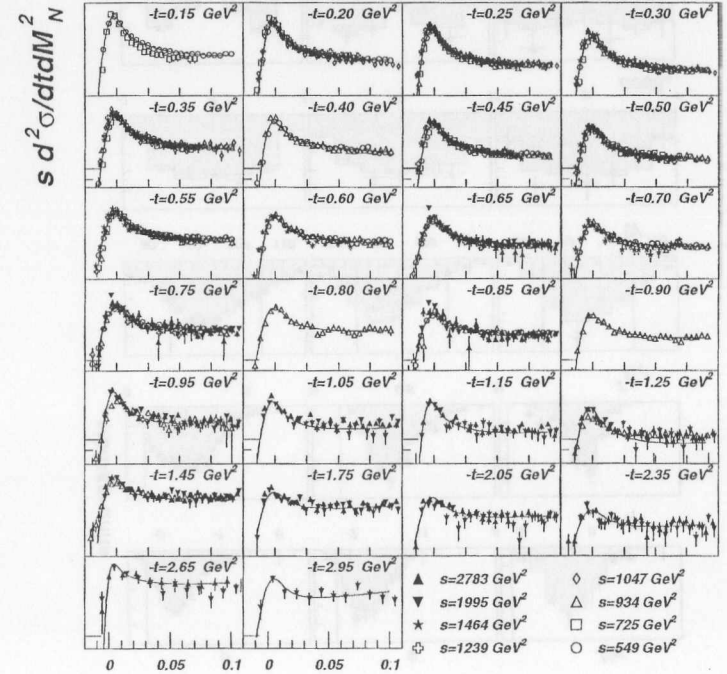


Figure 5.1: The invariant cross sections $s d^2\sigma/dtdM_N^2$ at fixed values of t as a function of M_N^2/s . The solid curves are the results of the fits with Eq. (5.1). Data were taken from [26]

Fig. (5.2) shows the dependence of the power β on t resulting from the fits shown in Fig. (5.1). Additionally the results of the CDF measurement [27] at $t \approx 0$ and UA8 [25] are presented. The solid curve is the best parameterization of $\beta(t)$ used later to reweight proton-dissociative MC samples for ρ^0 and ϕ mesons. The dashed curves represent the systematic uncertainty on $\beta(t)$ used to evaluate the systematic error due to the modeling proton dissociation.

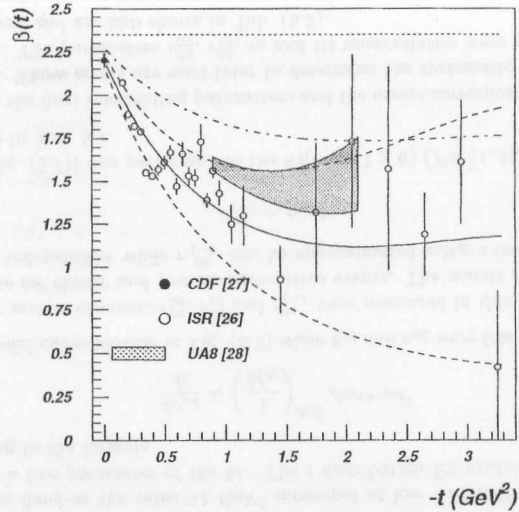


Figure 5.2: The effective power β as a function of $-t$ resulting from the fit of the formula $d\sigma/dM_N^2 \sim 1/M_N^\beta$ to the ISR data (empty circles). Also the result of the CDF measurement at $t \approx 0$ and UA8 are presented. The curves are explained in the text.

A different parameterization of β was assumed in the J/ψ MC with proton dissociation. The steep energy behavior of the elastic photoproduction cross section at HERA [31, 32] cannot be described in the Regge picture by a Pomeron trajectory with a universal intercept of $\alpha_P(0) = 1.08$ but requires a larger intercept. In addition, a direct determination of the Pomeron trajectory has shown that the slope α'_P from elastic photoproduction of J/ψ is much smaller than 0.25 GeV^{-2} [40]. Therefore as one of the systematic checks $\beta(t) = 2.35$ was assumed (the dotted line in Fig. (5.2)). The β value of 2.35 was obtained by putting $\alpha_P(t) = 1.175 + 0.0t$ and $R(t) = 0$ into Eq. (5.2). The nominal parameterization used in the ρ^0 and ϕ MC (solid curve) was also used as the second systematic check. As a nominal parameterization of $\beta(t)$ for the J/ψ meson the average of the above two parameterizations was taken (dashed-dotted curve in Fig. (5.2)).

Particle multiplicity of the proton dissociative system

The parameterization of the average ($\langle n \rangle$) and dispersion (D) of particle multiplicity as a function of M_N used in EPSOFT comes from the fit to the ZEUS photon-dissociative photoproduction data and to the hadron-hadron results. However those fits were performed at relatively high values of dissociative masses. It was found that the standard EPSOFT does not reproduce the multiplicity distributions

measured in the $pp \rightarrow pN$ experiments in the low M_N region. For the present data FCAL energy limitation in the trigger restricted the mass of the dissociative system $M_N < 5 - 8 \text{ GeV}$ therefore the correct simulation of the low M_N region is essential.

Therefore the modeling of the proton dissociation in the standard EPSOFT was improved, according to the results obtained in [41]. The multiplicity distributions for charged and neutral hadrons from the decay of the system N at a fixed mass M_N are assumed to be Gaussian

$$P(n) \sim \frac{1}{D} \exp\left(-\frac{(n - \langle n \rangle)^2}{2D^2}\right) \quad (5.3)$$

where $n = 1, 3, \dots$ (multiplicity of charged hadrons) and $n = 0, 1, 2, \dots$ (multiplicity of neutral hadrons) and

$$\langle n \rangle = \langle n \rangle_{ch} = 2\sqrt{(M_N - M_P)} \quad \text{for charged hadrons,} \quad (5.4)$$

$$\langle n \rangle = \langle n \rangle_{nu} = \sqrt{(M_N - M_P)} \quad \text{for neutral hadrons,} \quad (5.5)$$

$$\langle n \rangle / D = 2.0 \quad (5.6)$$

5.2 Comparison of MC with data

The analysis of the vector meson production is complicated due to the fact that the acceptance depends on all kinematic variables ($W, M_V, t, \phi_h, \cos\theta_h$). It is therefore important to have an MC simulation which is capable of reproducing the data to have confidence in the results.

To improve the agreement between data and MC in the reconstructed t, M_V and decay angular distributions, the MC was reweighted so as to minimize the differences between the measured data distributions and the reconstructed MC distributions.

The unknown parameters $\vec{\lambda}$ are given by the minima in χ^2 function with respect to all parameters $\vec{\lambda}$. Here variable χ^2 is defined as in [42]

$$\chi^2(\vec{\lambda}) = \sum_i \frac{(d_i - m_i(\vec{\lambda}))^2}{\sigma_i^2} \quad (5.7)$$

where d_i is the number of data events in bin i , $m_i(\vec{\lambda})$ the number of Monte Carlo events (mixture of elastic and proton-dissociative) determined with parameters $\vec{\lambda}$ in the corresponding bin and σ_i is the error assigned to the number of events in this bin. The sum in Eq. (5.7) runs through three dimensional (PD^T, t, M_V) bins, where $PD^T = 1$ for events tagged as the proton-dissociative by requiring a signal in the PRT1 (or FCAL) otherwise $PD^T = 0$. The data and MC events with $PD^T = 1$ are almost all proton-dissociative while events with $PD^T = 0$ are the mixture of elastic and proton-dissociative ones. This procedure allows to determine all parameters related to the t and M_V distributions separately for elastic and proton-dissociative events as well as the relative contributions of these two processes in the whole data sample. The minimalization was performed using the package MINUIT [43].

To improve the agreement between data and MC in the reconstructed angular distributions, the MC was reweighted in an iterative procedure. As the first step of this procedure the acceptance corrections were calculated using the MC generated according to the SCHC hypothesis and the spin density matrix elements were obtained as described in Sec. (6.3.3), Sec. (6.4.3) and Sec. (6.5.3). Then the procedure was repeated using the spin density matrix elements as measured in the first step. The whole procedure was repeated until the parameters converged.

5.2.1 Reweighting of the ρ^0 MC

Since the ρ^0 mass shape is skewed and since this skewing changes with t the ρ^0 MC was reweighted according to the Söding parameterization (see Eq. (6.4)), where parameter B/A depends on t . The dependence of the parameter B/A on t was parameterized as (see Sec. (7.1))

$$B/A = k_S e^{b_S t} . \quad (5.8)$$

The parameters k_S and b_S describe the ρ^0 mass shape as a function of t . The parameter k_S was fixed to the value 0.8 GeV^{-2} measured at low $-t$ ZEUS measurement [44] and only parameter b_S was a free parameter of the fit.

The contribution of the background events with photon dissociation (term $f = A_f(1 + 1.5M_{\pi\pi})$ in Eq. (6.4)) also changes with t (see Sec. (6.3.1)). The parameter A_f is treated as a free parameter which depends on t . The dependence of A_f on t was parameterized as

$$A_f = A_f^0 \cdot t . \quad (5.9)$$

M_ρ and Γ_0 were free parameters and were assumed to be independent on t . The parameters $k_S, b_S, M_\rho, \Gamma_0$ and A_f^0 , based on the results of this analysis, were assumed to be the same for elastic and proton-dissociative events.

The generated t distribution for elastic ρ^0 events was parameterized as suggested by the results of this analysis (see Sec. (7.1))

$$\frac{d\sigma_{el}}{dt} \sim \exp(b_{el}^l t) \quad \text{at } -t \leq 0.25 \text{ GeV}^2 , \quad (5.10)$$

$$\frac{d\sigma_{el}}{dt} \sim \exp(-b_{el}^l \cdot 0.25 + b_{el}^h(t + 0.25)) \quad \text{at } -t > 0.25 \text{ GeV}^2 . \quad (5.11)$$

The t -slope b_{el}^l was fixed at the value 11 GeV^2 measured at low $-t$ ZEUS measurement [45] while parameter b_{el}^h was a free parameter of the fit. The t distribution for proton-dissociative events was generated according to the formula

$$\frac{d\sigma_{pd}}{dt} \sim \left(\frac{1}{M_N} \right)^{\beta(t)} e^{b_{pd}t + c_{pd}t^2} \quad (5.12)$$

where $\beta(t)$ is the solid curve plotted in Fig. (5.2) while b_{pd} and c_{pd} were free parameters of the fit.

The spin density matrix elements r_{00}^{04}, r_{10}^{04} and r_{1-1}^{04} were measured in this analysis (see Sec. (7.1)) and taken the same for elastic and proton-dissociative events. The matrix elements r_{00}^{04} and r_{10}^{04} were found to be t independent while r_{1-1}^{04} can be approximated using a linear function

$$r_{1-1}^{04} = r_0 \cdot t . \quad (5.13)$$

The χ^2 fit (see Eq. (5.7)) was performed to the $84(=2 \times 7 \times 6)$ ($PD^T, t, M_{\pi\pi}$) bins. The t and $M_{\pi\pi}$ bin limits are given in Tab. 5.1.

Tab. (5.2) shows the final reweighting parameters and the errors corresponding to a change by one standard deviation. These errors are used later to determine the systematic error due to changes in the MC simulation. The parameters $r_{00}^{04}, r_{10}^{04}, r_0$ and its uncertainties were obtained from the fit to results of this analysis and are also shown in Tab. (5.2).

As an example of the agreement reached between data and MC after reweighting the ρ^0 MC, various distributions ($t, W, M_{\pi\pi}, \cos\theta_h$ and ϕ_h) of ρ^0 candidates as reconstructed in the data and in MC are shown in Fig. (5.3). The distributions are presented in four t bins. The agreement between data and MC is satisfactory. The proton-dissociative process dominates at large $-t$.

$-t$ (GeV ²)		$M_{\pi\pi}$ (GeV)	
lower limit	upper limit	lower limit	upper limit
0.30	0.50	0.55	0.67
0.50	0.70	0.67	0.75
0.70	0.90	0.75	0.82
0.90	1.15	0.82	0.90
1.15	1.50	1.00	1.20
1.50	2.20		
2.20	4.20		

Table 5.1: $M_{\pi\pi}$ and $-t$ bin limits used to obtain parameters of the ρ^0 MC.

parameter	optimal value	range corresponding to one standard deviation	
M_ρ	766 MeV	763 MeV	769 MeV
Γ_0	152 MeV	146 MeV	152 MeV
A_f^0	-0.06 GeV ⁻³	-0.09 GeV ⁻³	-0.03 GeV ⁻³
b_{el}^h	6.4 GeV ⁻²	6.2 GeV ⁻²	6.6 GeV ⁻²
b_{pd}	0.72 GeV ⁻²	0.69 GeV ⁻²	0.75 GeV ⁻²
c_{pd}	-0.28 GeV ⁻⁴	-0.26 GeV ⁻⁴	-0.30 GeV ⁻⁴
b_S	1.7	1.5	1.9
r_{00}^{04}	0.06	0.03	0.09
r_{10}^{04}	0.06	0.04	0.08
r_0	0.07	0.05	0.09

Table 5.2: The final reweighting parameters of the ρ^0 MC.

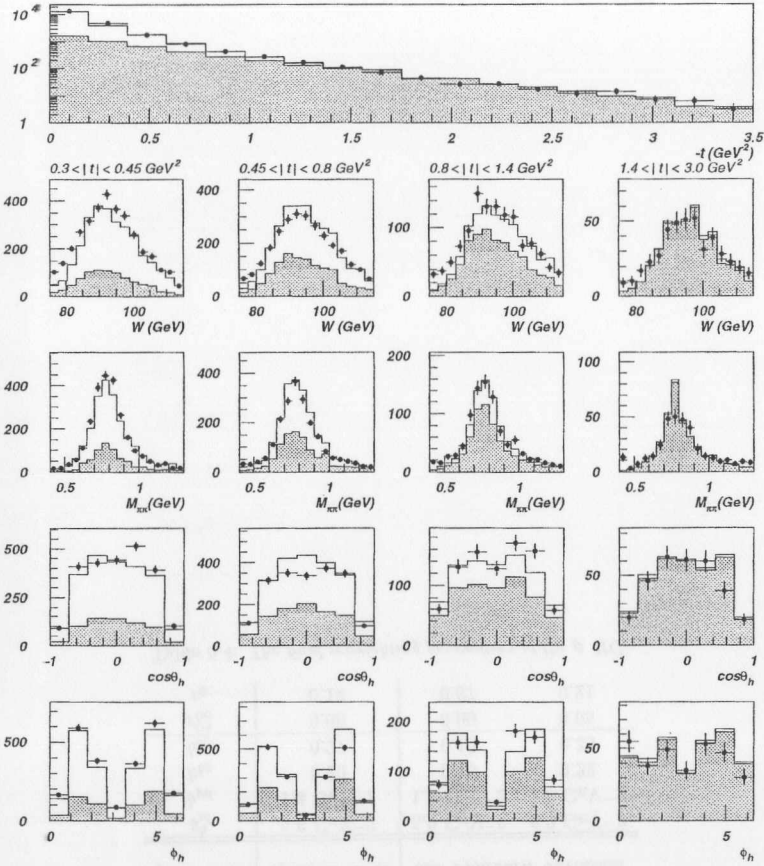


Figure 5.3: The t , W , $M_{\pi\pi}$, $\cos\theta_h$ and ϕ_h distributions of ρ^0 candidates as reconstructed in the data and in MC. The distributions are presented in four t bins. Points represent the data. Empty histograms correspond to the sum of elastic and proton-dissociative MC events. Shaded histograms are proton-dissociative MC events.

5.2.2 Reweighting of the ϕ MC

The study of the ϕ mass distribution for the completeness of the results are presented together with other results in chapter 6. Since the non-resonant background under ϕ signal cannot be neglected it has to be accounted for in the reweighting procedure. The results presented in Sec. (6.4.1) show that the background to the ϕ signal is well described by equation $A_{BG} (M_{KK} - 2M_K)^\Delta$ where Δ is almost t independent. In the χ^2 fit (see Eq. (5.7)) data distributions were compared to the MC distributions after background subtraction. The background contribution in the chosen ϕ signal region was parameterized as a function of t with a form

$$C_{bg}(t) = k_{bg} \cdot e^{b_{bg}t} . \quad (5.14)$$

The parameters Δ , k_{bg} and b_{bg} were free in the fit and assumed to be the same for elastic and proton-dissociative events. The t and M_{KK} bin limits are given in Tab. (5.3). Eq. (5.14) gives the background contribution in the ϕ signal region (first M_{KK} bin listed in Tab. (5.3)). The M_{KK} bins outside ϕ signal region were used to constrain Δ and $C_{bg}(t)$.

$-t$ (GeV ²)		M_{KK} (GeV)	
lower limit	upper limit	lower limit	upper limit
0.4	0.6	0.99	1.06
0.6	0.8	1.06	1.09
0.8	1.4	1.09	1.12
1.4	4.0	1.12	1.15

Table 5.3: M_{KK} and $-t$ bin limits used to obtain parameters of the ϕ MC.

Similarly as for ρ^0 , the generated t distribution for elastic ϕ events was parameterized as suggested by the results of this analysis (see Sec. (7.1))

$$\frac{d\sigma_{el}}{dt} \sim \exp(b_{el}^l t) \quad \text{at } -t \leq 0.35 \text{ GeV}^2, \quad (5.15)$$

$$\frac{d\sigma_{el}}{dt} \sim \exp(-b_{el}^l \cdot 0.35 + b_{el}^h(t + 0.35)) \quad \text{at } -t > 0.35 \text{ GeV}^2 . \quad (5.16)$$

The t -slope b_{el}^l was fixed at the value 7.3 GeV^2 measured at low $-t$ ZEUS measurement [46] while parameter b_{el}^h was a free parameter of the fit. The t distribution for proton-dissociative events was generated according to

$$\frac{d\sigma_{pd}}{dt} \sim \left(\frac{1}{M_N}\right)^{\beta(t)} e^{b_{pd}t} \quad (5.17)$$

where $\beta(t)$ is the solid curve plotted in Fig. (5.2) while b_{pd} was one of the free parameters of the fit.

The spin density matrix elements r_{00}^{04} and r_{1-1}^{04} were measured in this analysis (see Sec. (7.1)) and taken the same for elastic and proton-dissociative events. The matrix element r_{00}^{04} was found to be t independent while r_{1-1}^{04} can be approximated using a linear function

$$r_{1-1}^{04} = r_0 \cdot t . \quad (5.18)$$

The matrix element r_{10}^{04} was not measured and taken from SCHC, namely $r_{10}^{04} = 0$.

Tab. 5.4 shows the final reweighting parameters and the errors corresponding to a change by one standard deviation as obtained from the χ^2 fit (see Eq. (5.7)) to the $32(=2 \times 4 \times 4)$ ($PD^T, t, M_{\pi\pi}$) bins.

These errors are used later to determine the systematic error due to changes in the MC simulation. The parameters r_{00}^{04} and r_0 and its uncertainty were obtained from the fit to results of this analysis and are also shown in Tab. 5.4.

As an example of the agreement reached between data and MC after reweighting the ϕ MC, various distributions (t , W , $\cos\theta_h$ and ϕ_h) of ϕ candidates as reconstructed in the data and in MC are shown in Fig. (5.4). The distributions are presented in four t bins. The agreement between data and MC is satisfactory. The proton-dissociative process dominates at large $-t$.

parameter	optimal value	range corresponding to one standard deviation	
		5.0 GeV ⁻²	6.2 GeV ⁻²
b_{el}^h	5.6 GeV ⁻²	5.0 GeV ⁻²	6.2 GeV ⁻²
b_{pd}	1.3 GeV ⁻²	1.1 GeV ⁻²	1.5 GeV ⁻²
k_{bg}	0.20	0.18	0.22
b_{bg}	0.27	0.19	0.35
r_{00}^{04}	0.00	0.00	0.05
r_0	0.14	0.07	0.21

Table 5.4: The final reweighting parameters of the ϕ MC.

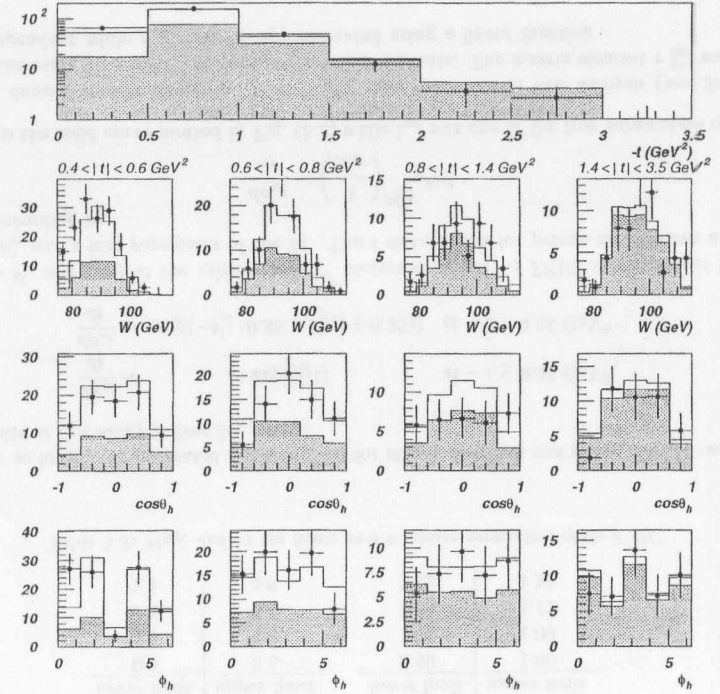


Figure 5.4: The t , W , $\cos\theta_h$ and ϕ_h distributions of ϕ candidates as reconstructed in the data and \bar{u} in MC. The distributions are presented in four t bins. Points represent the data. Empty histograms correspond to the sum of elastic and proton-dissociative MC events. Shaded histograms are proton-dissociative MC events.

5.2.3 Reweighting of the J/ψ MC

Similarly as for ϕ meson the non-resonant background under J/ψ signal was accounted for in the reweighting procedure. The results presented in Sec. (6.5.1) shows that the background to the J/ψ signal is well described by equation $A_{BG} \cdot (1 + \Delta M_{ee})$ where Δ is almost t independent. In the χ^2 fit (see Eq. (5.7)) the data distributions were compared to the MC distributions after background subtraction. The background contribution in the chosen J/ψ signal region was assumed to be t independent

$$C_{bg}(t) = k_{bg} \quad (5.19)$$

The parameters Δ and k_{bg} were free in the fit and assumed to be the same for elastic and proton-dissociative events. The t and M_{ee} bins limits are given in Tab. (5.5). Eq. (5.19) gives the background contribution in the J/ψ signal region (second M_{ee} bin listed in Tab. 5.5). The M_{ee} bins outside ϕ signal region were used to constrain Δ and C_{bg} .

$-t$ (GeV ²)		M_{ee} (GeV)	
lower limit	upper limit	lower limit	upper limit
0.1	0.5	2.40	2.98
0.5	1.2	2.98	3.13
1.2	4.0	3.13	3.50

Table 5.5: M_{ee} and $-t$ bin limits used to obtain parameters of the J/ψ MC.

The generated t distribution for elastic J/ψ events was parametrized as suggested by the results of this analysis (see Sec. (7.1))

$$\frac{d\sigma_{el}}{dt} \sim e^{b_{el}t} \quad (5.20)$$

The t -slope b_{el} was a free parameter of the fit. The t distribution for proton-dissociative events was generated according to

$$\frac{d\sigma_{pd}}{dt} \sim \left(\frac{1}{M_N}\right)^{\beta(t)} e^{b_{pd}t} \quad (5.21)$$

where $\beta(t)$ is the dashed-dotted curve plotted in Fig. (5.2) while b_{pd} was free parameters of the fit.

The spin density matrix elements r_{00}^{04} and r_{1-1}^{04} were measured in this analysis (see Sec. (7.1)) and taken the same for elastic and proton-dissociative events. The matrix element r_{00}^{04} was found to be t independent while r_{1-1}^{04} can be approximated using a linear function

$$r_{1-1}^{04} = r_0 \cdot t \quad (5.22)$$

The matrix element r_{10}^{04} was not measured and taken from SCHC, namely $r_{10}^{04} = 0$.

The Tab. (5.6) shows the final reweighting parameters and the errors corresponding to a change by one standard deviation as obtained from the χ^2 fit (see Eq. (5.7)) to the $18(=2 \times 3 \times 3)$ (PD , T , M_{ee}) bins. These errors are used later to determine the systematic error due to changes in the MC simulation. The parameters r_{00}^{04} and r_0 and their uncertainties were obtained from the fit to results of this analysis and are also shown in Tab. (5.6).

As an example of the agreement reached between data and MC after reweighting the J/ψ MC, various distributions (t , W , $\cos\theta_h$ and ϕ_h) of J/ψ candidates as reconstructed in the data and in MC are shown in Fig. (5.5). The distributions are presented in two t bins. The agreement between data and MC is satisfactory.

parameter	optimal value	range corresponding to one standard deviation	
b_{el}	4.3 GeV ⁻²	3.3 GeV ⁻²	5.3 GeV ⁻²
b_{pd}	0.3 GeV ⁻²	0.1 GeV ⁻²	0.5 GeV ⁻²
k_{bg}	0.16	0.13	0.19
r_{00}^{04}	0.08	0.00	0.30
r_0	0.15	0.05	0.25

Table 5.6: The final reweighting parameters of the J/ψ MC.

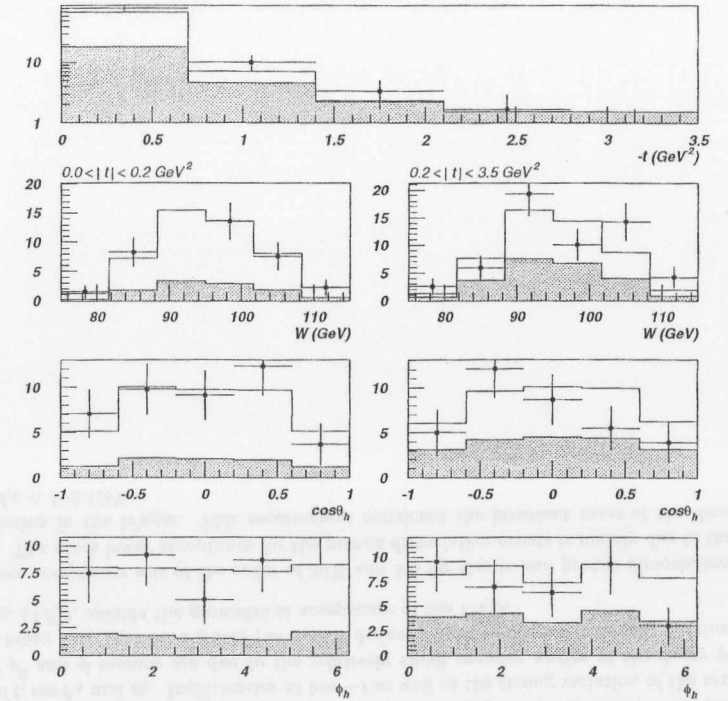


Figure 5.5: The t , W , $\cos\theta_h$ and ϕ_h distributions of J/ψ candidates as reconstructed in the data and in MC. The distributions are presented in two t bins. Points represent the data. Empty histograms correspond to the sum of elastic and proton-dissociative MC events. Shaded histograms are proton-dissociative MC events.

5.3 Resolution and acceptance

5.3.1 Resolution

Fig. (5.6) shows the resolution for the variables: t , W , $\cos\theta_h$, ϕ_h and M_V as a function of reconstructed $-t$ for ρ^0 , ϕ and J/ψ mesons. Generally the resolution for all the variables improves with increasing $-t$ since both tracks cross more CTD super layers as $-t$ increases. The angular resolutions deteriorate significantly if the tracks from the V decay are not well spatially separated. This is the case for the ϕ meson where opening angles between the two kaons are relatively small. In Tab. 5.7 the typical resolutions are listed. There are no systematical differences between reconstructed and generated variables except for the low $-t$ region for the ϕ meson (excluded from the analysis) and mass reconstruction for the J/ψ meson. The radiation of the photons from electrons in the magnetic field caused a systematic shift (50 MeV) in the reconstructed mass of J/ψ observed in the $J/\psi \rightarrow e^+e^-$ decay channel.

variable	typical resolution		
	ρ^0	ϕ	J/ψ
t (GeV^2)	0.20	0.15	0.15
W (GeV)	6	3	1
$\cos\theta_h$	0.08	0.20	0.02
ϕ_h (rad)	0.08	0.12	0.05
M_V (MeV)	50	10	25

Table 5.7: The typical resolutions for the variables: t , W , $\cos\theta_h$, ϕ_h and M_V for ρ^0 , ϕ and J/ψ mesons.

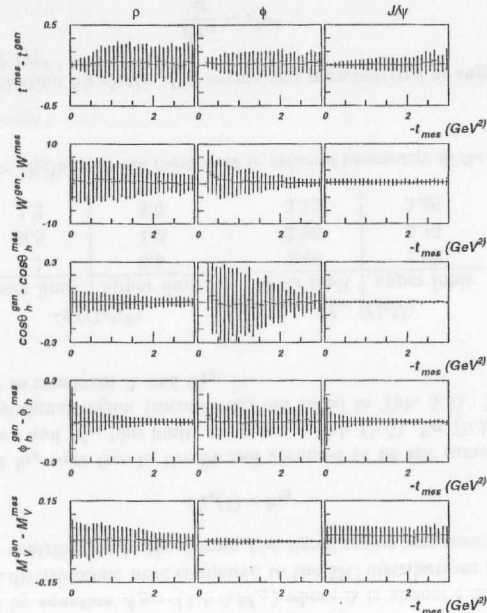


Figure 5.6: The resolution for the variables: t , W , $\cos\theta_h$, ϕ_h and M_V as a function of reconstructed $-t$ for ρ^0 , ϕ and J/ψ mesons.

5.3.2 Acceptance

The acceptance in a given bin was determined as the ratio of the number of accepted Monte Carlo events to the number of the generated events in the selected kinematic range. The acceptance calculated in this manner accounts for the geometric acceptance, the detector and reconstruction efficiencies, the detector resolution and, the trigger efficiency.

Fig. (5.7) shows the overall acceptance for proton dissociative (squares) and elastic events (circles) as a function of t , $\cos\theta_h$ and ϕ_h . Inefficiencies at low $-t$ as well as the strong variation of the acceptance with ϕ_h for ρ^0 and ϕ mesons are due to the relatively small opening angles of the decay particles, resulting in many very backward tracks (as can be deduced from the pseudo-rapidity distributions of tracks in Fig. (4.6)), outside the geometrical acceptance of the CTD.

The average acceptance was of the order of 30% and 5% for elastic and proton dissociative events, respectively. The much lower acceptance for the proton dissociative events is mainly due to the FCAL energy limitation in the trigger. This requirement restricted the invariant mass of the dissociative system to $M_N < 5-8$ GeV.

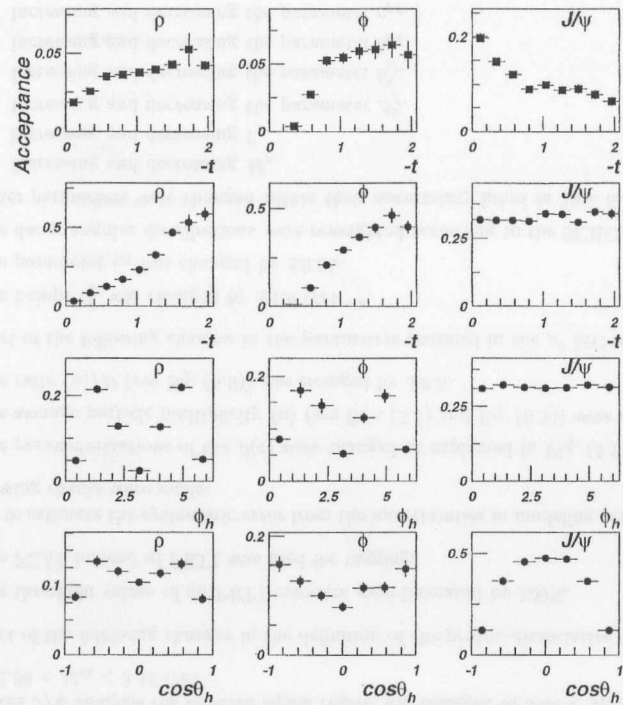


Figure 5.7: The overall acceptance for proton dissociative (squares) and elastic samples (circles) as a function of t , $\cos\theta_h$ and ϕ_h . For the angular distributions the shape of the acceptance plots are the same for elastic and proton-dissociative events.

Chapter 6

Results

The differential cross sections $d\sigma/dw$ ($w = t, M_V, \cos\theta_h, \phi_h$) for elastic and proton-dissociative photo-production of the ρ^0 , ϕ and J/ψ mesons, were evaluated in each bin of variable w as

$$\frac{d\sigma}{dw}(\gamma p \rightarrow Vp) = \frac{N_{data} \cdot (1 - C_D) \cdot C_{res}}{A \cdot \mathcal{L} \cdot \Phi_\gamma \cdot \Delta w \cdot C_{br}} \quad (6.1)$$

$$\frac{d\sigma}{dw}(\gamma p \rightarrow VN) = \frac{N_{data} \cdot C_D \cdot C_{res}}{A \cdot \mathcal{L} \cdot \Phi_\gamma \cdot \Delta w \cdot C_{br}} \quad (6.2)$$

where N_{data} is the number of observed vector meson candidates in bin Δw after all selection cuts, C_D is the contribution of the proton-dissociative events in the bin, C_{br} is the branching ratio of the observed vector meson decay mode, A is the acceptance in the bin, \mathcal{L} the integrated luminosity, $\Phi_\gamma = \int \int \Gamma(y, Q^2) dy dQ^2$ is the photon flux integrated over the y and Q^2 range covered by this measurement and Δw is the bin width.

The effective photon flux for $Q^2 < 0.02 \text{ GeV}^2$ and $85 < W_{\gamma p} < 105 \text{ GeV}$ is $\Phi_\gamma = 0.0121$. The integrated luminosity of the data sample is 1.98 pb^{-1} . The branching ratios C_{br} are 1, 0.5 and 0.12 for ρ^0 , ϕ and J/ψ respectively.

Some results of this analysis (ρ^0 mass shape analysis, helicity analysis and the ratios of cross sections $\rho^0: \phi: J/\psi$) are within errors the same for elastic and proton-dissociative processes. These similarities indicate that the data are consistent with the hypothesis of factorization of the diffractive vertices. Assuming factorization the differential cross sections for diffractive vector meson production without separation of elastic and proton-dissociative events were calculated according to the formula

$$\frac{d\sigma}{dw}(\gamma p \rightarrow VX) = \frac{N_{data} \cdot C_{res}}{A \cdot \mathcal{L} \cdot \Phi_\gamma \cdot \Delta w \cdot C_{br}} \quad (6.3)$$

where X is either the proton or higher mass nucleonic state N and the acceptance is determined from a mixture of elastic and proton-dissociative MC events.

6.1 Estimate of systematic uncertainties

The systematic checks were subdivided into those related to the selection procedure and those reflecting the uncertainty in the model used for the Monte Carlo generator.

- Assuming the conditions requested for selection of vector meson candidates described in Sec. (4.3) the effect of the following changes was checked:

1. The tighter ($p_T > 200$ MeV and $|\eta| < 2.1$) and looser ($p_T > 100$ MeV and $|\eta| < 2.3$) track quality cuts were applied.
 2. The tighter ($|V_Z| < 35$ cm and $\sqrt{V_X^2 + V_Y^2} < 0.5$ cm) and looser ($|V_Z| < 45$ cm and $\sqrt{V_X^2 + V_Y^2} < 1.0$ cm) vertex position cuts were employed.
 3. The radii R_{max} were changed to 25(45) cm EMC(HAC) and to 35(55) cm EMC(HAC).
 4. The maximum energy E_{max} was changed to 200(150) MeV BCAL(RCAL) and to 300(250) MeV BCAL(RCAL).
 5. In the ρ^0 analysis the selected signal region was changed to $0.6 < M_{\pi\pi} < 1.15$ GeV and to $0.5 < M_{\pi\pi} < 1.25$ GeV.
 6. In the ϕ analysis the selected signal region was changed to $1.00 < M_{KK} < 1.05$ GeV and to $0.98 < M_{KK} < 1.07$ GeV.
 7. In the J/ψ analysis the selected signal region was changed to $3.00 < M_{ee} < 3.11$ GeV and to $2.96 < M_{ee} < 3.15$ GeV.
- The effect of the following changes in the definition of the proton-dissociative tag were checked:
 8. The threshold values of all PRT1 counters were increased by 100%.
 9. The FCAL instead of PRT1 was used for tagging.
 - In order to estimate the systematic error from the uncertainties in modeling proton dissociation, the following checks were made:
 10. The parameterizations of the $\beta(t)$ were changed as explained in Fig. (5.2).
 11. The average particle multiplicity $\langle n \rangle$ (see Eq.s (5.4) and Eq. (5.5)) were changed by ± 0.4 .
 12. The ratio $\langle n \rangle / D$ (see Eq. (5.6)) was changed by ± 0.5 .
 - The effect of the following changes in the parameters assumed in the ρ^0 MC was checked:
 13. The t-slope b_{el}^t was changed by ± 1.0 GeV⁻².
 14. The parameter k_S was changed by ± 0.05 .
 15. The decay angular distributions were reweighted according to the SCHC.
 - Other parameters were changed within their uncertainty listed in Tab. 5.2
 - 16. Increasing and decreasing M_ρ .
 - 17. Increasing and decreasing Γ_ρ .
 - 18. Increasing and decreasing the parameter A_f^0 .
 - 19. Increasing and decreasing the parameter b_{el}^h .
 - 20. Increasing and decreasing the parameter b_{pd} .
 - 21. Increasing and decreasing the parameter c_{pd} .
 - 22. Increasing and decreasing the parameter b_S .
 - 23. Increasing and decreasing r_{00}^{04} .
 - 24. Increasing and decreasing r_{10}^{04} .
 - 25. Increasing and decreasing the parameter r_0 .
 - The effect of the following changes in the parameters assumed in the ϕ MC was checked:
 26. The t-slope b_{el}^t was changed by ± 1.0 GeV⁻².
 27. The decay angular distributions were reweighted according to the SCHC.

- Other parameters were changed within their uncertainty listed in Tab. 5.4
 28. Increasing and decreasing the parameter b_{el}^h .
 29. Increasing and decreasing the parameter b_{pd} .
 30. Increasing and decreasing the parameter k_{bg} .
 31. Increasing and decreasing the parameter b_{bg} .
 32. Increasing and decreasing r_{00}^{04} .
 33. Increasing and decreasing the parameter r_0 .
- The effect of the following changes in the parameters assumed in the J/ψ MC were checked:
 34. The decay angular distributions were reweighted according to the SCHC.
 - Other parameters were changed within their uncertainty listed in Tab. 5.6
 - 35. Increasing and decreasing the parameter b_{el} .
 - 36. Increasing and decreasing the parameter b_{pd} .
 - 37. Increasing and decreasing the parameter k_{bg} .

- Other error sources in addition to the errors estimated with the checks above:
 38. Uncertainty on the FCAL-BPFLT trigger efficiency accounted for by changing the relative contribution of the MC events with open and closed collimator in front of the FCAL as described in Sec. (4.2).
 39. Uncertainty on the PTFLT trigger efficiency accounted for by using different parameterization of the A_t as described in Sec. (4.2).
 40. Uncertainty on the CTD trigger efficiency.
 41. Uncertainty on radiative corrections.
 42. Uncertainty on the luminosity measurement.

For all the results quoted in the following the systematic uncertainty was determined through repeating the full analysis for each systematic check. For checks: 1-4,6-15,26,27,34,38,39 the analysis was repeated starting from the reweighting of the MC samples as described in chapter 5. For all other checks (except for 40,41,42) the analysis was repeated by changing only one parameter and keeping all others at the nominal value. The systematic errors due to the checks: 40, 41 and 42 were evaluated independently without repeating the analysis.

The errors due to the checks: 10, 11 and 12 are strongly correlated between different t bins. Therefore on all the plots these errors summed in quadrature are indicated as a shaded band and are not included in the systematic error.

The effect of checks: 39,40,41,42 has been considered to be independent of the variables under study and contributes therefore to an overall normalization error, which is not shown on the plots. The overall normalization error (17 %) is dominated by the uncertainty in the PT acceptance (16 %). It has been assumed that the overall normalization error does not affect the mass shape and helicity analysis as well as the measurements of the ratios of cross sections.

6.2 Separation of elastic and proton-dissociative processes.

The selected samples of the diffractively produced vector mesons are mixtures of elastic and proton-dissociative events. Proton-dissociative events were tagged by requiring a signal in one of the PRT1

counters above a threshold corresponding to the signal of a minimum ionizing particle signal. Alternatively, for systematic checks, energy deposits in the FCAL towers close to the beam pipe were also used for tagging the proton-dissociative events. In fact the proton-dissociative events where no energy is deposited in the forward direction are experimentally not distinguishable from the elastic ones on an event-by-event basis. Therefore these two processes have been separated on a statistical basis using MC simulation.

Since the non-diffractive background was negligible, the following relation was assumed

$$\frac{N_{pd,data}^T}{N_{pd,data}} = \frac{N_{pd,MC}^T}{N_{pd,MC}}$$

where $N_{pd,data}^T$ and $N_{pd,MC}^T$ are the numbers of the tagged proton-dissociative events, whereas $N_{pd,data}$ and $N_{pd,MC}$ are the numbers of all the observed proton-dissociative events in the data and proton-dissociative EPSOFT sample, respectively. The unknown numbers of the observed proton-dissociative events are equal:

$$N_{pd,data} = N_{pd,data}^T \frac{N_{pd,MC}^T}{N_{pd,MC}}$$

Therefore, the fraction C_D of proton-dissociative events in the data could be calculated

$$C_D \equiv \frac{N_{pd,data}}{N_{data}} = \frac{N_{pd,data}^T}{N_{data}} \frac{N_{pd,MC}^T}{N_{pd,MC}}$$

where N_{data} is the number of all observed diffractive events (elastic and proton-dissociative) in a given t bin in the data. In Fig. (6.1) the observed fraction of PRT1 tags (R_D) in the data and in the proton-dissociative MC as well as the estimated fraction of proton dissociative events C_D are displayed separately for the ρ^0 , ϕ and J/ψ samples. The same procedure was used for separation of the elastic and proton-dissociative processes in the ρ^0 mass shape and helicity analysis.

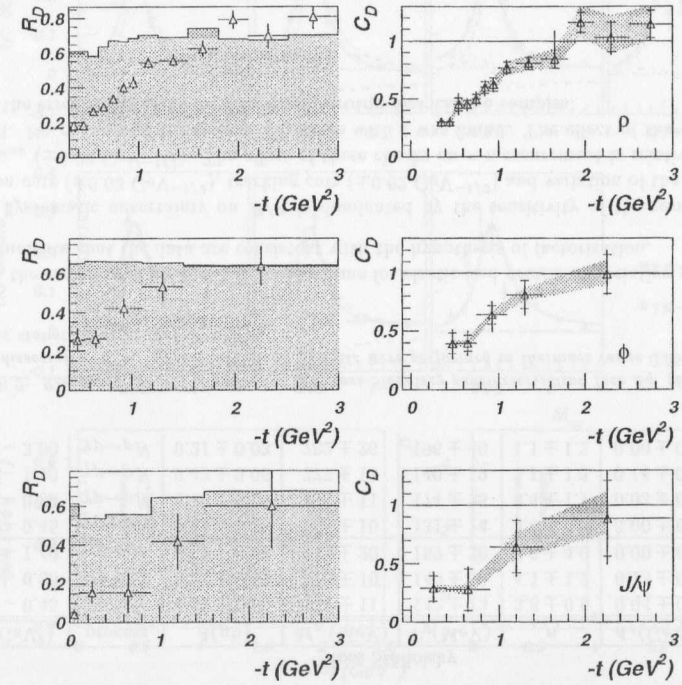


Figure 6.1: Observed fraction of PRT1 tags (R_D) in data (triangles with statistical error bars) and in the proton-dissociative MC (shaded histogram) and the estimated fraction of proton dissociative events in data, C_D , in the ρ^0 (upper), ϕ (middle) and J/ψ (lower) samples as a function of $-t$. The inner error bars indicate the statistical error, the outer bars the statistical and systematic errors added in quadrature. The shaded bands represent the size of the correlated errors due to modeling of the proton-dissociation in the Monte Carlo

6.3 ρ^0 photoproduction

6.3.1 Mass distribution

The differential cross section $d\sigma/dM_{\pi\pi}$ for elastic and proton-dissociative $\pi^+\pi^-$ photoproduction was calculated according to Eq. (6.1) and E1. (6.2). The proton-dissociative contribution, C_D was determined as described in Sec. (6.2) as a function of $M_{\pi\pi}$. The resonant and nonresonant $\pi^+\pi^-$ photoproduction was studied together therefore the C_{res} in Eq. (6.1) and Eq. (6.2) was set to unity.

The differential cross sections $d\sigma/dM_{\pi\pi}$ have been fitted using a parameterization inspired by the Söding model [47] where the p-wave relativistic Breit-Wigner (BW) shape is distorted by interference with non-resonant $\pi\pi$ production

$$\frac{d\sigma}{dM_{\pi\pi}} = A^2 \left[\left| \frac{\sqrt{M_{\pi\pi} M_\rho \Gamma_\rho}}{M_{\pi\pi}^2 - M_\rho^2 + i M_\rho \Gamma_\rho} + B/A \right|^2 + f \right] \quad (6.4)$$

with M_ρ the ρ^0 mass and Γ_ρ the momentum dependent width

$$\Gamma_\rho(M_{\pi\pi}) = \Gamma_0 \left(\frac{q}{q_0} \right)^3 \frac{M_\rho}{M_{\pi\pi}} \quad (6.5)$$

where Γ_0 is the width of the ρ^0 , q is the π momentum in the $\pi\pi$ rest frame and q_0 is the value of q for $M_{\pi\pi} = M_\rho$. The $M_{\pi\pi}$ -independent non-resonant amplitude is denoted by B , and A is the normalization factor of the resonant amplitude. Additionally, another term f was introduced which should reflect the background from reactions with diffractive photon dissociation. The term f was assumed to be of the form[44]

$$f = A_f(1 + 1.5M_{\pi\pi}) \quad (6.6)$$

Alternatively the following parameterization proposed by Ross and Stodolsky [48] was used

$$\frac{d\sigma}{dM_{\pi\pi}} = A \left[\frac{M_{\pi\pi} M_\rho \Gamma_\rho}{(M_{\pi\pi}^2 - M_\rho^2)^2 + M_\rho^2 \Gamma_\rho^2} \left(\frac{M_\rho}{M_{\pi\pi}} \right)^n + f \right] \quad (6.7)$$

where Γ_ρ is given by Eq. (6.5) and f is given by Eq. (6.6).

Tab. (6.1) summarizes the results of the Söding type fit to the elastic and proton-dissociative $M_{\pi\pi}$ spectra in three and four t ranges, respectively. The results of the fit with Ross-Stodolsky parameterization are presented in Tab. (6.2). The χ^2/NDF for all the fits is satisfactory. The values of M_ρ , Γ_0 and χ^2/NDF do not depend on the prescription used to parameterize the mass distribution. The ρ^0 mass M_ρ and width Γ_0 are within the statistical error close to the PDG values (768.1 ± 1.3 and 150.9 ± 3.0 MeV respectively)

Therefore to decrease the uncertainties of the fitted parameters, the final results for B/A , n and A_f were obtained by repeating the fits with the ρ^0 mass and width fixed to that of PDG. Tab. (6.3) summarizes the results of these fits. The mass distributions for elastic and proton-dissociative $\pi^+\pi^-$ production are shown in Fig. (6.2) together with the results of fits according to Eq. (6.4). The contribution from events with photon dissociation (term f in Eq. (6.4) and in Eq. (6.7)) in the mass range $0.55 < M_{\pi\pi} < 1.2$ GeV increases systematically from about $2 \pm 2\%$ at low $-t$ to about $11 \pm 11\%$ at large $-t$. Within the statistical errors this background contribution is the same for elastic and proton-dissociative $\pi^+\pi^-$ production. Fig. (6.2) shows also the ratio B/A and n as a function of $-t$. Both quantities decrease with $-t$, since the skewing decreases as the momentum transfer increases.

Söding

$-t(\text{GeV}^2)$	process	$A^2(\mu\text{b})$	M_ρ (MeV)	$\Gamma_0(\text{MeV})$	$B/A(\text{GeV}^{-1/2})$	$A_f(\text{GeV}^{-1})$	χ^2/NDF
0.30 - 0.45	$\gamma p \rightarrow \rho p$	0.50 ± 0.05	773 ± 12	143 ± 13	0.51 ± 0.15	0.05 ± 0.04	1.1
0.45 - 0.80	$\gamma p \rightarrow \rho p$	0.24 ± 0.03	775 ± 10	143 ± 15	0.50 ± 0.17	0.16 ± 0.06	0.5
0.80 - 1.40	$\gamma p \rightarrow \rho p$	0.04 ± 0.01	744 ± 25	154 ± 30	0.00 ± 0.52	0.00 ± 0.33	1.1
0.30 - 0.45	$\gamma p \rightarrow \rho N$	0.80 ± 0.08	767 ± 11	132 ± 15	0.40 ± 0.14	0.01 ± 0.05	1.6
0.45 - 0.80	$\gamma p \rightarrow \rho N$	0.72 ± 0.09	777 ± 11	172 ± 25	0.47 ± 0.17	0.03 ± 0.06	0.7
0.80 - 1.40	$\gamma p \rightarrow \rho N$	0.42 ± 0.07	777 ± 14	140 ± 17	0.40 ± 0.19	0.15 ± 0.11	1.2
1.40 - 3.00	$\gamma p \rightarrow \rho N$	0.20 ± 0.02	781 ± 26	184 ± 40	0.15 ± 0.17	0.00 ± 0.41	1.4

Table 6.1: Results of the fits with Söding parameterization (see Eq. (6.4)) for elastic and proton-dissociative $\pi^+\pi^-$ photoproduction. The fits were performed in the mass range $0.55 < M_{\pi\pi} < 1.2$ GeV. Only the statistical errors are presented.

Ross Stodolsky

$-t(\text{GeV}^2)$	process	$A(\mu\text{b})$	M_ρ (MeV)	$\Gamma_0(\text{MeV})$	n	$A_f(\text{GeV}^{-1})$	χ^2/NDF
0.30 - 0.45	$\gamma p \rightarrow \rho p$	0.52 ± 0.05	771 ± 11	142 ± 13	3.8 ± 0.9	0.04 ± 0.03	1.1
0.45 - 0.80	$\gamma p \rightarrow \rho p$	0.22 ± 0.03	775 ± 10	140 ± 19	4.1 ± 1.2	0.15 ± 0.06	0.6
0.80 - 1.40	$\gamma p \rightarrow \rho p$	0.04 ± 0.01	745 ± 20	152 ± 30	0.0 ± 4.0	0.00 ± 0.33	1.1
0.30 - 0.45	$\gamma p \rightarrow \rho N$	0.81 ± 0.08	765 ± 10	131 ± 14	3.4 ± 0.5	0.00 ± 0.25	1.6
0.45 - 0.80	$\gamma p \rightarrow \rho N$	0.76 ± 0.08	778 ± 11	174 ± 25	3.4 ± 1.1	0.03 ± 0.05	0.8
0.80 - 1.40	$\gamma p \rightarrow \rho N$	0.43 ± 0.06	777 ± 13	140 ± 19	3.1 ± 1.3	0.14 ± 0.10	1.2
1.40 - 3.00	$\gamma p \rightarrow \rho N$	0.21 ± 0.03	782 ± 26	196 ± 40	1.1 ± 1.2	0.00 ± 0.50	1.4

Table 6.2: Results of the fits according to the Ross-Stodolsky parameterization (see Eq. (6.7)) for elastic and proton-dissociative $\pi^+\pi^-$ photoproduction. The fits were performed in the mass range $0.55 < M_{\pi\pi} < 1.2$ GeV. Only the statistical errors are presented.

Within the errors both B/A and n are the same for elastic and proton-dissociative $\pi^+\pi^-$ production. These indicate that the data are consistent with the hypothesis of factorization.

The systematic uncertainty on B/A is dominated by the sensitivity of the results to the vertex selection cuts (± 0.03 GeV $^{-1/2}$), tracking cuts (± 0.02 GeV $^{-1/2}$) and variation of the parameters E_{max} and R_{max} (± 0.02 GeV $^{-1/2}$). The effect of these checks on n measurement is relatively the same like on B/A . No changes of the systematic errors with t was found. The effect of the systematic checks within the error is the same for elastic and proton-dissociative samples.

Söding $M_\rho = 768 \text{ MeV}$, $\Gamma_0 = 151 \text{ MeV}$					
$-t(\text{GeV}^2)$	process	$A^2(\mu\text{b})$	$B/A(\text{GeV}^{-1/2})$	$A_f(\text{GeV}^{-1})$	χ^2/NDF
0.30 - 0.45	$\gamma p \rightarrow \rho p$	0.52 ± 0.04	0.45 ± 0.07	0.03 ± 0.03	0.9
0.45 - 0.80	$\gamma p \rightarrow \rho p$	0.24 ± 0.02	0.39 ± 0.08	0.09 ± 0.05	0.8
0.80 - 1.40	$\gamma p \rightarrow \rho p$	0.03 ± 0.01	0.21 ± 0.15	0.11 ± 0.12	1.3
0.30 - 0.45	$\gamma p \rightarrow \rho N$	0.80 ± 0.06	0.45 ± 0.07	0.00 ± 0.02	1.8
0.45 - 0.80	$\gamma p \rightarrow \rho N$	0.73 ± 0.05	0.37 ± 0.08	0.04 ± 0.04	0.8
0.80 - 1.40	$\gamma p \rightarrow \rho N$	0.45 ± 0.04	0.28 ± 0.08	0.08 ± 0.07	1.0
1.40 - 3.00	$\gamma p \rightarrow \rho N$	0.17 ± 0.03	0.06 ± 0.10	0.12 ± 0.12	1.2

Ross Stodolsky $M_\rho = 768 \text{ MeV}$, $\Gamma_0 = 151 \text{ MeV}$					
$-t(\text{GeV}^2)$	process	$A(\mu\text{b})$	n	$A_f(\text{GeV}^{-1})$	χ^2/NDF
0.30 - 0.45	$\gamma p \rightarrow \rho p$	0.54 ± 0.04	3.4 ± 0.5	0.02 ± 0.03	0.9
0.45 - 0.80	$\gamma p \rightarrow \rho p$	0.25 ± 0.02	3.0 ± 0.6	0.09 ± 0.05	0.8
0.80 - 1.40	$\gamma p \rightarrow \rho p$	0.03 ± 0.01	1.7 ± 1.2	0.12 ± 0.12	1.3
0.30 - 0.45	$\gamma p \rightarrow \rho N$	0.82 ± 0.06	3.4 ± 0.5	0.00 ± 0.02	1.8
0.45 - 0.80	$\gamma p \rightarrow \rho N$	0.75 ± 0.05	2.9 ± 0.6	0.04 ± 0.04	0.8
0.80 - 1.40	$\gamma p \rightarrow \rho N$	0.52 ± 0.04	2.2 ± 0.6	0.09 ± 0.07	1.0
1.40 - 3.00	$\gamma p \rightarrow \rho N$	0.17 ± 0.03	0.5 ± 0.8	0.13 ± 0.12	1.3

Table 6.3: Results of the fits for the two parameterizations (Söding Eq. (6.4) and Ross-Stodolsky Eq. (6.7)) for the elastic and proton-dissociative ρ^0 photoproduction. The fits were performed in the mass range $0.55 < M_{\pi\pi} < 1.2 \text{ GeV}$. The values of M_ρ and Γ_0 were fixed to that of PDG.

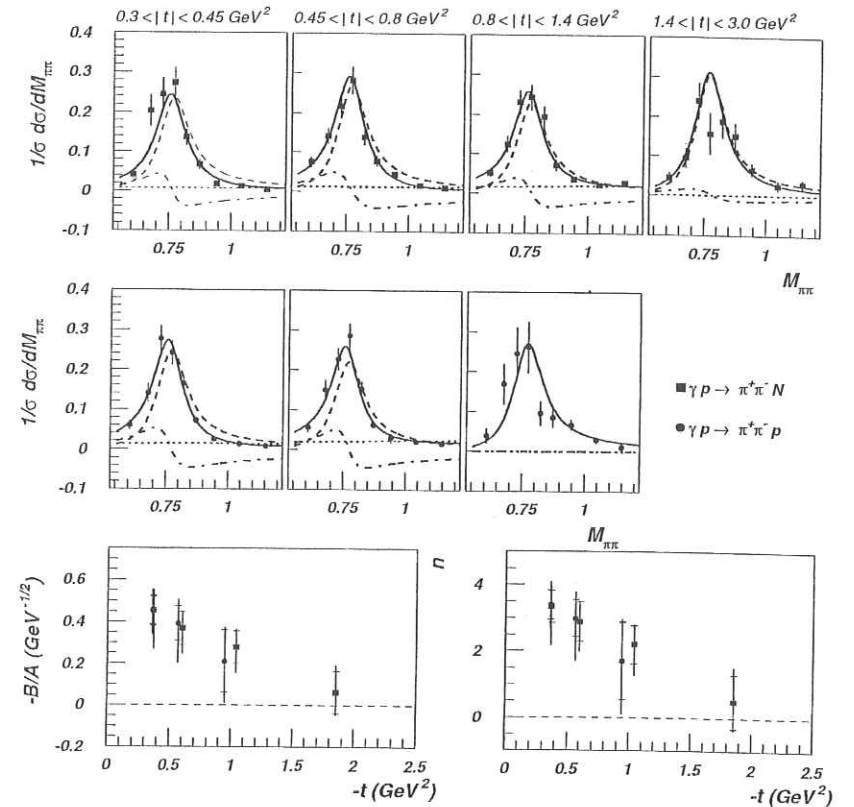


Figure 6.2: The normalized differential cross section $1/\sigma \cdot d\sigma/dM_{\pi\pi}$ for proton-dissociative (squares) and elastic (circles) $\pi\pi$ photoproduction in different t bins. The dashed curve represents the fitted resonant contribution, the dotted curve the non-resonant contribution and the dot-dashed curve the contribution from the interference term. The continuous curve is the sum. Only the statistical errors are presented. The ratio B/A and the parameter n as a function of $-t$ for the elastic (circles) and proton-dissociative (squares) processes. The inner error bars indicate the statistical uncertainty and the outer ones the statistical and systematical uncertainties summed in quadrature.

6.3.2 Differential cross section $d\sigma/dt$

The differential cross section $d\sigma/dt$ for elastic and proton-dissociative ρ^0 photoproduction was calculated according to Eq. (6.1) and Eq. (6.2). The proton-dissociative contribution, C_D , was determined as described in Sec. (6.2).

Since $d\sigma/dt$ was studied in tighter t bins than used in the ρ^0 mass analysis, the resonant contribution, C_{res} , was calculated analytically in each t bin

$$C_{res}(t) = \frac{\sigma(\gamma p \rightarrow \rho^0 X) / \int_{0.55}^{1.2} d\sigma(\gamma p \rightarrow \pi\pi X) dM_{\pi\pi}}{\int_{2M_\pi}^{M_\rho + 5\Gamma_0} BW^2(M_{\pi\pi}) dM_{\pi\pi} / \int_{0.55}^{1.2} [|BW(M_{\pi\pi}) + B/A|^2 + A_f(1 + 1.5M_{\pi\pi})] dM_{\pi\pi}} \quad (6.8)$$

where the parameters B/A and A_f were calculated according to the parameterizations used in the reweighting procedure (see Eq. (5.8) and Eq. (5.9)).

Fig. (6.3) shows C_{res} used to correct $d\sigma/dt$ as calculated from Eq. (6.9).

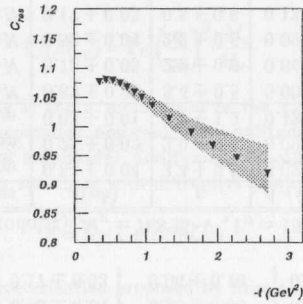


Figure 6.3: The C_{res} used to obtain the differential cross section $d\sigma/dt$ for elastic and proton-dissociative ρ^0 photoproduction. The shaded band corresponds to the total uncertainty of the C_{res} .

Fig. (6.4a) shows the differential cross section $d\sigma/dt$ for elastic and proton-dissociative (for $M_N^2 < 0.1W^2$) ρ^0 photoproduction. Both samples exhibit an exponential drop with increasing $-t$, with the cross section for the elastic process falling off more steeply than that for the proton-dissociative process. The results of fits with the single exponential function, $d\sigma/dt = A \cdot \exp(bt)$, in the t range $0.4 < -t < 1.2$ GeV² are shown in Tab. (6.4).

The ratio of the elastic to the proton-dissociative cross sections is also an interesting quantity. Because in each t bin the errors (also statistical) on $d\sigma/dt$ (see Eq. (6.1) and Eq. (6.2)) are strongly correlated, same errors on both distributions cancel in the ratio. Therefore the ratio was recalculated with a correct treatment of the statistical correlations. In Fig. (6.4b) the ratio of the elastic to the proton-dissociative cross section is shown as a function of $-t$. Since the average t in each t bin is different for elastic (t_{el}) and proton-dissociative (t_{pd}) events both cross sections were corrected so as to be given at the same t value of $t' = (t_{el} + t_{pd})/2$ according to the following formula

$$\frac{d\sigma_{el}/dt}{d\sigma_{pd}/dt} = \frac{d\sigma_{el}(t = t_{el}) \cdot \exp(b_{el}(t' - t_{el}))}{d\sigma_{pd}(t = t_{pd}) \cdot \exp(b_{pd}(t' - t_{pd}))} \quad (6.10)$$

where the subscripts on b refer to the elastic (el) and proton-dissociative (pd) samples and t -slopes were obtained from the fits with function $\sim \exp(bt)$ separately for elastic and proton-dissociative samples.

This ratio falls off rapidly with $-t$ from about $7 \cdot 10^{-1}$ at $-t \approx 0.4$ GeV² to $\approx 10^{-2}$ for $-t \geq 1$ GeV². Tab. (6.4) shows also the results of the fit with the single exponential function, $A \cdot \exp(bt)$, to the ratio of cross sections in the t range $0.4 < -t < 1.2$ GeV². Due to the correlated errors the values of A and b found from the fit to the ratio are not simply the ratio A_{el}/A_{pd} and difference $b_{el} - b_{pd}$ found from the fits to the cross sections.

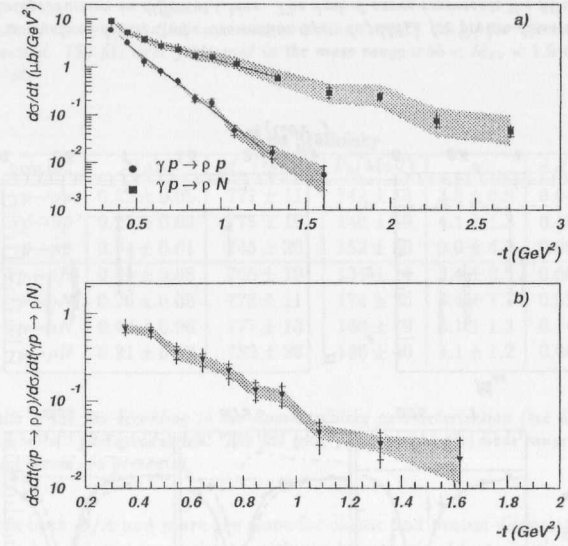


Figure 6.4: The differential cross sections $d\sigma/dt$ (a) for the processes $\gamma p \rightarrow \rho p$ (circles) and $\gamma p \rightarrow \rho N$ (squares) in the kinematic range $2M_\pi < M_{\pi\pi} < M_\rho + 5\Gamma_0$, $85 < W < 105$ GeV and $M_N^2 < 0.1 \cdot W^2$. The continuous lines represent the results of the exponential fit of the form $A \cdot e^{bt}$. The ratio of the cross sections $d\sigma/dt(\gamma p \rightarrow \rho p)/d\sigma/dt(\gamma p \rightarrow \rho N)$ (b) as a function of $-t$. The inner error bars on both plots indicate the statistical uncertainty and the outer ones the statistical and systematical uncertainties summed in quadrature. The shaded region corresponds to the uncertainty in modeling proton dissociation.

The systematic uncertainty is dominated by the uncertainty in the parameterization of the M_N evolution with t in the proton-dissociative MC, using FCAL instead of the PRT1 for tagging proton dissociation and sensitivity of the results to the position of the collimator in front of the FCAL. The overall normalization error for cross sections measurement is also significant. The effect of these systematic checks on the cross sections and on the ratio of cross sections are listed in Tab. (6.5) for different t values. The systematic errors due to the checks: 1,2,3,4,8,11,12 and 15 are of the order 3-5 %, other systematic errors are below 3 %. The variation of the t -slope at low $-t$ for elastic process from 11 GeV⁻² by ± 1 GeV⁻² changes the elastic cross section by ± 5 % only in the first t bin. The variation of the background contribution within its uncertainty (check 18) changes the cross sections at large $-t$ by ± 5 %.

process	A	$b \text{ GeV}^{-2}$
$\gamma p \rightarrow \rho p$	$51 \pm 7 \pm 11 \pm 10 (\mu\text{bGeV}^{-2})$	$6.0 \pm 0.3 \pm 0.3 \pm 0.4$
$\gamma p \rightarrow \rho N$	$14 \pm 1 \pm 3 \pm 1 (\mu\text{bGeV}^{-2})$	$2.4 \pm 0.2 \pm 0.2 \pm 0.3$
$\gamma p \rightarrow \rho p / \gamma p \rightarrow \rho N$	$3.1 \pm 0.5 \pm 0.5 \pm 0.7$	$3.4 \pm 0.3 \pm 0.3 \pm 0.2$

Table 6.4: The results of the exponential fit of the form $A \cdot e^{bt}$ to the differential cross section $d\sigma/dt$ for the processes $\gamma p \rightarrow \rho p$ and $\gamma p \rightarrow \rho N$ and to the ratio of cross sections. The first error is the statistical one the second error is the systematical one and the last error is the error in modeling proton dissociation.

systematic check	$\frac{d\sigma_{pd}}{dt}$			$\frac{d\sigma_{st}}{dt}$		$\frac{d\sigma_{st}}{dt} / \frac{d\sigma_{pd}}{dt}$	
	$-t \approx 0.5$	$-t \approx 1.0$	$-t \approx 2.0$	$-t \approx 0.5$	$-t \approx 1.0$	$-t \approx 0.5$	$-t \approx 1.0$
10	10 %	30 %	70 %	4 %	10 %	6 %	20 %
9	-10 %	-5 %	10 %	10 %	20 %	20 %	25 %
38	15 %	15 %	15 %	5 %	5 %	10 %	10 %
39	16 %	16 %	16 %	16 %	16 %	0 %	0 %

Table 6.5: Main systematic uncertainties on the ρ^0 cross sections and the ratio of cross section at different value of t .

6.3.3 Decay angular distribution

The differential cross section $d\sigma/d \cos \theta_h$ and $d\sigma/d\phi_h$ for elastic and proton-dissociative ρ^0 photoproduction was calculated according to Eq. (6.1) and Eq. (6.2). The proton-dissociative contribution, C_D was determined as described in Sec. (6.2) as a function of relevant angles. It was assumed that the resonant contribution C_{res} does not depend on $\cos \theta_h$ and ϕ_h .

In Fig. (6.5) the acceptance corrected $\cos \theta_h$ and ϕ_h distributions for elastic sample are shown together with the results of the fits according to Eq. (2.19) and Eq. (2.20) in three t ranges. Also the spin density matrix elements r_{00}^{04} and r_{1-1}^{04} obtained from these fits are shown as a function of $-t$. The same distributions for proton-dissociative sample are presented in Fig. (6.6) in four t ranges.

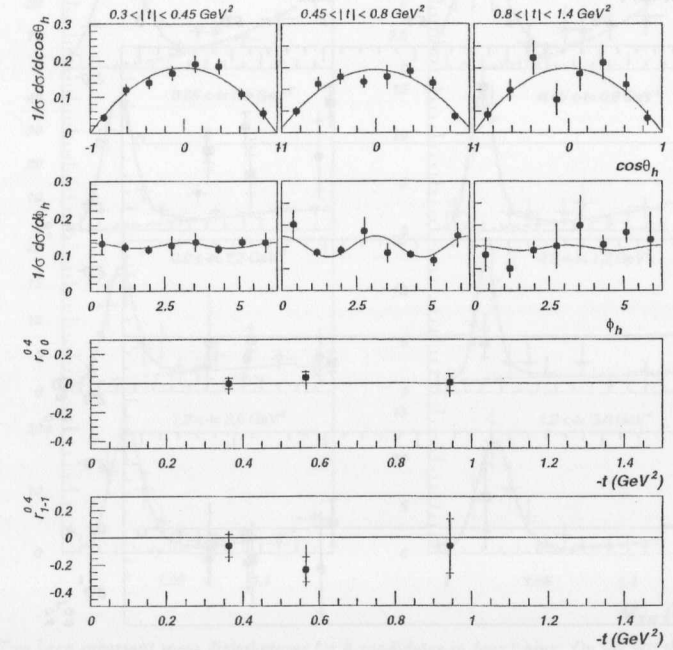


Figure 6.5: Differential distribution $1/\sigma d\sigma/d\cos\theta_h$ and $1/\sigma d\sigma/d\phi_h$ for elastic ρ^0 photoproduction in three t bins. The continuous lines represent the results of the fits according to Eq. (2.19) and Eq. (2.20). The spin density matrix elements as a function of $-t$ obtained by fitting Eq. (2.19) and Eq. (2.20) to the data. The inner error bars indicate the statistical error, the outer ones the statistical and systematical error added in quadrature.

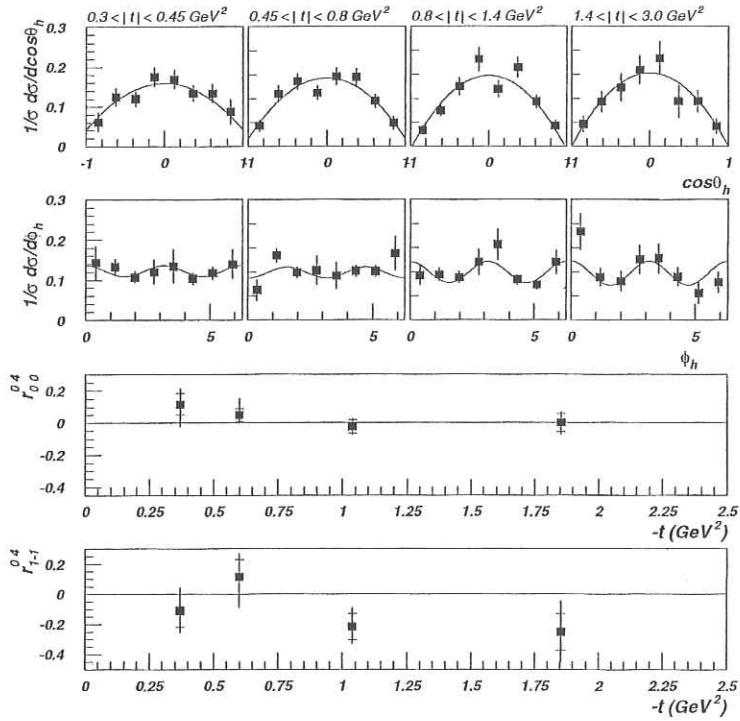


Figure 6.6: Differential distribution $1/\sigma d^2\sigma/d\cos\theta_h$ and $1/\sigma d^2\sigma/d\phi_h$ for proton dissociative ρ^0 photoproduction in four t bins. The continuous lines represent the results of the fits according to Eq. (2.19) and Eq. (2.20). The spin density matrix elements as a function of $-t$ obtained by fitting Eq. (2.19) and Eq. (2.20) to the data. The inner error bars indicate the statistical error, the outer ones the statistical and systematical error added in quadrature.

In Fig. (6.7) the matrix elements obtained by fitting Eq. (2.18) to the two-dimensional distribution are shown as a function of $-t$. The fits to the two and one dimensional distributions give consistent results. Two dimensional fit allows determination also r_{10}^{04} matrix element. The data do not indicate a dependence on t of all matrix elements except for r_{1-1}^{04} which decreases as $-t$ increases. At the highest $-t$ bins r_{1-1}^{04} was found to be different from zero.

The present accuracy does not allow to conclude about SCHC violation at t range covered at this analysis. In addition, the non-zero value of r_{1-1}^{04} could be due to the possible significant contribution ($10 \pm 10\%$) of the photon-dissociative events in the sample as found from the fit to the $M_{\pi\pi}$ distributions integrated over helicity angles or strong variation of the interference and nonresonant contributions with the helicity angles. Present statistics does not allow to perform the $M_{\pi\pi}$ analysis in bins of the helicity angles to extract directly the resonance contribution as a function of the helicity angles.

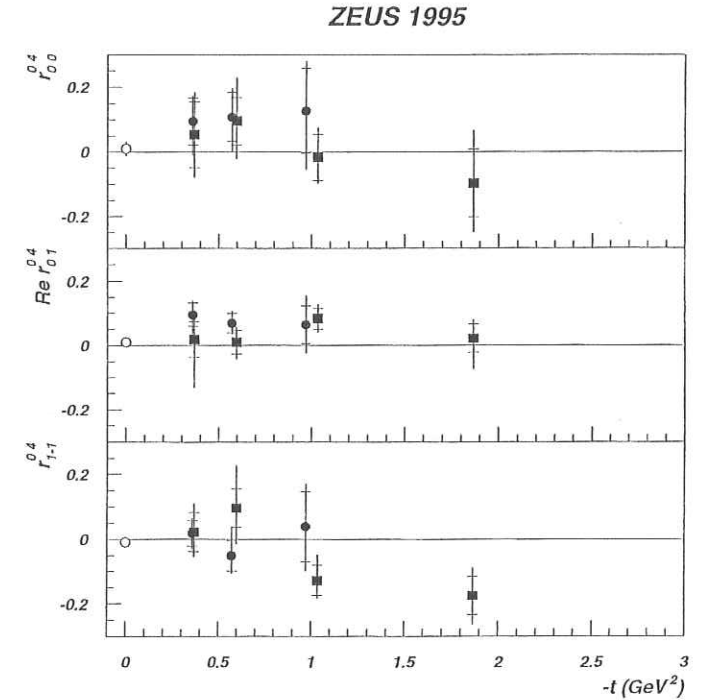


Figure 6.7: The spin density matrix elements as a function of $-t$ obtained by two dimensional fitting of the Eq. (2.18) to the data. The inner error bars indicate the statistical error, the outer ones the statistical and systematical error added in quadrature. The circles correspond to the elastic ρ^0 production and squares correspond to the proton-dissociative production.

6.4 ϕ photoproduction

6.4.1 Mass distribution

Since the acceptance as a function of M_{KK} is flat in the region of the ϕ resonance, the non-resonant background under the ϕ signal was determined by fitting the observed mass spectra in data without mass dependent corrections. Due to the limited statistics of the sample the ϕ invariant mass analysis was performed in four t bins. A relativistic Breit-Wigner (BW) function smeared with a Gaussian function for the finite tracking resolution is fitted to the data over a function describing the background (BG).

The background is mainly due to diffractive ρ^0 production. The shape of this background as a function of M_{KK} was deduced by studying the invariant mass distributions of the ρ^0 MC events for which the two pions are given the kaon mass

$$BG = A_{BG} \cdot (M_{KK} - 2M_K)^\Delta \quad (6.11)$$

where Δ is a parameter determined by the fit.

Fig. (6.8) shows the two kaon invariant mass spectra separately for all selected events and for events with an additional tag in the PRT. In each of the plots the fitted power like function describing the background is shown as a dashed line. The results of the fits are summarized in Tab. (6.6). In the fits the width of the BW function was fixed at 4.4 MeV.

all selected events					
$-t$ (GeV ²)	M_ϕ (MeV)	resolution (MeV)	backg. (%)	Δ	χ^2/NDF
0.40 - 0.65	1020 ± 1	12 ± 1	9 ± 2	2.2 ± 0.2	1.0
0.65 - 0.90	1021 ± 1	8 ± 1	8 ± 2	1.8 ± 0.4	1.2
0.90 - 1.20	1021 ± 2	7 ± 1	15 ± 8	0.9 ± 0.5	0.8
1.20 - 3.00	1023 ± 3	8 ± 1	2 ± 1	2.5 ± 0.5	1.2

PRT1 tagged events					
$-t$ (GeV ²)	M_ϕ (MeV)	resolution (MeV)	backg. (%)	Δ	χ^2/NDF
0.40 - 0.65	1017 ± 3	13 ± 1	7 ± 3	2.5 ± 0.6	0.9
0.65 - 0.90	1019 ± 2	6 ± 2	7 ± 2	1.8 ± 0.2	0.5
0.90 - 1.20	1021 ± 2	7 ± 1	10 ± 5	1.5 ± 0.5	0.9
1.20 - 3.00	1024 ± 3	7 ± 2	1 ± 2	2.8 ± 0.6	0.6

Table 6.6: Summary of results for the fits to the M_{KK} spectra shown in Fig. (6.8). The background column indicates the fitted fraction of the background events in the region $0.99 < M_{KK} < 1.06$ GeV. In each case the fit range is $0.99 < M_{KK} < 1.15$ GeV.

The values obtained for the mass of ϕ are in agreement with the Particle Data Group and the observed tracking resolution is also in good agreement with that obtained using the MC (10, 8, 6, 6 MeV for four chosen t bins respectively). The fraction of the background events was found within the statistical error to be the same for all selected events and for those with the additional hit in the PRT. This indicates that the non-resonant background is the same for elastic and for proton dissociative ϕ events.

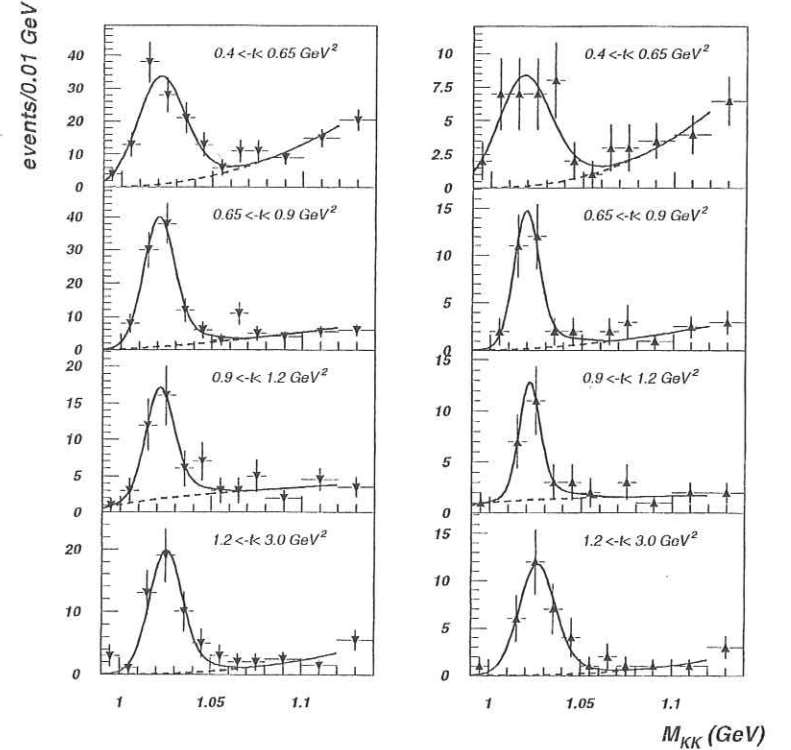


Figure 6.8: Two kaon invariant mass distributions for ϕ candidates in four t bins. On the left the mass spectra for all selected events are shown. On the right the mass spectra for events with a tag in the PRT are presented. The continuous line is the result of fit to the sum of the Breit-Wigner function convoluted with Gaussian function and the power like background term of the form $A \cdot (M_{KK} - 2M_K)^\Delta$. The fitted background is indicated by the dashed line.

6.4.2 Differential cross section $d\sigma/dt$

The differential cross section $d\sigma/dt$ for elastic and proton-dissociative ϕ photoproduction was calculated according to Eq. (6.1) and Eq. (6.2). The proton-dissociative contribution, C_D , was determined as described in Sec. (6.2).

The resonant contribution, C_{res} , in the ϕ signal region was parameterized as a function of t according to the Eq. (5.14)

$$C_{res} = 1 - k_{bg} \cdot e^{b_{bg}t} \quad (6.12)$$

Fig. (6.9a) shows the differential cross section $d\sigma/dt$ for elastic and proton-dissociative (for $M_N^2 < 0.1W^2$) ϕ photoproduction. As in the ρ^0 case, both differential cross sections decrease exponentially with increasing $-t$. The results of fits with the single exponential function, $d\sigma/dt = A \cdot \exp(bt)$, in the t range $0.4 < -t < 1.2 \text{ GeV}^2$ are shown in Tab. (6.7).

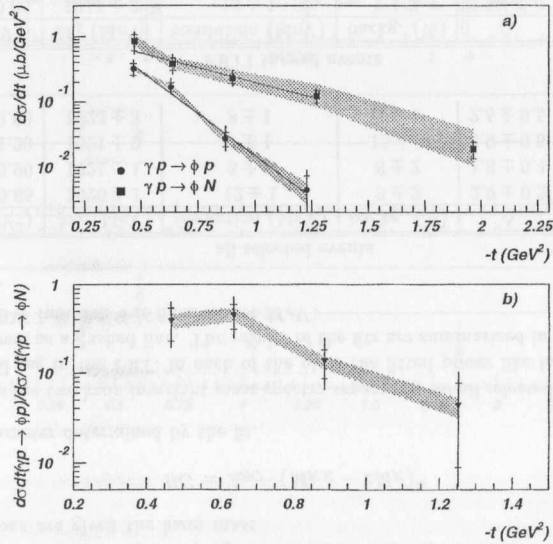


Figure 6.9: The differential cross sections $d\sigma/dt$ (a) for the processes $\gamma p \rightarrow \phi p$ (circles) and $\gamma p \rightarrow \phi N$ (squares) in the kinematic range $85 < W < 105 \text{ GeV}$ and $M_N^2 < 0.1 \cdot W^2$. The continuous lines represent the results of the exponential fit of the form $A \cdot e^{bt}$. The ratio of the cross sections $d\sigma/dt(\gamma p \rightarrow \phi p) / d\sigma/dt(\gamma p \rightarrow \phi N)$ (b) as a function of $-t$. The inner error bars on both plots indicate the statistical uncertainty and the outer ones the statistical and systematical uncertainties summed in quadrature. The shaded region corresponds to the uncertainty in modeling proton dissociation.

The main systematic uncertainties on the ϕ cross sections and ratio of cross section are similar as those discussed in ρ^0 production case.

process	A	b GeV ⁻²
$\gamma p \rightarrow \phi p$	$6.8 \pm 2.0 \pm 2.9 \pm 0.9$ (μbGeV^{-2})	$6.3 \pm 0.7 \pm 0.7 \pm 0.3$
$\gamma p \rightarrow \phi N$	$1.6 \pm 0.4 \pm 0.6 \pm 0.2$ (μbGeV^{-2})	$2.1 \pm 0.5 \pm 0.3 \pm 0.4$
$\gamma p \rightarrow \phi p / \gamma p \rightarrow \phi N$	$1.7 \pm 0.7 \pm 0.9 \pm 0.7$	$3.0 \pm 0.8 \pm 0.8 \pm 0.4$

Table 6.7: The results of the exponential fit of the form $A \cdot e^{bt}$ to the differential cross section $d\sigma/dt$ for the processes $\gamma p \rightarrow \phi p$ and $\gamma p \rightarrow \phi N$ and to the ratio of cross sections. The first error is the statistical one the second error is the systematical one and the last error is the error in modeling proton dissociation.

6.4.3 Decay angular distribution

Present statistic does not allow to study helicity angle distributions after separation of the elastic and proton-dissociative samples. The helicity analysis was performed using all diffractive ϕ candidates assuming that the factorization holds and the decay angular distributions are the same for elastic and proton-dissociative events.

Before acceptance correction the background contribution was subtracted from the data. It was assumed that the helicity angle distributions of the background events in the ϕ signal region ($0.99 < M_{KK} < 1.06 \text{ GeV}$) are the same as outside this region ($1.06 < M_{KK} < 1.15 \text{ GeV}$).

In each t range considered in this study the normalized $\cos\theta_h$ and ϕ_h distributions obtained for events lying outside the ϕ signal region were subtracted from the distributions obtained for events lying inside the ϕ signal region. The amount of subtracted events was chosen according to the results of the M_{KK} spectra analysis described in one of the previous sections.

In Fig. (6.10) the background subtracted and acceptance corrected $\cos\theta_h$ and ϕ_h distributions are shown together with the fits according to Eq. (2.19) and Eq. (2.20) in four t bins. On the plot also the spin density matrix elements r_{00}^{04} and r_{1-1}^{04} obtained from these fits are shown as a function of $-t$. Similarly as in the case of ρ^0 , at the highest $-t$ bins r_{1-1}^{04} was found to be different from zero. Present statistics does not allow to perform the M_{KK} analysis in bins of the helicity angles to directly extract the ϕ contribution as a function of the helicity angles.

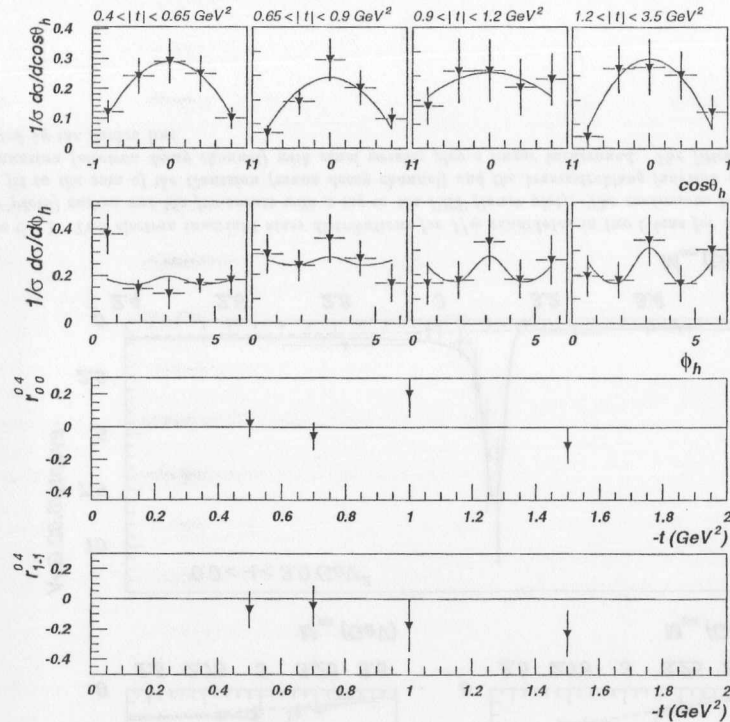


Figure 6.10: Differential distribution $1/\sigma d^2\sigma/d\cos\theta_h$ and $1/\sigma d^2\sigma/d\phi_h$ for diffractive ϕ photoproduction in four t bins. The continuous lines represent the results of the fits according to Eq. (2.19) and Eq. (2.20). The spin density matrix elements as a function of $-t$ obtained by fitting Eq. (2.19) and Eq. (2.20) to the data. Only statistical errors are shown.

6.5 J/ψ photoproduction

6.5.1 Mass distribution

Similarly as in the case of ϕ the non-resonant background under the J/ψ signal was determined by fitting the observed mass spectra in data without mass dependent corrections. Due to the limited statistics of the sample the J/ψ invariant mass analysis was performed in two t bins for all selected events and in one bin for PRT1 tagged events. A sum of the Gaussian (muon decay channel) and the bremsstrahlung function convoluted with the Gaussian (electron decay channel) with equal weights is fitted to the data over a linear background of the form

$$BG = A_{BG} \cdot (1 + \Delta M_{ee}). \quad (6.13)$$

Fig. (6.11) shows the two electron invariant mass spectra separately for all selected events and for events with the additional tag in the PRT1. In each of the plots the fitted non-resonant background is shown as a dashed line. The results of the fits are summarized in Tab. (6.8).

all selected events				
$-t$ (GeV^2)	$M_{J/\psi}$ (MeV)	resolution (MeV)	backg. (%)	χ^2/NDF
0.0 - 0.2	3083 ± 5	20 ± 5	19 ± 4	0.93
0.2 - 3.0	3092 ± 4	15 ± 3	20 ± 5	0.60
PRT tagged events				
$-t$ (GeV^2)	$M_{J/\psi}$ (MeV)	resolution (MeV)	backg. (%)	χ^2/NDF
0.0 - 3.0	3095 ± 6	11 ± 8	21 ± 10	0.43

Table 6.8: Summary of results for the fits shown in Fig. (6.11). The background column indicates the fitted fraction of the background events in the region $2.98 < M_{ee} < 3.13 \text{ GeV}$. In each case the fit range is $2.6 < M_{KK} < 3.4 \text{ GeV}$.

The values obtained for the mass of the J/ψ are in agreement with the Particle Data Group and the observed tracking resolution is also in good agreement with that obtained using the MC. The fraction of the background events was found within the statistical error to be the same for all selected events and for those with a hit in the PRT, also no t dependence was observed. This indicates that the non-resonant background is on the same level for elastic and for proton dissociative J/ψ events independently of the chosen t range.

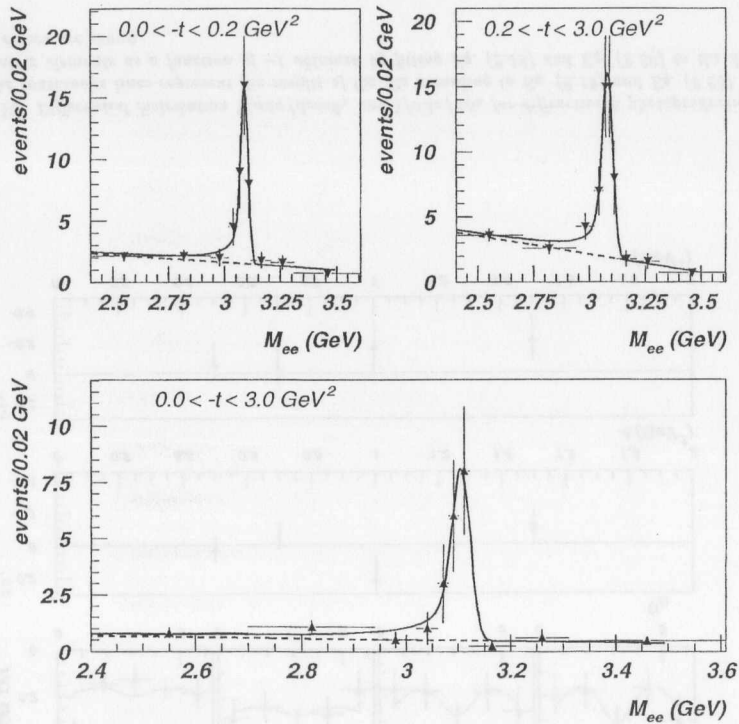


Figure 6.11: Two electron invariant mass distributions for J/ψ candidates in two t bins for all selected data (upper plots) and in one bin for events with a tag in the PRT (lower plot). The continuous line is the result of the fit to the sum of the Gaussian (muon decay channel) and the bremsstrahlung function convoluted with the Gaussian (electron decay channel) with equal weights plus a linear background. The fitted background is indicated by the dashed line.

6.5.2 Differential cross section $d\sigma/dt$

The differential cross section $d\sigma/dt$ for elastic and proton-dissociative J/ψ photoproduction was calculated according to Eq. (6.1) and Eq. (6.2). The proton-dissociative contribution, C_D , was determined as described in Sec. (6.2).

According to the results of the previous section the resonant contribution, C_{res} , in the J/ψ signal region is $80 \pm 5\%$. The same resonant contributions were assumed for elastic and for the proton dissociative.

Fig. (6.12a) shows the acceptance corrected t distributions for elastic and proton dissociative J/ψ events together with the results of an exponential fit of the form $A \cdot e^{bt}$ in the range $0.4 < -t < 1.2 \text{ GeV}^2$. In Fig. (6.12b) a ratio of the elastic to the proton dissociative cross section is shown as a function of $-t$. The results of fits with the single exponential function, $d\sigma/dt = A \cdot \exp(bt)$, in the range $0.4 < -t < 1.2 \text{ GeV}^2$ are shown in Tab. (6.9).

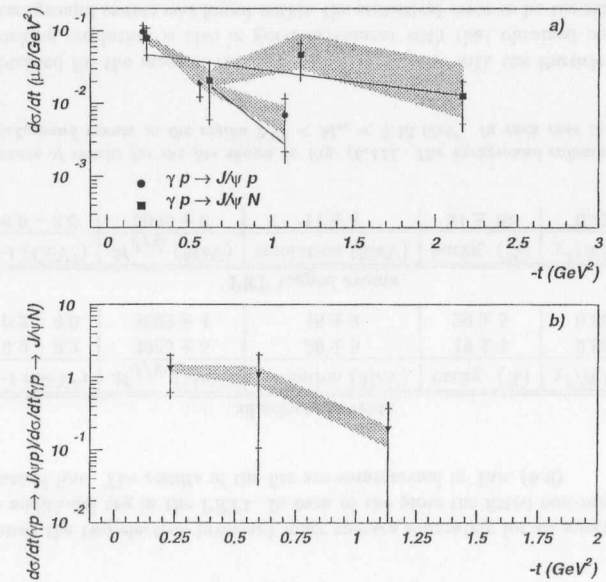


Figure 6.12: The differential cross sections $d\sigma/dt$ (a) for the processes $\gamma p \rightarrow J/\psi p$ (circles) and $\gamma p \rightarrow J/\psi N$ (squares) in the kinematic range $85 < W < 105 \text{ GeV}$ and $M_N^2 < 0.1 \cdot W^2$. The continuous lines represent the results of the exponential fit of the form $A \cdot e^{bt}$. The ratio of the cross sections $d\sigma/dt(\gamma p \rightarrow \phi p) / d\sigma/dt(\gamma p \rightarrow \phi N)$ (b) as a function of $-t$. The inner error bars on both plots indicate the statistical uncertainty and the outer ones the statistical and systematical uncertainties summed in quadrature. The shaded region corresponds to the uncertainty in modeling proton dissociation.

process	A	$b \text{ GeV}^{-2}$
$\gamma p \rightarrow J/\psi p$	$0.22 \pm 0.03 \pm 0.1 \pm 0.02 (\mu\text{b GeV}^{-2})$	$4.0 \pm 1.2 \pm 1.0 \pm 0.5$
$\gamma p \rightarrow J/\psi N$	$0.055 \pm 0.022 \pm 0.022 \pm 0.003 (\mu\text{b GeV}^{-2})$	$0.7 \pm 0.4 \pm 0.2 \pm 0.4$
$\gamma p \rightarrow J/\psi p / \gamma p \rightarrow J/\psi N$	$2.4 \pm 0.7 \pm 0.8 \pm 0.2$	$2.1 \pm 1.2 \pm 0.6 \pm 0.3$

Table 6.9: The results of the exponential fit of the form $A \cdot e^{bt}$ to the differential cross section $d\sigma/dt$ for the processes $\gamma p \rightarrow J/\psi p$ and $\gamma p \rightarrow J/\psi N$ and to the ratio of cross sections. The first error is the statistical one the second error is the systematical one and the last error is the model dependent error.

6.5.3 Decay angular distribution

The helicity analysis was performed for all diffractive J/ψ events in two t bins. The procedure used to subtract nonresonant contribution was the same as in the ϕ case. The events lying outside the J/ψ signal region ($2.40 < M_{ee} < 2.98 \text{ GeV}$) or ($3.13 < M_{ee} < 3.50 \text{ GeV}$) were used to subtract nonresonant contribution.

In Fig. (6.13) the background subtracted and acceptance corrected $\cos\theta_h$ and ϕ_h distributions are shown together with the fits according to Eq. (2.22) and Eq. (2.23) in two t bins. On the plot also the spin density matrix elements r_{00}^{04} and r_{1-1}^{04} obtained from these fits are shown as a function of $-t$. Similarly as in ρ^0 and ϕ case, r_{1-1}^{04} was found to be different from zero. Present statistics does not allow to perform the M_{ee} mass shape analysis in bins of the helicity angles to directly extract the J/ψ contribution as a function of the helicity angles.

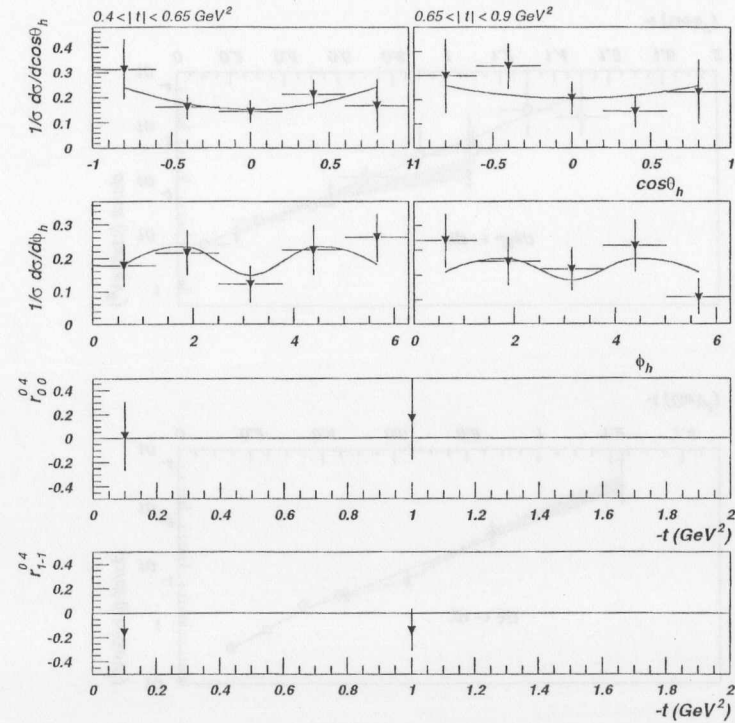


Figure 6.13: Differential distribution $1/\sigma d\sigma/d\cos\theta_h$ and $1/\sigma d\sigma/d\phi_h$ for diffractive J/ψ photoproduction in two t bins. The continuous lines represent the results of the fits according to Eq. (2.22) and Eq. (2.23). The spin density matrix elements as a function of $-t$ obtained by fitting Eq. (2.22) and Eq. (2.23) to the data. Only statistical errors are shown.

Chapter 7

Discussion

In this chapter the results of this analysis are compared to the previous ZEUS measurements. Then the predictions from the Regge and pQCD models are confronted with the data.

7.1 Comparison with the previous ZEUS measurements

Photoproduction of vector mesons at ZEUS was extensively studied in the low $-t$ region [45, 50, 46, 31]. It is interesting to test how these results extrapolate to the high $-t$ region covered by this analysis. In the following sections the t dependence of the cross sections as well as the mass shape and the spin density matrix elements as a function of t are discussed.

t dependence

In Fig. (7.1) the differential cross sections $d\sigma/dt$ for the elastic ρ^0 , ϕ and J/ψ photoproduction measured in this analysis and in the earlier ZEUS analyses are shown. The present data agree well with the low $-t$ results in the region of overlap, except for the ρ^0 case. The value of $d\sigma/dt$ at $-t \approx 0.3 \text{ GeV}^2$ of the LPS tagged ρ^0 analysis[50] (empty crosses) agrees within the error with both this measurement (full circles) and untagged photoproduction results[45] (empty circles). However this analysis differs from the untagged results by more than three standard deviations.

The data for ρ^0 cannot be described by a single exponential function, e^{bt} , over the whole t range. Also a quadratic function in exponent, e^{bt+ct^2} , does not describe the data. The best quality of the fit was obtained using single exponential function where the slope changes at $t \approx -0.25 \text{ GeV}^2$. The solid curve represents the result of the fit to the combined data. The t -slope was found to be $b = 10.2 \pm 0.2 \text{ GeV}^{-2}$ for $-t \leq 0.25 \text{ GeV}^2$ and $b = 6.0 \pm 0.2 \text{ GeV}^{-2}$ for $-t > 0.25 \text{ GeV}^2$.

Similarly as for ρ^0 the data for ϕ also cannot be described by single exponential function over the whole t range. In this case it was found that the slope changes at $t = -0.35 \text{ GeV}^2$. The solid curve represents the result of the combined fit. The t -slope for ϕ was found to be $b = 7.8 \pm 1.8 \text{ GeV}^{-2}$ for $-t \leq 0.35 \text{ GeV}^2$ and $b = 5.4 \pm 0.5 \text{ GeV}^{-2}$ for $-t > 0.35 \text{ GeV}^2$.

The data for J/ψ are well described by single exponential function where $b = 4.5 \pm 0.5 \text{ GeV}^{-2}$.

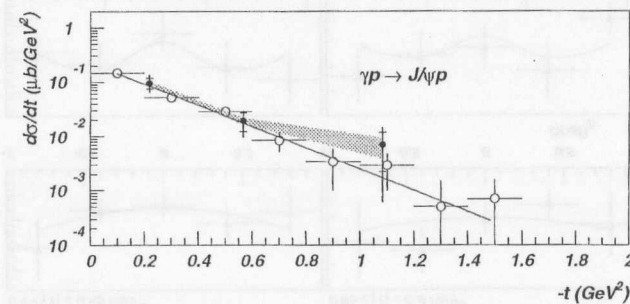
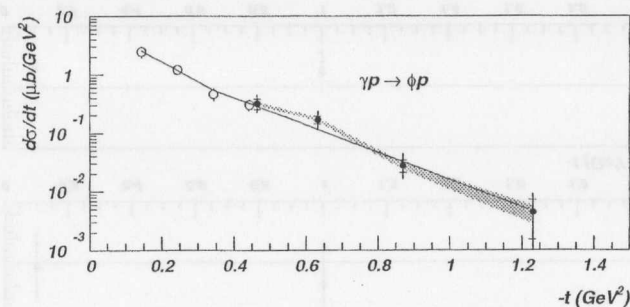
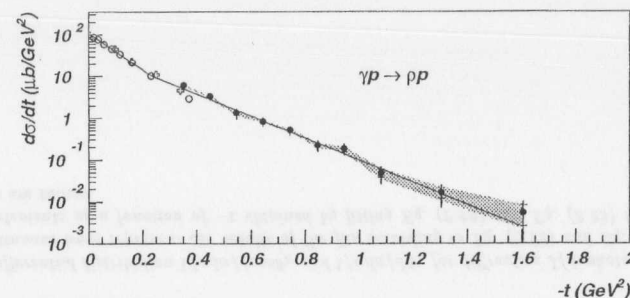


Figure 7.1: The differential cross sections $d\sigma/dt$ for elastic ρ^0 (upper plot) ϕ (middle plot) and J/ψ (bottom plot) photoproduction. The full circles correspond to this measurements, the empty symbols are from the earlier ZEUS analyses. The solid curves represent the result of the combined fit.

ρ^0 mass spectra

The fact that the results for ρ^0 mass shape analysis presented in Fig. (6.2) are the same within the errors for the elastic and proton-dissociative processes shows that factorization holds. This allows the study of the ρ^0 mass shape for the total diffractive sample with higher statistical accuracy. Fig. (7.2) shows the ratio B/A (Söding parameterization) and n (Ross-Stodolsky parameterization) as a function of $-t$ for diffractive ρ^0 events. The results of this analysis are compared with the low $-t$ results [44]. The data agrees in the region of overlap. The solid curves are the results of combined fit with single exponential function $k \cdot e^{b_k t}$. For B/A , $k = 0.80 \pm 0.05 \text{ GeV}^{-1/2}$ and $b_k = 1.75 \pm 0.15 \text{ GeV}^{-2}$ while for n we have $k = 6.1 \pm 0.4$ and $b_k = 1.76 \pm 0.15 \text{ GeV}^{-2}$.

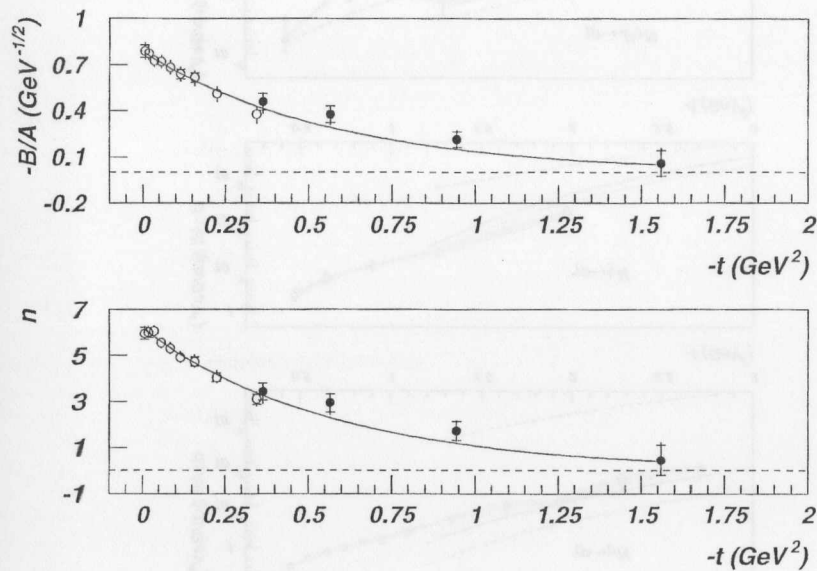


Figure 7.2: The ratio B/A and the parameter n as a function of $-t$ for the total diffractive sample. The empty circles correspond to ZEUS 1994 measurement [44].

Test of SCHC

The study of the ρ^0 decay angular distributions presented in Sec. (6.3.3) shows that the factorization hypothesis seems to hold. This allows to combine the elastic and proton-dissociative processes in order to reduce the statistical errors. Fig. (7.3) shows the compilation of the helicity analysis results obtained in this thesis and earlier ZEUS measurements. The results are presented in terms of the matrix elements r_{00}^{04} , r_{10}^{04} and r_{1-1}^{04} for ρ^0 , ϕ and J/ψ production as a function of $-t$.

The matrix elements are generally consistent with SCHC hypothesis except for the highest $-t$ range accessible in this analysis where r_{1-1}^{04} was found to be slightly different from zero for all the vector mesons and the parameter r_{10}^{04} , which was found to be also different from zero. However present accuracy does not allow to conclude about SCHC violation at t range covered at this analysis.

The reweighting procedure described in Sec. (5.2) requires the spin density matrix elements to be parameterized as a function of $-t$. It was assumed that r_{00}^{04} and r_{10}^{04} does not depend on t while r_{1-1}^{04} can be parameterize as $r_{1-1}^{04} = r_0 t$. Tab. (7.1) summarizes the values of r_{00}^{04} , r_{10}^{04} and r_0 resulting from the fits to the present data.

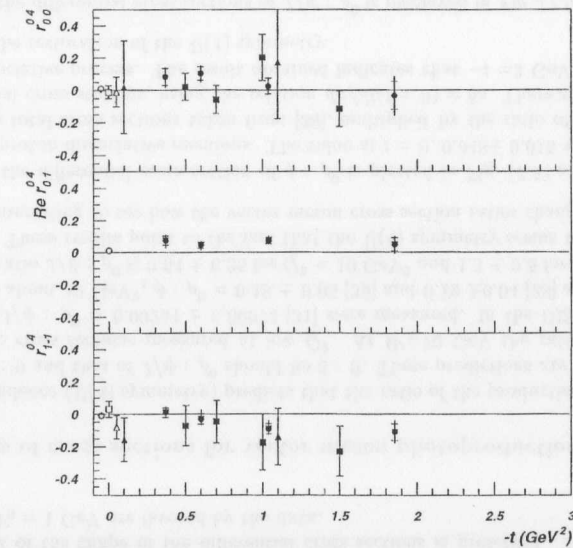


Figure 7.3: The spin density matrix elements as a function of $-t$ measured in this analysis (full symbols) and in the low $-t$ ZEUS measurements (empty symbols) for ρ^0 (circles), ϕ (squares) and J/ψ (triangles) mesons.

parameter	ρ^0	ϕ	J/ψ
r_{00}^{04}	0.06 ± 0.03	0.00 ± 0.05	0.08 ± 0.22
$\text{Re} r_{10}^{04}$	0.06 ± 0.02		
r_0	0.07 ± 0.02	0.14 ± 0.07	0.15 ± 0.10

Table 7.1: The parameters obtained from the fits to the present data.

7.2 Comparison with pQCD based models and Regge based models

In the following sections the results of this analysis are compared to the pQCD and Regge based model.

7.2.1 Comparison with pQCD based models

In Fig. (7.4) the measured proton-dissociative cross sections calculated for $M_N^2 < 0.01 \cdot W^2$ are compared with the pQCD predictions for light [12] and heavy [9] mesons at $-t > 1 \text{ GeV}^2$. The requirement of relatively small mass M_N was imposed to ensure coupling of the exchanged gluons to the same quark [10] in the proton, as was assumed in the calculations.

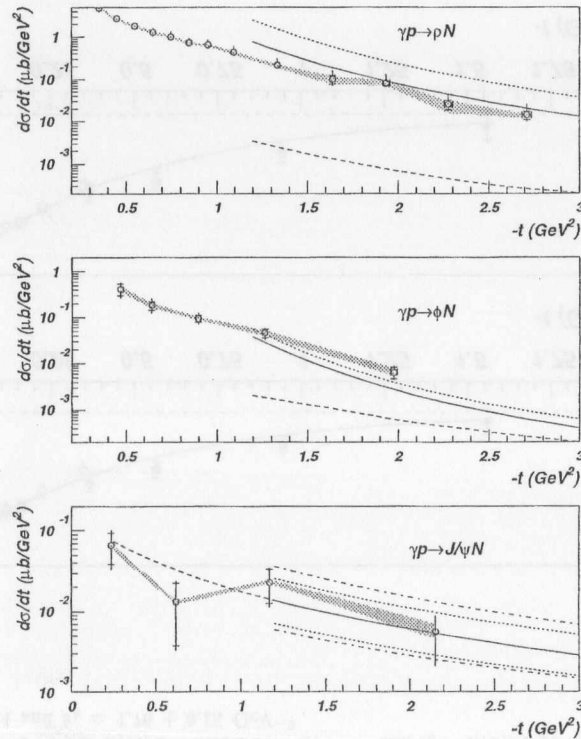


Figure 7.4: The comparison of the measured differential cross sections for the proton-dissociative production with the pQCD based models. For the description of curves see the text.

The calculations for the production of the ρ^0 and ϕ mesons were done at the lowest order in α_S . The non-perturbative effects were simulated by introducing effective masses of quarks and anti-quarks, m_q . In Fig. (7.4) the solid (dotted) lines represent results for $m_q = 300$ (200) MeV. The contribution of the purely perturbative production is still small for the considered t range and is represented by dashed lines. The comparison of the curves in Fig. (7.4) at much higher $-t$ range (not shown on the plot) indicates that the purely perturbative production (dashed lines) of the ρ^0 and ϕ mesons may dominate approximately only above $-t$ of 10 and 6 GeV^2 , respectively (intersection points of dashed and solid curves).

The nominal perturbative QCD prediction for the J/ψ production compares well with the data (solid line in Fig. (7.4)). The extrapolation of this prediction below $-t = 1 \text{ GeV}^2$ (dashed line) gives also a good description of the data. The uncertainties due to the choice of α_S ($\pm 10\%$ - dotted lines) and the $\log(W^2/W_0^2)$ scale ($0.2 < W_0^2 < 5 \text{ GeV}^2$ - dashed-dotted lines) are significant, however a good agreement of the shape of the differential cross sections is preserved. The nominal values of $\alpha_S = 0.2$ and $W_0 = 1 \text{ GeV}$ are favored by the data.

7.2.2 Ratios of cross sections for vector meson photoproduction

Flavour independence (U(4) symmetry) predicts that the ratio of the production cross sections of $\phi : \rho^0$ should be 2 : 9 and that of $J/\psi : \rho^0$ should be 8 : 9. These predictions are in large disagreement with the elastic cross sections measured at low Q^2 . At $W=70 \text{ GeV}$ the ratios $\phi : \rho^0 = 0.065 \pm 0.013$ [30] and $J/\psi : \rho^0 = 0.00294 \pm 0.00074$ [31] were measured. In the DIS kinematic region, as Q^2 increases to about 12 GeV^2 , $\phi : \rho^0 = 0.18 \pm 0.05$ [30] and 0.19 ± 0.04 [28] at $W \approx 100 \text{ GeV}$ were obtained. The ratio $J/\psi : \rho^0$ is 0.64 ± 0.35 for $Q^2 = 10 \text{ GeV}^2$ and 1.3 ± 0.5 for $Q^2 = 20 \text{ GeV}^2$ [29] at $W \approx 100 \text{ GeV}$. These results point to the fact that the U(4) symmetry seems to be restored at large Q^2 . It is thus interesting to see how the vector meson cross section ratios change with t .

The ratio of the differential cross section of $\phi : \rho^0$ is plotted in Fig. (7.5) as function of t for the elastic and the proton-dissociative reactions. The value at $t = 0$, 0.048 ± 0.015 was obtained by using the ratio of the total cross sections taken from [30], multiplied by the ratio of the respective slopes of the differential cross sections, using the relation $d\sigma/dt(t=0) = b\sigma$. There are no data at $t = 0$ for the proton-dissociative process. The result obtained indicates that $-t = 3 \text{ GeV}^2$ is not a sufficiently large scale for the restoration of the U(4) symmetry.

The ratio of the differential cross-sections of $J/\psi : \rho^0$ is displayed in Fig. (7.5) in a similar manner to that of the $\phi : \rho^0$ ratio. Here too the value at $t = 0$, 0.00138 ± 0.00044 was obtained by using the ratio of the total elastic cross section values [31] and rescaling them by the ratios of the respective slopes of the differential cross sections. The ratio of the differential cross sections is seen to be growing, it reaches a value which is still more than one order of magnitude smaller than the expected 8 : 9 even at $-t = 3 \text{ GeV}^2$.

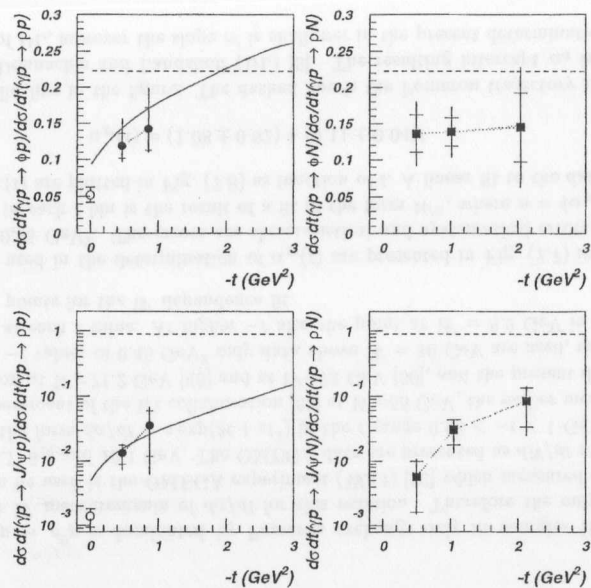


Figure 7.5: The ratios of the differential cross sections $d\sigma/dt$, ϕ to ρ^0 and J/ψ to ρ^0 for the elastic (full circles) and the proton-dissociative (squares) photoproduction. The empty circles represent the measurements for the elastic production at $t=0$. The dashed lines correspond to the $U(4)$ expectations.

7.2.3 Comparison with Regge pole based models

Test of the factorization hypothesis

The ratio of the elastic to the proton-dissociative reaction is expected (see Eq. (2.35)) to be independent of the type of the vector meson.

To test this hypothesis the ratios $\frac{d\sigma}{dt}(\gamma p \rightarrow Vp) / \frac{d\sigma}{dt}(\gamma p \rightarrow VN)$ for the three vector mesons $V = \rho^0, \phi, J/\psi$ were re-plotted in Fig. (7.6). As can be seen, the ratio is the same within errors for each of the three vector mesons, confirming the factorization hypothesis.

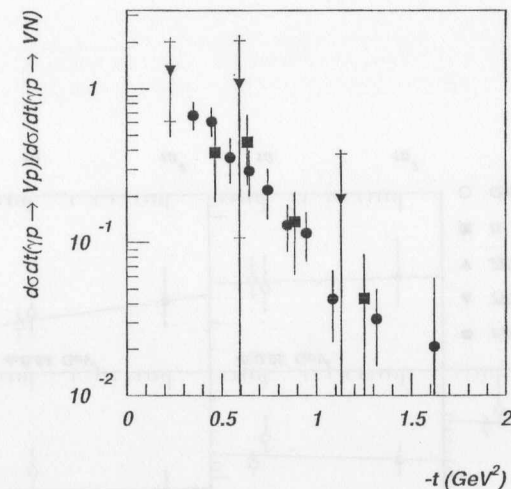


Figure 7.6: The ratio of elastic to proton-dissociative differential cross section as function of $-t$ for ρ^0 (circles), ϕ (squares) and J/ψ (triangles). The error bars correspond to the total error.

Determination of the Pomeron trajectory

In the Regge theory the elastic cross section $d\sigma/dt$ is given by (see Eq. (2.26))

$$d\sigma/dt = f(t) \cdot (W^2)^{2\alpha_P(t)-2} \quad (7.1)$$

where $f(t)$ is a function of t only and $\alpha_P(t)$ is the Pomeron trajectory.

By studying the W dependence of $d\sigma/dt$ at fixed t , $\alpha_P(t)$ can be determined directly. If in addition the trajectory is assumed to be linear

$$\alpha_P(t) = \alpha_P(0) + \alpha' t \quad (7.2)$$

The intercept and slope of the trajectory can be obtained by fitting Eq. (7.2) to the measured $\alpha_p(t)$ values.

The most precise determinations of the Pomeron trajectory using the above mentioned procedure are from pp elastic scattering experiments and yield an intercept of $\alpha_p(0) = 1.08$ and a slope of $\alpha' = 0.25 \text{ GeV}^{-2}$ [36, 37]. It is accepted that the Pomeron trajectory is universal and has a slope of 0.25 GeV^{-2} .

The steep energy behaviour of the elastic J/ψ photoproduction cross section at HERA cannot be described in the Regge picture by the Pomeron trajectory with a constant intercept of 1.08 and requires a larger intercept. In addition, a direct determination of the Pomeron trajectory in a way similar to that described above showed that the slope α' from elastic photoproduction of J/ψ is smaller than 0.25 GeV^{-2} [40]. These observations point to the fact that the Pomeron trajectory does not seem to be universal when a large scale is involved. It is thus of interest to see whether the universality notion can be kept in soft interactions.

In the present analysis the accurate means of measuring t for the tagged events permit a measurement of the trajectory over the region in momentum transfer where the energy dependence in the elastic cross section changes from rising to falling.

$\gamma p \rightarrow \rho^0 p$

Since the reaction $\gamma p \rightarrow \rho^0 p$ is dominated by Pomeron exchange only at energies $W \sim 10 \text{ GeV}$, one cannot use lower W measurements of $d\sigma/dt$ for this reaction. Therefore the only fixed target experiment which can be used is the OMEGA experiment (WA4) [52] which measured elastic photoproduction at $W = 6.7, 8.2$ and 10.1 GeV . The OMEGA data are presented as dN/dt at the three W values, and fitted to the form $d\sigma/dt = a \exp(bt + ct^2)$ in the t range $0.06 < -t < 1 \text{ GeV}^2$. From the HERA data the measurement of the H1 collaboration [53] at $W=55 \text{ GeV}$, the earlier measurements of the ZEUS collaboration at $W=71.2 \text{ GeV}$ [45] and at $W=73 \text{ GeV}$ [50], and the present data at $W=94 \text{ GeV}$ are used. Up to $-t$ values of 0.45 GeV^2 only data above $W = 10 \text{ GeV}$ are used, since there are three or more points at each t value. At higher $-t$ also the point at $W = 8.2 \text{ GeV}$ is used so as to have a minimum of 3 points for the W dependence fit.

The data of $d\sigma/dt$ used in the determination of $\alpha_p(t)$ are presented in Fig. (7.7) in 12 t bins in the range $0 \leq -t \leq 0.95 \text{ GeV}^2$. The errors are the statistical and systematical errors combined in quadrature. The line in each t bin is the result of a fit of the form W^n , where $n = 4\alpha_p(t) - 4$. The resulting values of $\alpha_p(t)$ are plotted in Fig. (7.8) as function of t . A linear fit to the data yields

$$\alpha_p(t) = (1.08 \pm 0.02) + (0.11 \pm 0.04)t \quad (7.3)$$

and is plotted as a solid line in the figure. The dashed line is the Pomeron trajectory $1.0808 + 0.25 t$, as determined by Donnachie and Landshoff (DL) [5]. The resulting intercept α_0 is in excellent agreement with that of DL, however the slope α' is shallower in the present determination.

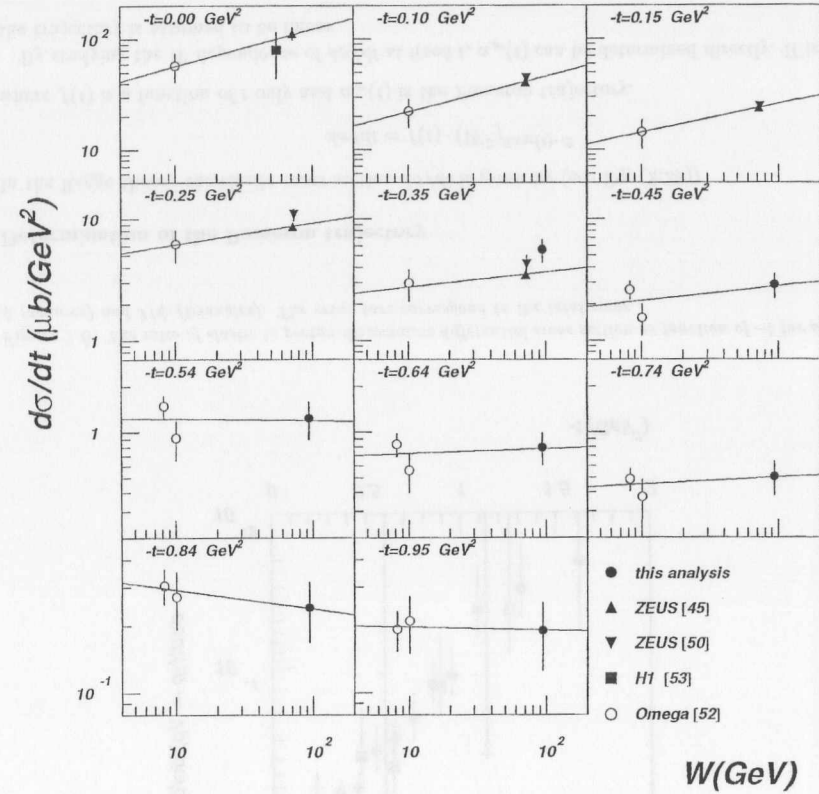


Figure 7.7: Fits to $d\sigma/dt \propto (W)^{4\alpha(t)-4}$ for exclusive ρ^0 production. Statistical and systematic uncertainties were added in quadrature.

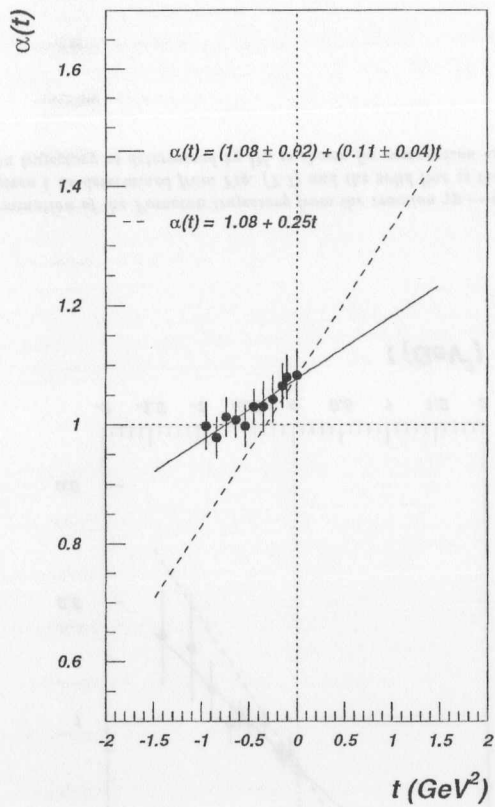


Figure 7.8: Determination of the Pomeron trajectory from the reaction $\gamma p \rightarrow \rho^0 p$. The dots are the values of the trajectory at a given t as determined from Fig. (7.7) and the solid line is the result of a linear fit to these values. The Pomeron trajectory as determined by DL is shown for comparison as a dashed line.

$\gamma p \rightarrow \phi p$

The elastic photoproduction of ϕ is a good reaction to study the properties of the Pomeron since this is the only trajectory that one can exchange, assuming the ϕ to be a pure $s\bar{s}$ state. This allows the use of low W data in the procedure described above.

The $d\sigma/dt$ data used for the trajectory determination include the following: $W=2.64-3.60$ GeV [56], $W=2.8$ [58], $W=2.81-4.28$ GeV [59], $W=3.59-4.21$ GeV [60], $W=4.73-5.85$ GeV [61], $W=12.89$ GeV [62], $W=70$ GeV [46] and the present measurement at $W=94$ GeV. These data points are displayed in Fig. (7.9) for 11 t values in the range $0 \leq -t \leq 1.4$ GeV². The lines are the results of fits of the function W^n to the data. The resulting values of the trajectory $\alpha_p(t)$ are shown in Fig. (7.10) as a function of t . Assuming a linear trajectory and fitting $\alpha_p(t)$ to a straight line one gets

$$\alpha_p(t) = (1.08 \pm 0.01) + (0.15 \pm 0.04)t. \quad (7.4)$$

This trajectory is shown as a solid line in the figure and compared with the DL trajectory, which is plotted as a dashed line. As in the ρ^0 case, the intercepts agree very well while the slope of the present measurement is smaller than that of the DL trajectory.

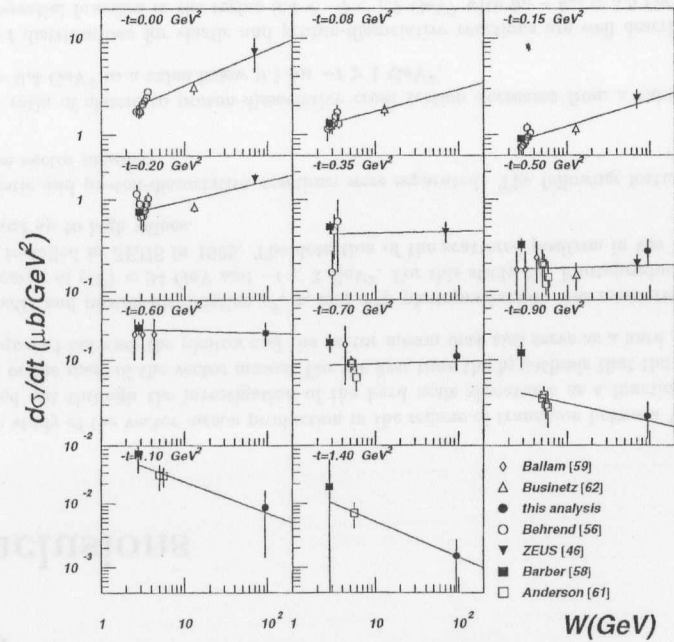


Figure 7.9: Fits to $d\sigma/dt \propto (W)^{4\alpha(t)-4}$ for exclusive ϕ production. Statistical and systematic uncertainties were added in quadrature.

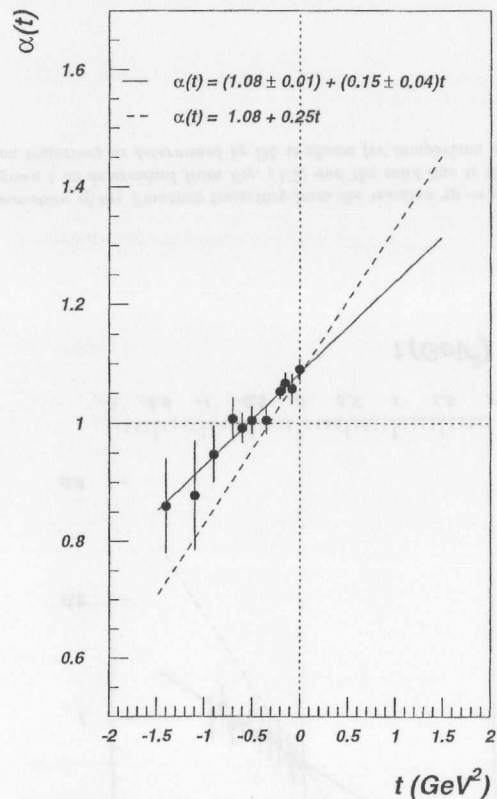


Figure 7.10: Determination of the Pomeron trajectory from the reaction $\gamma p \rightarrow \phi p$. The dots are the values of the trajectory at a given t as determined from Fig. (7.7) and the solid line is the result of a linear fit to these values. The Pomeron trajectory as determined by DL is shown for comparison as a dashed line.

Chapter 8

Conclusions

So far the study of the vector meson production in the regime of transition between VMD and pQCD was carried out through the investigation of the hard scale signatures as a function of the photon virtuality or the mass of the vector meson. For the first time the hypothesis that the four-momentum transfer squared between the photon and the vector meson may also serve as a hard scale was tested.

The elastic and proton-dissociative ρ^0 , ϕ , and J/ψ photoproduction was measured at a γp center of mass energy of $\langle W \rangle = 94$ GeV and $-t < 3$ GeV². For this study the Photoproduction Tagger was built and installed in ZEUS in 1995. The detection of the scattered positron in the PT allows $-t$ to be measured up to high values.

The elastic and proton-dissociative reactions were separated. The following features are common to all three vector mesons:

- The ratio of elastic to proton-dissociative cross section decreases from a value of about 1 at $-t = 0.4$ GeV² to a value below 0.1 for $-t > 1$ GeV².
- The t distributions for elastic and proton-dissociative reactions are well described by a single exponential function in the region $0.4 < -t < 1.2$ GeV² with $b_{el} - b_{pd} \approx 3.5$ GeV⁻².
- The decay angular distributions are generally consistent with SCHC hypothesis except for the highest $-t$ range accessible in this analysis where r_{1-1}^{04} was found to be different from zero. However present accuracy does not allow to conclude about SCHC violation at $-t$ range covered in this analysis.

A comparison of the properties of elastic and proton-dissociative photoproduction of the three vector mesons shows that the factorization hypothesis holds.

In the case of ρ^0 ($\rho^0 \rightarrow \pi^+\pi^-$) production, the $\pi^+\pi^-$ invariant mass spectrum is skewed. The amount of skewing decreases with increasing $-t$ and is similar for elastic and proton-dissociative $\pi^+\pi^-$ production.

The proton-dissociative cross sections calculated for $M_N^2 < 0.01 \cdot W^2$ were compared with the pQCD predictions for ρ^0 , ϕ and J/ψ mesons at $-t > 1$ GeV². For ρ^0 and ϕ the contribution of the purely perturbative production is still small for the considered t range and may dominate approximately only above $-t$ of 10 and 6 GeV², respectively. The nominal perturbative QCD prediction for the J/ψ production compares well with the data.

The ratios of ϕ to ρ^0 and J/ψ to ρ^0 photoproduction cross sections were studied as a function of t for both elastic and proton-dissociative processes. The ratios increase with $-t$ but even at $-t = 3 \text{ GeV}^2$ are still much lower than that expected from $U(4)$ symmetry.

The Pomeron trajectory was determined from elastic production of ϕ and ρ^0 mesons by studying the W dependence of $d\sigma/dt$ at fixed t values of the present measurements together with lower W data from other experiments. The fit of the linear trajectory to the data for ρ^0 and ϕ mesons in the range $0.0 < -t < 0.9 \text{ GeV}^2$ and $0.0 < -t < 1.4 \text{ GeV}^2$, respectively yields $\alpha_p(t) = (1.08 \pm 0.02) + (0.11 \pm 0.04)t$ for elastic ρ^0 photoproduction and $\alpha_p(t) = (1.08 \pm 0.01) + (0.15 \pm 0.04)t$ for elastic ϕ photoproduction. The lower values of α' determined in this analysis imply that the Pomeron trajectory is not universal even in soft processes.

The measurements show that ρ^0 and ϕ production in the t range covered by this analysis generally exhibits the features of a soft diffractive process. On the other hand, in comparison with the low $-t$ data, there are possible indications of the transitional character of this data, such as non-zero values of r_{1-1}^{04} and increase of the ratios of cross sections ϕ to ρ^0 and J/ψ to ρ^0 towards the expectations from $U(4)$ symmetry.

It was shown that several experimental techniques exist to analyze vector meson production at large $-t$. The main limitations of this study were low numbers of vector meson candidates at sufficiently large $-t$ and FCAL energy limitation in the trigger. Since 1996 the data are collected with an improved trigger which allows to constrain $d\sigma/dM_N^2$ behavior at large $-t$. The much higher integrated luminosity of this data allows also the extension of the vector meson measurements upto $-t = 13 \text{ GeV}^2$. Analyzing this new data we should finally be able to answer whether the four-momentum transfer squared t between the photon and the vector meson may also serve as a hard scale.

Acknowledgments

I am very grateful to my supervisor Professor Danuta Kiselewska for her continuous support and encouragement during the writing of this thesis. Furthermore, I would like to thank her for all the trust she put in my work.

I wish to thank the Directorate of the DESY laboratory for supporting my stay in Hamburg.

I would like to thank Dr Krzysztof Piotrkowski. I have learned a lot from him and would like to give him a special thank you.

I would like to thank Professor Andrzej Eskreys for his support during my work in the LUMI group.

I thank a lot all of my colleagues in the LUMI group and in particular Agnieszka Kowal for her hard work on correcting my English.

Finally, I would like to thank my family for their help, patience and care.

Appendix A

In this appendix the Eq. (4.2, 4.3 and 4.4) are derived.

In the two-body scattering process $1+2 \rightarrow 3+4$ ($\gamma^* + p \rightarrow V + p(N)$) assuming that P_i are the respective four-vectors ($P_i = (E_i, \vec{p}_i)$; $|\vec{p}_i| = p_i$)

$$\begin{aligned} t &= (P_1 - P_3)^2 \\ &= (E_1 - E_3)^2 - (\vec{p}_1 - \vec{p}_3)^2 \\ &= (E_1 - E_3)^2 - p_1^2 - p_3^2 + 2p_1p_3 \cos \theta \end{aligned} \quad (1)$$

where θ is the angle between \vec{p}_1 and \vec{p}_3 momenta.

Since $\cos \theta = 1 - 2 \sin^2(\theta/2)$

$$\begin{aligned} t &= (E_1 - E_3)^2 - p_1^2 - p_3^2 + 2p_1p_3 - 4p_1p_3 \sin^2(\theta/2) \\ &= (E_1 - E_3)^2 - (p_1 - p_3)^2 - 4p_1p_3 \sin^2(\theta/2) \\ &= t_0 - 4p_1p_3 \sin^2(\theta/2) \end{aligned} \quad (2)$$

where t_0 is the maximum $t(\theta = 0)$ value

$$t_0 = (E_1 - E_3)^2 - (p_1 - p_3)^2. \quad (3)$$

In the 1-2 (photon-proton) center-of-mass system $\vec{p}_1 = -\vec{p}_2$ and $\vec{p}_3 = -\vec{p}_4$

$$s = (P_1 + P_2)^2 = (P_3 + P_4)^2 \quad (4)$$

$$s = (E_1 + E_2)^2 = (E_3 + E_4)^2 \quad (5)$$

$$\sqrt{s} = E_1 + E_2 = E_3 + E_4 \quad (6)$$

On the other hand (since $P_i^2 = m_i^2 = E_i^2 - p_i^2$ and $\vec{p}_1\vec{p}_2 = -p_1^2 = -p_2^2$)

$$\begin{aligned} s &= (P_1 + P_2)^2 \\ &= m_1^2 + m_2^2 + 2P_1P_2 \\ &= m_1^2 + m_2^2 + 2(E_1E_2 - \vec{p}_1\vec{p}_2) \\ &= m_1^2 + m_2^2 + 2(E_1E_2 + p_1^2) \\ &= m_1^2 + m_2^2 + 2(E_1E_2 + E_1^2 - m_1^2) \\ &= -m_1^2 + m_2^2 + 2E_1(E_2 + E_1) \end{aligned} \quad (7)$$

From Eq. (6) and Eq. (7)

$$E_1 = \frac{s + m_1^2 - m_2^2}{2\sqrt{s}}. \quad (8)$$

By the same way it is easy to proof that:

$$E_2 = \frac{s + m_2^2 - m_1^2}{2\sqrt{s}}, \quad (9)$$

$$E_3 = \frac{s + m_3^2 - m_4^2}{2\sqrt{s}}, \quad (10)$$

$$E_4 = \frac{s + m_4^2 - m_3^2}{2\sqrt{s}}. \quad (11)$$

Inserting Eq. (8) and Eq. (10) to Eq. (3) leads to

$$\begin{aligned} t_0 &= \frac{[(s + m_1^2 - m_2^2) - (s + m_3^2 - m_4^2)]^2}{4s} - (p_1 - p_3)^2, \\ t_0 &= \frac{(m_1^2 - m_2^2 - m_3^2 + m_4^2)^2}{4s} - (p_1 - p_3)^2. \end{aligned} \quad (12)$$

In our case: $m_1^2 = -Q^2$; $m_2^2 = M_p^2$; $m_3^2 = M_V^2$; $m_4^2 = M_N^2$; $p_1 = p_\gamma$; $p_3 = p_V$; $s = W^2$ so Eq. (3) and Eq. (2) can be expressed as

$$t_0 = \frac{(M_N^2 - M_p^2 - Q^2 - M_V^2)^2}{4W^2} - (p_\gamma - p_V)^2, \quad (13)$$

$$t = \frac{(M_N^2 - M_p^2 - Q^2 - M_V^2)^2}{4W^2} - (p_\gamma - p_V)^2 - 4p_\gamma p_V \sin^2(\theta/2). \quad (14)$$

which is the Eq. (4.3).

Now I am going to approximate the formula for t_0 by putting $p_1 = \sqrt{E_1^2 - m_1^2}$ and $p_3 = \sqrt{E_3^2 - m_3^2}$ to Eq. (3)

$$\begin{aligned} t_0 &= (E_1 - E_3)^2 - \left(\sqrt{E_1^2 - m_1^2} - \sqrt{E_3^2 - m_3^2} \right)^2 \\ &= (E_1 - E_3)^2 - \left(E_1 \sqrt{1 - m_1^2/E_1^2} - E_3 \sqrt{1 - m_3^2/E_3^2} \right)^2 \end{aligned} \quad (15)$$

Since $\sqrt{1-x} \approx 1 - x/2$ for $x \ll 1$

$$\begin{aligned} t_0 &\approx (E_1 - E_3)^2 - \left[E_1(1 - m_1^2/2E_1^2) - E_3(1 - m_3^2/2E_3^2) \right]^2 \\ &\approx (E_1 - E_3)^2 - \left(E_1 - m_1^2/2E_1 - E_3 + m_3^2/2E_3 \right)^2 \\ &\approx (E_1 - E_3)^2 - \left[(E_1 - E_3) - (m_1^2/2E_1 - m_3^2/2E_3) \right]^2 \\ &\approx (E_1 - E_3)^2 - \left[(E_1 - E_3)^2 - 2(E_1 - E_3)(m_1^2/2E_1 - m_3^2/2E_3) + (m_1^2/2E_1 - m_3^2/2E_3)^2 \right] \\ &\approx 2(E_1 - E_3)(m_1^2/2E_1 - m_3^2/2E_3) - (m_1^2/2E_1 - m_3^2/2E_3)^2 \\ &\approx (m_1^2/2E_1 - m_3^2/2E_3)[2(E_1 - E_3) - m_1^2/2E_1 + m_3^2/2E_3] \end{aligned} \quad (16)$$

Above approximation is valid for $|m_1^2| \ll E_1^2$ and $|m_3^2| \ll E_3^2$. Inserting Eq. (8) and Eq. (10) to Eq. (16) leads to

$$t_0 \approx \left(\frac{m_1^2}{s + m_1^2 - m_2^2} - \frac{m_3^2}{s + m_3^2 - m_4^2} \right) (m_1^2 - m_2^2 - m_3^2 + m_4^2) - \frac{sm_1^2}{s + m_1^2 - m_2^2} + \frac{sm_3^2}{s + m_3^2 - m_4^2} \quad (17)$$

For $m_1^2 - m_2^2 \ll s$ and $m_3^2 - m_4^2 \ll s$ above formula can be approximated further

$$\begin{aligned} t_0 &\approx \frac{m_1^2 - m_3^2}{s} (m_1^2 - m_2^2 - m_3^2 + m_4^2 - m_1^2 + m_3^2) \\ &\approx \frac{(m_1^2 - m_3^2)(m_4^2 - m_2^2)}{s} \end{aligned} \quad (18)$$

In our case Eq. (18) can be written as

$$t_0 \approx -\frac{(Q^2 + M_V^2)(M_N^2 - M_p^2)}{W^2} \quad (19)$$

or for $Q^2 \ll M_V^2$ as

$$t_0 \approx -M_V^2(M_N^2 - M_p^2)/W^2 \quad (20)$$

which is the right side of the Eq. (4.4).

Now I am going to approximate the rest of the Eq. (2) using

$$\sin \theta = p_{3,T}/p_3 \quad (21)$$

where $p_{3,T}$ is the transverse momentum of the particle 3(vector meson). In the limit $p_{3,T} \ll p_3$, $\sin \theta \approx \theta$ and $\sin(\theta/2) \approx \theta/2$. In the above limit one can write

$$\sin(\theta/2) \approx p_{3,T}/(2p_3). \quad (22)$$

Inserting Eq. (22) to Eq. (2) leads to

$$\begin{aligned} t &\approx t_0 - 4p_1 p_3 (p_{3,T}/2p_3)^2 \\ &\approx t_0 - \frac{p_1}{p_3} p_{3,T}^2 \\ &\approx t_0 - \frac{\sqrt{E_1^2 - m_1^2}}{\sqrt{E_3^2 - m_3^2}} p_{3,T}^2. \end{aligned} \quad (23)$$

In the limits $|m_1^2| \ll E_1^2$ and $|m_3^2| \ll E_3^2$ above equation can be written as

$$t \approx t_0 - \frac{E_1}{E_3} p_{3,T}^2. \quad (24)$$

Inserting Eq. (8) and Eq. (10) to the last equation leads to

$$t \approx t_0 - \frac{s + m_1^2 - m_2^2}{s + m_1^2 - m_4^2} p_{3,T}^2. \quad (25)$$

In the limits $|m_1^2 - m_2^2| \ll s$ and $|m_3^2 - m_4^2| \ll s$ the above equation can be approximated further

$$t \approx t_0 - p_{3,T}^2. \quad (26)$$

Inserting last equation and Eq. (20) to Eq. (2) leads to

$$t \approx t_0 - p_{3,T}^2 \approx -M_V^2(M_N^2 - M_p^2)/W^2 - p_{3,T}^2. \quad (27)$$

which is the Eq. (4.4).

Bibliography

- [1] L. Frankfurt, M. Strikman, *Phys. Rev. Lett.* **63** (1989) 1914.
- [2] A.H. Mueller, W-K. Tang, *Phys. Lett.* **B284** (1992) 123.
- [3] G. Levman, *ZEUS-Note* 95-088.
- [4] P.D.B. Collins, *An introduction to Regge Theory and High Energy Physics* Cambridge University Press, England.
- [5] A. Donnachie, P.V. Landshoff, *Nucl. Phys.* **B231** (1984) 189.
A. Donnachie, P.V. Landshoff, *Phys. Lett.* **B191** (1987) 309.
A. Donnachie, P.V. Landshoff, *Phys. Lett.* **B296** (1992) 227.
- [6] K. Schilling, G. Wolf, *Nucl. Phys.* **B61** (1973) 381.
- [7] S.J. Brodsky et al., *Phys. Rev.* **D50** (1994) 3134.
- [8] M.G. Ryskin, *Zeit. Phys.* **C57** (1993) 89.
M.G. Ryskin et al., *Zeit. Phys.* **C76** (1997) 231.
- [9] J. Bartels, J.R. Forshaw, H. Lotter and M. Wüsthoff, *Phys. Lett.* **B375** (1996) 301.
- [10] D.Yu Ivanov, *Phys. Rev.* **D53** (1996) 3564.
- [11] V.L. Chernyak and A.R. Zhitnitsky, *Phys. Rep.* **112** (1984) 173.
- [12] I.F. Ginzburg, D.Yu Ivanov, *Phys. Rev.* **D54** (1996) 5523.
- [13] H. Abramowicz, L. Frankfurt, M. Strikman, *Surveys in High Energy Phys.* **11** (1997) 51.
- [14] ZEUS Collaboration, *The ZEUS detector*, Status Report 1994.
- [15] G.F. Hartner et al., *ZEUS-Note* 96-013.
- [16] Song Ming Wang, *ZEUS-Note* 96-121.
- [17] TRKCLU, ZEUS user library.
- [18] L. Adamczyk, K. Piotrkowski *ZEUS-Note* 99-029
- [19] R. Brun et al., GEANT 3, *CERN/DD/EE/84-1* (1987).
- [20] M. Arneodo, L. Lamberti, M. Ryskin *Computer Phys. Comm.* **100** (1997) 195.
- [21] M. Kasprzak, *ZEUS-Note* 95-069.
- [22] A. Mastroberardino, *ZEUS-Note* 98-057.

[23] MOZART, ZEUS internal package.

[24] T. Sjostrand, *Computer Phys. Comm.* **39** (1986) .

[25] UA8 Collab., A. Brandt et al., *Nucl. Phys.* **B514** (1998) 3.

[26] Albrow et al., *Nucl. Phys.* **B108** (1975) 1.

[27] F. Abe et al., *Phys. Rev.* **D50** (1994) 5535.

[28] H1 Collab., C. Adloff et al., *Zeit. Phys.* **C75** (1997) 607.

[29] H1 Collab., S. Aid et al., *Nucl. Phys.* **B468** (1996) 3.

[30] ZEUS Collab., M. Derrick et al., *Phys. Lett.* **B380** (1996) 220.

[31] ZEUS Collab., M. Derrick et al., *Phys. Lett.* **B 350** (1995) 120;

[32] H1 Collab., S. Aid et al., *Nucl. Phys.* **B 468** (1996) 3.

[33] V.N. Gribov, L.Ya Pomeranchuk, *Phys. Rev. Lett.* **8** (1962) 343.

[34] CHLM Collab., M.G. Albrow et al., *Nucl. Phys.* **B108** (1976) 1.

[35] J.J.J. Kokkedee, *The quark model*, W.A. Benjamin, Inc., 1969.

[36] G.A. Jaroszkiewicz, P.V. Landshoff, *Phys. Rev.* **D10** (1974) 170.

[37] P.D.B. Collins, F.D. Gault, A. Martin, *Nucl. Phys.* **B80** (1974) 135.

[38] G. Giacomelli, *Phys. Rep.* **23C** (1976) 123.

[39] J.P. Burq et al., *Phys. Lett.* **B109** (1982) 124.
J.P. Burq et al., *Nucl. Phys.* **B217** (1983) 285.

[40] A. Levy *Phys. Lett.* **B424** (1998) 191.

[41] R.L. Coll et al., *Phys. Rev. Lett.* **48** (1982) 1451.

[42] G. Zech, *DESY* 95-113.

[43] MINUIT, CERN program library.

[44] Dirk Westphal *DESY F35D-97-11*.

[45] ZEUS Collab., J. Breitweg et al., *Eur. Phys. J.* **C2** (1998) 247.

[46] ZEUS Collab., M. Derrick et al., *Zeit. Phys.* **C73** (1996) 73.

[47] P. Söding, *Phys. Lett.* **19** (1966) 702.

[48] M. Ross, L. Stodolsky, *Phys. Rev.* **149** (1966) 1172.

[49] For a review, see e.g. T.H. Bauer et al., *Rev. Mod. Phys.* **50** (1978) 261.

[50] ZEUS Collab., M. Derrick et al., *Z. Phys.* **C 73** (1997) 253.

[51] ZEUS Collab., M. Derrick et al., *Z. Phys.* **C 69** (1995) 39.

[52] D. Aston et al., *Nucl. Phys.* **B209** (1982) 56.

[53] H1 Collab., S. Aid et al., *Nucl. Phys.* **B463** (1996) 3.

[54] ZEUS Collab., M. Derrick et al., *Phys. Lett.* **B 377** (1996) 259.

[55] ZEUS Collab., M. Derrick et al., *Phys. Lett.* **B 356** (1995) 601.
H1 Collab., S. Aid et al., *Nucl. Phys.* **B 468** (1996) 3.

[56] H.J. Behrend et al., *Nucl. Phys.* **B144** (1978) 22.

[57] E. Gotsman, A. Levy, *Phys. Rev.* **D13** (1976) 3036.

[58] D.P. Barber et al., *Zeit. Phys.* **C12** (1982) 1.

[59] J. Ballam et al., *Phys. Rev.* **D7** (1973) 3150.

[60] G. McClellan et al., *Phys. Rev. Lett.* **26** (1971) 1593.

[61] R. Anderson et al., *Phys. Rev.* **D1** (1970) 27.

[62] J. Busenitz et al., *Phys. Rev.* **D40** (1989) 1.

[63] J-R. Cudell, K. Kang, S.K. Kim, *Phys. Lett.* **B395** (1997) 311.

[64] K. Desler, *ZEUS-Note* 95-061.